

**VUV LASER-INDUCED PLASMA SPECTROSCOPY FOR
LOW LEVEL SULPHUR DETECTION IN STEEL**

A thesis submitted for the degree of

DOCTOR of PHILOSOPHY

Presented to:

*The School of Physical Sciences, Faculty of Science and Health, Dublin City
University*

Author:

EOIN P. O' LEARY

B.SC. A.M.INST.P.

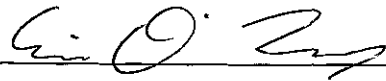
Research Supervisor:

PROF. EUGENE T. KENNEDY

B.SC. PH. D C. PHYS. F. INST.P. M.R.I.A.

Declaration

I hereby certify that this material, which I now submit for assessment on the programme of study leading to the award of Doctor of Philosophy, Ph D. is entirely my own work and has not been taken from the work of others save and to the extent that such work has been cited and acknowledged within the text of my work.

Signed: 

ID No.: 97054615

Date 17/8/07

To my parents and to Ann.

Acknowledgments

First and foremost, sincere thanks must go to Prof. Eugene Kennedy, my supervisor for giving me the opportunity to work in the CLPR and for guiding my work therein. Throughout my time in DCU as a postgrad student his absolute willingness to talk on any subject was a great help to me both solve problems I encountered in and out of the lab and avoid some possible difficulties entirely. His seemingly endless patience and attention to detail are of great value when dealing with enthusiastic but occasionally confused students!

I'd also like to thank the other members of the CLPR. In particular, I'd like to extend my warm thanks to Prof. John Costello and Dr. Paul Van Kampen. JC for, as his deific name suggests, seemingly being able to perform multiple tasks simultaneously such as organise experiments, conduct highly complex technical conversations and still manage to tell me how rubbish my car is. Paul for always being around to help, advise and generally have a chat with in the corridors - always appreciated.

Both past and present research students have also had a great influence on my time in DCU. From the past: John Hirsch, Mark Stapleton, Mohamed Khater, Alan McKiernan and James Fryar; the postgrads with whom I started: Kevin Kavanagh, Deirdre McCabe, Oisín McDonald & Richard O' Haire and finally to the new batch of postgrads: John Dardis, Caroline Banahan, Pádraig Haugh and Vincent Richardson - thanks for all the interesting visits to labs, problems I was lucky enough to try to help answer and many, many highly entertaining Ballygowan-fuelled evenings in various local establishments!

To all the staff in DCU, both academic and technical - very many thanks for all the good times and good conversations over the years. Special thanks must be extended to Pat Wogan for effortless assistance to my many electronics queries and Des Lavelle for lots of work and endless, selfless political advice since the day I started working here. I still vote the wrong way Des, unfortunately that's not likely to change any time soon!

Finally, thanks to my friends and parents for all your support - it was and is greatly appreciated. Thanks also to Ann, for showing everyone that cared to see what hanging in there is all about

ABSTRACT

When a short, high energy pulse of laser light is focused onto a solid target a high density, high temperature plasma is formed. This plasma emits radiation across a wide spectral range, from the x-ray to the infra-red. In this thesis, a variant of the well-established spectroscopic technique known as Laser-Induced Plasma Spectroscopy (LIPS) is used in order to more sensitively quantify sulphur content in steels. LIPS is a well-established method for both quantitative and qualitative analysis of solids, liquids and gases. A particular problem exists with the elemental characterisation of the light elements ($Z < 20$) including sulphur in that the strongest resonant emission lines from these elements lie in the VUV part of the spectrum.

In this thesis, the VUV region of the spectrum has been exploited using a spatially-resolved approach which has proved to be superior to the more conventional time-resolved ultraviolet and visible LIPS experiments. Spectral surveys of the VUV region have been conducted in order to isolate interference-free sulphur emission lines. A number of optimisation studies have been made in order to improve the signal to standard deviation ratio in the characteristic background continuum emission. These included modification of the laser pulse energy, power density, lens focusing type (cylindrical and spherical) and ambient gas type & pressure.

As a result of these experiments, optimum conditions in which to construct calibration curves were found. Steel targets of certified sulphur concentration in the range 27 - 3800 ppm were used in the construction of these calibration functions. The sensitivity of the LIPS technique has been improved on substantially with an ultimate detection limit of 1.7 ± 0.1 ppm achieved using the emission features of the S V emission line at 78.65 nm.

TABLE OF CONTENTS

Declaration	ii
Dedication	iii
Acknowledgments	iv
Abstract	v
Table of Contents	vi
Chapter 1: Introduction	1
1.1 Thesis Organisation	2
1.2 The Development of LIPS as a Spectroscopic Technique	3
1.2.1 Early Studies	4
1.2.2 Modern Studies	5
1.2.3 LIPS for the Analysis of Sulphur in Steels	6
1.3 Aims and Objectives of the Present Work	10
1.4 Summary	11
References	13
Chapter 2: Theory of Laser Plasmas	16
2.1 Introduction	17
2.2 General Characteristics of Plasmas	17
2.3 Laser Plasma Formation	19
2.4 Atomic Processes in Laser Produced Plasmas	22
2.4.1 Free-Free Processes	22
2.4.2 Free-Bound Processes	23
2.4.3 Bound-Bound Processes	24
2.5 Quantitative Spectroscopy using Laser Plasmas	25
2.6 Analytical Figures of Merit	29
2.7 Summary	31
References	33
Chapter 3: Equipment and Laboratory Systems	35
3.1 Overview	36
3.2 Laser System. Continuum Surelite III-10	37
3.3 Target Chamber & Targets	41
3.3.1 Pre-Slit	44

3.3.2 Glass Capillary Arrays	45
3.4 1 m ARC VM-521 VUV Spectrometer/Concave Grating	46
3.4.1 General Theory of the Concave Diffraction Grating	48
3.4.2 Dispersion	51
3.4.3 Off-Rowland Mount & Spectral Characteristics	52
3.4.4 Resolution	53
3.5 Andor Technology CCD Camera	56
3.5.1 Quantum Efficiency & Noise	58
3.6 Vacuum Generation Systems	59
3.7 System Timing & Synchronisation	60
3.8 Summary	62
References	63
Chapter 4: Sulphur Detection in Steel: Vacuum Conditions	64
4.1 Introduction	65
4.1.1 VUV Transmission Coefficients	65
4.2 Time-Integrated Space-Resolved LIPS	66
4.3 Line Identification	70
4.3.1 LIPS Line Selection	71
4.4 Spherical vs Cylindrical Lenses	75
4.5 Laser Pulse Energy Variation	79
4.6 Focus Variation	83
4.7 Sulphur Calibration Curves	86
4.8 Summary	90
References	91
Chapter 5: LIPS for Detection of Sulphur in Steel: Ambient Atmospheres	93
5.1 Introduction	94
5.2 Theory	95
5.3 Experiment and Initial Spectra	99
5.4 Behaviour in Ambient Gases	105
5.5 Laser Pulse Optimisation	113
5.5.1 Energy Optimisation	114
5.5.2 Laser Pulse Defocusing	116
5.5.3 Variation in the Number of Accumulated Shots	118
5.6 Calibration Curves	120
5.6.1 Internally Referenced Sulphur Calibration	121

5 6.2 Standard Calibration Curve	122
5.7 Observations & Conclusions	124
5 7.1 Observations	124
5 7.2 Conclusion	127
References	129
Chapter 6: General Conclusions & Future Work	132
6.1 Summary & Conclusions of the Present Work	133
6.1.1 Summary	133
6.1.2 Conclusions	134
6.2 Future Work	136
6 2.1 Automation	137
6.2.2 Dual Pulse Technique	137
6.2.3 Plasma Diagnostics	138
6.2.4 Industrial Collaboration	139
References	140
Appendix A: Equilibrium in Plasmas	141
Appendix B: Targets	144
Appendix C: Spectral Line Profiles	145
List of Figures	148

CHAPTER I: INTRODUCTION

The introduction to this thesis is designed to contextualise the work in relation to progress in research in Laser-Induced Plasma Spectroscopy as it is being used in laboratory studies and on an industrial level. It is divided into an outline of the thesis structure followed by a general review on LIPS/LIBS in the wider scientific community with an emphasis on light elements & steels.

1.1 THESIS ORGANISATION

This thesis is divided into 6 main chapters with a number of appendices containing additional relevant information on some of the topics mentioned in the main body of the text.

Chapter 1 is a brief summary of the current state of research in Laser-Induced Plasma Spectroscopy (LIPS) with a general overview presented. A particular emphasis is given to research into studies performed on light elements and with steel as the main material.

Chapter 2 is an introduction to some of the theoretical aspects of laser ablation. This chapter provides a fundamental overview of laser light absorption by the target material which generates the plasma and how the resulting plasma behaves as it expands and cools. The basis for using laser plasmas as light sources for quantitative analytical spectroscopy is explained at the end of this chapter.

Chapter 3 is a description of the equipment used in the following experiments including details of the laser system employed, the spectrometer's operational characteristics and the method by which radiation from the laser plasma was captured. This chapter also details how these systems were combined in the Time-Integrated Space-Resolved (TISR) format.

Chapter 4 is a summary of the initial experiments conducted using laser plasmas as an analytical tool for LIPS in the Vacuum Ultraviolet (VUV). These experiments were conducted in a vacuum environment i.e. laser plasmas formed in these experiments freely expanded into a target chamber under vacuum. Quantitative results are presented as the result of these studies.

Chapter 5 describes LIPS experiments conducted in several different types of atmosphere - argon, nitrogen and air. Some experiments performed under vacuum are repeated to investigate the difference in the radiation emission under these environments. The results of these experiments conducted in buffer gases are presented along with contemporary theory on significant aberrations from experiments performed in vacuum.

Chapter 6 is a summary of experimental work and the general conclusions formed as a result of this series of experiments. Some future avenues of research are outlined in the context of current research direction and capabilities in the laser labs at DCU

Appendix A is a short description of an energy state known as *Local Thermal Equilibrium* and its importance in laser plasma physics.

Appendix B is a list of targets used in the experiments performed in chapters 4 and 5 and details their sulphur concentrations as provided by the retailer

Appendix C is a note on different types of spectral profiles and the importance of correct line profile use in analytical spectroscopy. This appendix contains information on different types of curves used to fit spectral lines.

1.2 THE DEVELOPMENT OF LIPS AS A SPECTROSCOPIC TECHNIQUE

1.2.1 EARLY STUDIES

Laser-Induced Plasma Spectroscopy (LIPS, also commonly referred to as LIBS - Laser-Induced *Breakdown* Spectroscopy) has been an established spectroscopic technique for elemental analysis since its conceptual birth by Brech & Cross (1963), made possible by the invention of the ruby laser by Maiman (1960) while working for Hughes Aircraft. For the first time, light at optical wavelengths could be focused onto a target in a short time to create the conditions necessary for plasma ignition. A number of reports on the properties and possible applications for high power lasers appeared in the literature over the next few years. Runge, Minck & Bryan (1963) observed that the emission from elemental species contained in a stainless steel sample was proportional to the concentration of these elements as they were changed via the introduction of new standardised targets. This is the earliest actual attempt at quantitative analysis using radiation from a laser plasma source, and paved the way for the wide number of applications today.

The potential for using laser plasma spectrochemical analysis as an online technique was investigated early on, as it offers the possibility of direct monitoring of molten materials as they are being created. This speeds up the industrial process

since samples of the material do not have to undergo removal, cooling and preparation in order to be analysed Runge, Bonfiglio & Bryan (1966) again showed the potential of the laser technique by testing another set of stainless steel samples, this time in a molten state. The authors note in this paper that some aspects of this technique can affect the analysis - notably that chromium detection can be affected by a layer of oxide on the surface of the melt, and also that the strong continuum emission from the laser plasma is far higher and more of a problem than the radiation emission from the hot molten steel.

The more fundamental properties of the laser plasma itself were also being considered in parallel with the more practical aspects of its use. Burgess, Fawcett & Peacock (1967) reported on the XUV emission from the laser plasma and measured the electron densities and temperatures associated with them. The authors observe that highly charged ions are detectable in the plasma and that the plasma itself shows structure in terms of emission at different distances from the target surface. Comments on the equilibrium state of the laser plasma and its transient nature form one of the salient points expressed by the authors.

The first highly detailed study on laser plasmas for use as an analytical method was produced by Scott and Strasheim in 1970. This study was the first to use a time-resolved or 'gated' detector to observe the expansion dynamics of the laser plasma. A gated detector is, essentially, a normal detector with a high-speed shutter attached to the face. This allows the temporal evolution of an expanding plasma (or indeed any other phenomenon that changes over time) to be studied at different stages of its lifetime. The result of this study showed some of the temporal and spatial characteristics of a laser-produced plasma as it expands - the authors essentially conclude that the expansion is hydrodynamic in nature and that several complex energy transfer mechanisms occur in the early stage of plasma ignition. The final part of this paper suggests that calibration curves can be obtained from spatially and temporally resolved areas of the plasma, and attempts to do so for copper analysis in aluminium alloys.

Another paper by Scott and Strasheim (1971) details a study using what is approaching the most common form of experiment used in modern LIPS research - a time-resolved detection system used to collect the radiation accumulated from more than one laser-produced plasma. In this case, the material under analysis was aluminium, with the behaviour of copper spectral lines being observed. This paper records the influences of crater depth on target spectra when many shots have been fired on the same spot, the effect of the number of shots on the spectra and also a so-called "3rd partner" effect - now known as the "matrix" effect where an element not

under direct observation can affect spectral lines emitted by the analyte. The paper concludes by noting that as the technology of both sources and detection system improves, the stability and accuracy of LIPS as a quantitative technique will improve.

In the same year, Piepmeier & Osten (1971) produced a paper outlining the influences of the atmosphere on laser-produced plasmas. This paper is one of the first to attempt an analytical study of changing pressure on both spectra and the plasma plume structure. The authors suggest here that absorption by the atmosphere of incident laser radiation supports a radiation shockwave in the laser plasma, the dynamics of which are dependant on the atmospheric pressure. A study of the crater left after ablation was also made where the authors note that with increasing energy at low pressure, the crater diameter increases along with the mass of target material ejected. At atmospheric pressure (760 Torr), the mass and crater diameter remain uniform across all tested laser energies.

These fundamental studies using the most basic available equipment form the foundation of techniques using lasers as an excitation source for optical emission spectroscopy and are the foundations on which the experiments featured in this thesis are laid. A summary of the physics of laser plasmas can be found in Carroll & Kennedy's 1981 paper which outlined the characteristics of laser plasmas and some of the methods used to diagnose them in terms of emission, temperature and density.

1.2.2 MODERN STUDIES

Although intense research continued on laser plasmas during the 80s, the applications to spectroscopic analysis were limited due to the cost and limited capability of experimental components - especially detectors. Lasers gradually became more and more reliable in terms of operation and shot-to-shot reproducibility of both energy and pulse width meaning that using LIPS as a viable alternative to such techniques as X-Ray Photoelectron Spectroscopy (XPS) and Secondary Ion Mass Spectroscopy (SIMS) became an ever increasingly viable option. Other techniques (known as the "hyphenated" techniques) have used laser plasmas as particle sources for mass and optical spectroscopy. The best known of these are LA-ICP-MS and -OES, both of which use laser plasmas as particle sources for mass and optical spectroscopy. The advantage LIPS has over these are that laboratory equipment used in LIPS experiments is less complex and more adaptable to different types of target. The LIPS technique still lacks some of the sensitivity of these other more common spectroscopic methods however. Typical detection limits are in the low parts per million range for Time-Of-Flight (TOF) SIMS and even extending into the parts per billion (ppb) range (ASM, the American Society for Metals, 2003).

Advances in detectors have seen the CCD (Charge-Coupled Device - see chapter 3) camera become the standard in LIPS experiments as the precision and 2 dimensional imaging capacity of this camera is ideal for a wide range of applications, including LIPS. New areas of study have included ultra-short pulse (femtoseconds and picosecond) lasers with combinations of both different pulses and wavelengths in experiments and also plasma plume evolution using ultra-fast gated (intensified) CCD cameras.

The use of lasers for materials analysis has continued apace with journal reviews and books being regularly published - some examples include Adrain & Watson (1984), Moenke-Blankenberg (1989), Radziemski & Cremers (1989), Majidi & Joseph (1992), Darke & Tyson (1993), Song, Lee & Sneddon (1997), Rusak et al. (1997), Tognoni et al. (2002), Vadillo & Laserna (2004) and finally Cremers & Radziemski (2006). This rather exhaustive list has been accompanied in recent years by a number of conferences dedicated to LIPS, starting in 2000 with the First International Conference on Laser-Induced Plasma Spectroscopy and Applications hosted in Pisa, Italy. Both international and European conferences have been hosted every alternate year since, indicating an increasingly substantial volume of research into the area internationally. Theoretical and experimental studies into laser ablation and LIPS have been presented in the literature (summarised by the above list of reviews and books) and at the various LIPS conferences.

The main outcome from these conferences has been the realisation that studies in the technique can be divided into several smaller and more focused areas. These can be loosely divided into fundamental studies of the laser-matter interaction, quantification of materials being analysed, novel instrumentation for the improvement of the technique, process control in analysis and both lab and field sample analysis. The wide array of samples in solid, liquid and gas form and also the various conditions in which they are analysed has been huge - from applications in artwork restoration (Anglos, Cours & Fotakis, 1997) to mine detection (Schade et al., 2006) to the possible inclusion of a VUV-sensitive LIPS instrument on the proposed 2009 NASA Mars rover mission (Radziemski et al., 2005).

There are a number of reasons as to why LIPS has emerged as an important tool for elemental analysis.

- It involves little or no target preparation
- It can be performed as an "online" technique in industrial manufacturing i.e. it can be performed while materials such as steel and aluminium are being manufactured

- LIPS is a comparatively non-destructive technique - sub millimetre craters indicate the remnants of a LIPS-based inspection
- Analysis times can be very low - turnaround times of no more than a few seconds are available on some commercially available LIPS systems
- For the heavier elements ($Z > 20$), limits of detection can be very low i.e. below ppm, with the corresponding accuracy of measurements quite high - appendix C in Cremers & Radziemski (2006) has a comprehensive library of detection limits for all studied elements in all matrices
- The versatility of the technique means that elements in a solid, liquid or gaseous state in a variety of environments can be analysed
- The use of picosecond and shorter laser pulse lengths means that surface analysis can be performed since the thermal penetration depth of these laser pulses is low (see chapter 2)

Elements with an atomic number of less than 20 ($Z < 20$) are difficult to analyse in most modern LIPS experiments as these are usually either visible- or UV-based. The lighter elements have their strongest and resonant emission lines in the VUV region of the spectrum (Samson, 1967) - a region generally neglected since air is a strong VUV absorber. Most studies on lighter elements to date have used emission lines in the UV region for both qualitative and quantitative analysis - this has limited the effectiveness of the technique as a result. The most successful studies on light elements to date have used emission lines in the near-VUV, the lower wavelength limit being about 180 nm. Another important advantage of using VUV emission lines is the existence of a number of spectral "windows" - these are areas of the spectrum where few if any of the bulk material's emission lines lie. This can eliminate the so-called "matrix effect" where suitable emission lines have been overcrowded by lines from the bulk element.

Many of the studies on these lighter elements have been performed on steels and other industrially important materials since some of the lighter elements have large influences on the properties of metal. Iron and steel in particular are affected by four elements in particular - carbon, nitrogen, phosphorus and sulphur (Turkdogan, 1996). Whereas carbon and nitrogen can enhance the toughness and hardness of steel, sulphur has a negative effect on several key properties: the ductility of the steel, the low temperature toughness and the fatigue strength. Sulphur is sometimes added to specific grades of steel to improve the machinability of steel for certain applications but in general, desulphurisation of steel is an important part of the steelmaking process. One of the starkest examples of the negative effects of sulphur

in steel is the sinking of the R.M.S. Titanic in 1912. Tests conducted on salvaged steel from the ship's hull have shown a relatively high level of sulphur present in it - a sulphur concentration of 0.69% was determined by Felkins, Leighly Jr. & Jankovic (1998). A Charpy test (a standardised test to determine the brittleness of steel) resulted in a straight fracture of the recovered steel in comparison to a buckling and tearing in modern, low-sulphur steel (Gannon, 1995). It is surmised that on the night when the Titanic hit the iceberg in the North Atlantic, the combination of high sulphur and low temperature resulted in the shattering of the hull at the contact point rather than a deformation and bending of the steel.

Steel standards have since improved, with increased control over contaminants found in the material. The current most widely used method for trace element monitoring is spark-discharge spectroscopy (spark-OES). This is a similar method to LIPS but instead of using a laser to generate a plasma, highly energetic electrons are used. Infrared absorption via combustive techniques is also used for determination of carbon, nitrogen and sulphur in steel. Both of these methods necessitate a degree of target preparation before analysis is performed which leads to delays in the manufacturing process (Hemmerlin, 2001). As such, the potential for LIPS to be used as an online monitoring process has not gone unnoticed. It has the capacity to provide real time observation of both the type and quantity of contaminants in steels both in the bulk material and, using short-pulse (less than 100 picoseconds) lasers, a surface analysis capability as well (Vadillo & Laserna, 2004).

1.2.3 LIPS FOR THE ANALYSIS OF SULPHUR IN STEELS

The first study of sulphur inclusions in steel samples using the LIPS technique was performed by Gonzalez, Ortiz and Campos in 1995. This study used neutral sulphur lines in the near VUV region at 180 and 182 nm in determining the sulphur content of the samples and resulted in a detection limit of 70 ppm (parts per million) of sulphur. A time-resolved detector system, an Optical Multichannel Analyser (OMA III, EG&G), was used to make these measurements. More studies followed, the next being that of Sturm, Peter and Noll in 2000. Again, time resolution was used to make the measurements, in this case a time-resolved photomultiplier tube in conjunction with a fast oscilloscope. The neutral sulphur line at 180 nm was again used but with far better accuracy this time - a limit of detection of 8 ppm was achieved. A LIPS system used in a pipe making plant in Germany was reported on in 2001 by Noll et al. This reported progress on research conducted in an industrial environment where LIPS was being actively used in process control for the analysis of carbon,

phosphorus and sulphur in steel. The advantages of LIPS as a non-destructive online technique were reported, along with the machine's limit of detection for sulphur of 21 ppm. A wide scale extension of this research was reported in 2002 by Bulajic et al. which introduced the EU funded LIBSGRAIN project. This project's aim was to improve analysis of industrial component failure using the LIPS technique. The conclusion of this report was that LIPS should be rapidly developed as an industrial process control technique.

The most sensitive application to date of the LIPS technique in sulphur analysis has been made by Hemmerlin et al. in 2001 when comparing figures of merit with those obtained using the standard spark-OES technique most commonly used in steel plants. This again used time resolution in the analysis of steel samples with optimisation of the signal to background ratio by adjusting both the gate delay and width. Emission lines as low as 133 nm were used for elemental analysis with VUV lines again being used for the lighter elements. A lower sulphur detection limit of 4.5 ppm was reported in comparison to the lower limit of 3 ppm using the spark-OED technique. This report also included single figure detection limits for both carbon and phosphorus,

Since this publication, work has continued apace at improving the accuracy and reliability of the LIPS technique with studies being performed on industrial and laboratory samples, although no improvements in the detection limit for sulphur have been published. VUV lines have been used almost exclusively in these studies as they offer the best intensities and also the clearest lines in comparison to the background and bulk emission from the target. Publications in 2003 and 2004 by Peter (2003), Sturm (2004) and Radivojevic (2004) have all shown improvements in the characterisation of multiple elements using various LIPS systems in conjunction with ICCD cameras; however, none have improved on the basic detection limit published by Hemmerlin in 2001.

An alternative to the temporally-resolved studies which had previously dominated the literature was introduced in 2000. A new type of spatially-resolved experiment was designed independently by 2 separate groups in which the spatial structure of a laser-produced plasma was exploited rather than the temporal characteristics. The basic problem both techniques try to overcome is the strong, continuum-dominated emission which occurs early on in the plasma's lifetime and also lies close to the target surface (see chapter 3). This approach also decreases the overall costs involved in experiments, since time-resolved detectors are more complex and expensive than time-integrated detectors. The spatially-resolved approach has been used to great effect in the past for the analysis of solid materials.

The first published study was a basic investigation into the feasibility of the spatially-resolved variant by Bulatov, Krasniker & Schechter in 2000. The publication shows a comparison between spatial and temporal resolution for the analysis of zinc in brass samples which uses an array of optical fibres positioned parallel to the laser plasma's expansion axis to discriminate between spectra recorded at the various distances from the target. The paper concludes by stating that temporal resolution is a better technique for the elements concerned; however, this study was limited to a wavelength region of 450 - 490 nm

The first spatially-resolved deep VUV study of light elements in steels was conducted by Khater et al. in 2000. This study was the first to show the feasibility of using spectral lines deep in the VUV *and* a spatially-resolved set up to analyse the concentration of carbon in steel samples. The type of spatial resolution was markedly different to that used by Bulatov, Krasniker & Schechter (2000) as optical fibres are not suitable for the transmission of VUV radiation. It also presented the possibility of studying ions, whereas the standard LIPS approach is to use lines neutral and sometimes singly-charged atomic species. This paper showed that carbon lines between 60 and 100 nm were quite suitable for elemental analysis and produced a detection limit of 87 ppm using a carbon line at 97.7 nm. A further extension of this paper was published in 2002 (again by Khater et al.) which used ambient gases to enhance the signal to background values for the VUV carbon lines. This paper produced an unprecedented detection limit of 1.2 ppm, a limit which has stood unbroken since. In 2006, a spatially-resolved system was used to quantitatively analyse the aluminium and zinc concentrations in nickel-based alloys (Tsai et al., 2006). This had a comparison between time and space-resolved LIPS which showed again that space resolution provides an effective alternative to time resolution.

1.3 AIMS AND OBJECTIVES OF THE PRESENT WORK

The goal of this body of work is to improve the detection limit for sulphur in steel by using emission lines in the deep VUV i.e. between 60 and 120 nm. This was investigated using space-resolved spectroscopy where the spatial structure of a laser-produced plasma was exploited rather than time-resolved spectroscopy as an alternative to the more common technique. A number of steel samples with varying concentrations of sulphur ranging from 0.0027% to 0.68% were used as analytical standards with which to construct calibration curves from spectral data. A modern Q-switched Nd:YAG laser was used to generate the laser plasma. Targets were

mounted in a custom-built vacuum chamber with the radiation generated from the laser plasma collected and dispersed by a 1 metre normal incidence VUV spectrometer fitted with a 1200 lines/mm reflective concave grating. The spectra were recorded using a VUV sensitive CCD camera.

The process by which the main goal of the thesis was accomplished can be summed up as follows.

- A spectral survey of the VUV region was performed in order to ascertain which of sulphur's spectral lines were suitable for concentration analysis.
- The conditions in which spectra are recorded for use in the LIPS analysis were optimised in vacuum conditions. This was done by systematic modification of a number of experimental parameters including laser energy, laser focus, the distance at which spectra were recorded and the type of lens used in generating the laser plasma.
- Changes in the emission characteristics of the laser plasma with the addition of several different ambient gases in the target chamber were investigated with the results compared to the optimisation study performed in vacuum. A new optimisation of the experimental parameters was conducted after partially optimised atmospheric conditions were established.
- Calibration curves were constructed at optimised conditions in both vacuum and in an ambient atmosphere using 2 different methods. Comparisons were made to contemporary detection limits and figures of merit from the available published literature.

1.4 SUMMARY

Laser-Induced Plasma Spectroscopy is an important developing technique for elemental analysis. Many theoretical and experimental studies have been directed at the analysis of elements in all forms and the physical processes involved in their ablation with focused laser energy. Although many of these have been successful, there has been a shortcoming particularly in the analysis of light elements (including sulphur) due to the difficulty involved in finding suitable emission lines as the strongest resonance emission lines are primarily located in the VUV region of the spectrum. This region is not readily accessible using standard equipment due to the fact that air is a strong VUV absorber

A proposed series of experiments have been outlined for the quantification of sulphur in steel samples using time-integrated space-resolved laser-induced plasma spectroscopy. The stated goal of these experiments is to investigate the emission characteristics of atomic sulphur species in a spatially-resolved manner with the intention of optimising the spectra obtained for use in calibration curves for low-level sulphur detection and quantification.

REFERENCES

- Adrain RS & Watson J: "Laser Microspectral Analysis: A Review of Principles and Applications", *Journal of Physics D: Applied Physics*, **17**, pp. 1915 - 1940 (1984).
- Anglos D, Couris S & Fotakis C: "Laser Diagnostics of Painted Artworks. Laser-Induced Breakdown Spectroscopy in Pigment Identification", *Applied Spectroscopy*, **51**, pp. 1025 - 1030 (1997)
- ASM - (The American Society for Metals): *ASM Handbook Volume 11: Failure Analysis and Prevention*, ASM International, 2003.
- Brech F & Cross L. "Optical Microemission Stimulated by a Ruby Maser", *Applied Spectroscopy*, **16**, no.2, p. 59 (1962).
- Bulajic D et al.: "Diagnostics of High-Temperature Steel Pipes in Industrial Environment by Laser-Induced Breakdown Spectroscopy Technique: the LIBSGRAIN Project", *Spectrochimica Acta Part B*, **57**, pp 1181 - 1192 (2002).
- Bulatov V, Krasniker R & Schechter I: "Converting Spatial to Pseudotemporal Resolution in Laser Plasma Analysis by Simultaneous Multifiber Spectroscopy", *Analytical Chemistry*, **72**, pp 2987 - 2994 (2000).
- Burgess DD, Fawcett BC & Peacock NJ: "Vacuum Ultra-Violet Emission from a Laser-Produced Plasma", *Proceedings of the Physical Society*, **92**, pp. 805 - 816 (1967).
- Carroll PK & Kennedy ET. "Laser-Produced Plasmas", *Contemporary Physics*, **22**, pp. 61 - 96 (1981).
- Cremers DA & Radziemski LJ: *Handbook of Laser-Induced Breakdown Spectroscopy*, Wiley, 2006.
- Darke SA & Tyson JF: "Interaction of Laser Radiation with Solid Materials and its Significance to Analytical Spectroscopy: A Review", *Journal of Analytical Atomic Spectrometry*, **8**, pp. 145 - 209 (1993)
- Felkins K, Leighly Jr. HP & Jankovic A: "The Royal Mail Ship Titanic: Did a Metallurgical Failure Cause a Night to Remember?", *JOM*, **50**, pp. 12 - 18 (1998).
- Gannon R: "What Really Sank the Titanic," *Popular Science*, **246**, pp 49-55 (1995).
- Gonzalez A, Ortiz M & Campos J:"Determination of Sulphur Content in Steel by Laser-Produced Plasma Atomic Emission Spectroscopy", *Applied Spectroscopy*, **49**, pp. 1632 - 1635 (1995).
- Hemmerlin M et al.: "Application of Vacuum Ultraviolet Laser-Induced Breakdown Spectrometry for Steel Analysis - Comparison with Spark-Optical Emission Spectrometry Figures of Merit", *Spectrochimica Acta Part B*, **56**, pp. 661 - 669 (2001).

- Khater MA et al: "Time-Integrated Laser-Induced Plasma Spectroscopy in the Vacuum Ultraviolet for the Quantitative Elemental Characterization of Steel Alloys", *Journal of Physics D: Applied Physics*, **33**, pp. 2252 - 2262 (2000).
- Khater MA et al: "Optimization of the Emission Characteristics of Laser-Produced Steel Plasmas in the Vacuum Ultraviolet: Significant Improvements in Carbon Detection Limits", *Applied Spectroscopy*, **56**, pp. 970 - 983 (2002).
- Maiman TH: "Stimulated Optical Radiation in Ruby", *Nature*, **187**, no. 4736, pp. 493 - 494 (1960).
- Majidi V & Joseph MR: "Spectroscopic Applications of Laser-Induced Plasmas", *Critical Reviews in Analytical Chemistry*, **23**, pp. 143 - 162 (1992).
- Moenke-Blankenberg L: *Laser Microanalysis*, Wiley, 1989.
- Peter L, Sturm V and Noll R: "Liquid Steel Analysis with Laser-Induced Breakdown Spectrometry in the Vacuum Ultraviolet", *Applied Optics*, **42**, pp. 6199 - 6204 (2003).
- Piepmeyer EH & Osten DE "Atmospheric Influences on Q-Switched Laser Sampling and Resulting Plumes", *Applied Spectroscopy*, **25**, pp. 642 - 652 (1971).
- Radivojevic I et al.. "Microanalysis by Laser-Induced Plasma Spectroscopy in the Vacuum Ultraviolet", *Analytical Chemistry*, **76**, pp. 1648 - 1656 (2004).
- Radziemski LJ & Cremers DA. *Laser-Induced Plasmas and Applications*, Dekker, 1989.
- Radziemski LJ et al.. "Use of the Vacuum Ultraviolet Spectral Region for Laser-Induced Breakdown Spectroscopy-Based Martian Geology and Exploration", *Spectrochimica Acta Part B*, **60**, pp.237 - 248 (2005).
- Runge EF, Minck RW & Bryan FR: "Spectrochemical Analysis Using a Pulsed Laser Source", *Spectrochimica Acta*, **20**, pp. 733 - 736 (1963).
- Runge EF, Bonfiglio S & Bryan FR: "Spectrochemical Analysis of Molten Metal using a Pulsed Laser Source", *Spectrochimica Acta*, **22**, pp. 1678 - 1680 (1966).
- Rusak DA et al.: "Fundamentals and Applications of Laser-Induced Breakdown Spectroscopy", *Critical Reviews in Analytical Chemistry*, **27**, pp. 257 - 290 (1997).
- Samson JAR: *Techniques of Vacuum Ultraviolet Spectroscopy*, Wiley, 1967.
- Schade W et al.: "Laser-Induced Plasma Spectroscopy for Mine Detection and Verification", *Laser and Particle Beams*, **24**, pp. 241 - 247 (2006).
- Scott RH & Strasheim A: "Laser Induced Plasmas for Analytical Spectroscopy", *Spectrochimica Acta*, **25B**, pp. 311 - 332 (1970).
- Scott RH & Strasheim A: "Spectrochemical Analysis using a Laser Source with a Medium-Pulse Repetition Rate", *Spectrochimica Acta*, **26B**, pp. 707 - 719 (1971).
- Song K, Lee YI & Sneddon J. "Applications of Laser-Induced Breakdown Spectrometry", *Applied Spectroscopy Reviews*, **32**, pp. 183 - 235 (1997)

- Sturm V, Peter L & Noll R: "Steel Analysis with Laser-Induced Breakdown Spectrometry in the Vacuum Ultraviolet", *Applied Spectroscopy*, **54**, pp 1275 - 1278 (2000).
- Sturm V et al.: "Bulk Analysis of Steel Samples with Surface Scale Layers by Enhanced Laser Ablation and LIBS Analysis of C, P, S, Al, Cr, Cu, Mn and Mo", *Journal of Analytical Atomic Spectrometry*, **19**, pp 451 - 456 (2004).
- Tognoni E et al. "Quantitative Micro-Analysis by Laser-Induced Breakdown Spectroscopy: A Review of Experimental Approaches", *Spectrochimica Acta Part B*, **57**, pp 1115 - 1130 (2002)
- Turkdogan ET: *Fundamentals of Steelmaking*, Woodhead, 1996.
- Vadillo JM & Laserna JJ: "Laser-Induced Plasma Spectrometry: Truly a Surface Analytical Tool", *Spectrochimica Acta Part B*, **59**, pp 147 - 161 (2004)

CHAPTER II: THEORY OF LASER PLASMAS

In this chapter, a brief summary of the major aspects of laser plasma physics is presented in order to enable a fundamental understanding of the complex processes involved. Emphasis is given to the interaction of the laser pulse with the target, expansion of the plasma and to atomic processes occurring in the plasma before its thermodynamic death. The basic premise for using laser plasmas for elemental detection is also explained in order to validate the LIPS technique.

2.1 INTRODUCTION

When Brech & Cross (1961) performed the first experiment using a Ruby laser as a plasma ignition source, the world of physics was introduced to a fascinating field of study: laser plasma physics. The interaction of a large and highly focused number of photons with a material is a very complex process, the conditions of which are still subject to substantial debate and study today. Changing parameters in the creation of the plasma have well-documented effects on the subsequent laser plasma expansion and emission. Variations in the initial conditions of the laser plasma such as the initial laser pulse energy, cratering of the target from previous shots and the effects of an expansion into an ambient gas affect the laser plasma during its relatively short lifetime. However, with the same initial conditions, laser plasmas can be replicated with only very slight deviations - experiments can be repeated and verified independently with high degrees of reproducibility. For most experiments, this is an important pre-requisite to any body of work; for a technique aimed at elemental quantification, this takes on an even greater urgency. Experimental conditions that can't be repeated and subject to use and examination elsewhere are of no practical use.

In order to fully understand laser plasma physics, a short explanation of what constitutes a plasma is necessary. Since the subject matter has been delved into extensively (Hughes (1975), Bekefi (1976), Carroll & Kennedy (1981) and Cremers & Radziemski (1989) to name but a few), it is not my intention to provide an extensive review of laser plasma physics, merely to provide a brief exposition of the basic principles and processes.

2.2 GENERAL CHARACTERISTICS OF PLASMAS

A plasma is basically a hot gas whose atoms and ions react in several unusual ways to outside influences such as electric and magnetic fields. The definition of a plasma is that it is "a quasineutral gas of charged and neutral particles exhibiting collective behaviour" (Chen, 1984). This statement can be broken down into several parameters, each of which is necessary to redefine an ionised gas as a plasma.

Firstly, the term "quasineutral" refers to the fact that in a typical plasma, the numbers of positive and negative charges are roughly equal i.e. $n^+ \approx n^-$ (the number

of positive charges refers to the number of ions in the plasma multiplied by their charge state i.e. C^{2+} is doubly charged, and therefore has 2 positive charges). The free electrons in the plasma are mobile enough that they can "shield" the plasma from external fields so that the bulk plasma remains largely unaffected. This shielding is called Debye shielding and the sheath around a field source called the plasma sheath. The first criterion for an ionised gas to be treated as a plasma is

$$\lambda_D \ll L \quad [2.1]$$

where λ_D is the length of the sheath (Debye length) and L is the length of the plasma. λ_D can be calculated using the following:

$$\lambda_D \equiv \left(\frac{\epsilon_0 k T_e}{n e^2} \right)^{\frac{1}{2}} = 69 \left(\frac{T}{n} \right)^{\frac{1}{2}} = 7430 \left(\frac{kT}{n} \right)^{\frac{1}{2}} \quad [2.2]$$

In equation [2.2], ϵ_0 is the permittivity of free space, k is Boltzmann's constant, T_e is the average electron temperature in the plasma, n the density of particles in the plasma and e is the electron charge. In the first simplification, T is measured in Kelvin while in the second kT is measured in eV

The second criterion is that the charged particles in the plasma must be close enough to exert force on more particles than just its neighbour. The "Debye sphere" is a measure of the number of charged particles N_D within the sphere of influence of a particle at the centre of the sphere and is calculated by:

$$N_D = \frac{4}{3} \pi \lambda_D^3 n \quad [2.3]$$

The second of the criteria regarding collective behaviour is therefore

$$N_D \gg 1 \quad [2.4]$$

The last of the parameters for an ionised gas to be treated as a plasma relates to inter-particle collisions in the plasma itself. If the charged particles collide too frequently with neutrals, then the motion of the charged particles are governed more by hydrodynamic effects rather than electromagnetic forces. If we take ω (known as the plasma frequency) as the oscillation frequency of electrons in the plasma and τ as the average time between collisions with neutral particles, then for a plasma to act rapidly in shielding out foreign fields the following must be observed:

$$\omega \tau > 1 \quad [2.5]$$

In other words, the collision frequency of particles in the plasma must be far less than the plasma frequency

2.3 LASER PLASMA FORMATION

When the output pulse from a Q-switched laser is focused onto a solid surface, a high density, high temperature plasma is formed. This happens via radiation absorption by the target on its surface with subsequent phase changes in the bulk material occurring when the initial pulse energy is redistributed through electron collisions in the material lattice. The relaxation times of these collisions are of the order of 10^{-12} - 10^{-13} seconds (Hughes, 1975), far shorter than the laser pulse durations in this body of work which are of the order of nanoseconds. A basic diagram of the laser absorption process can be viewed in Figure 1 (after Eliezer, 2002).

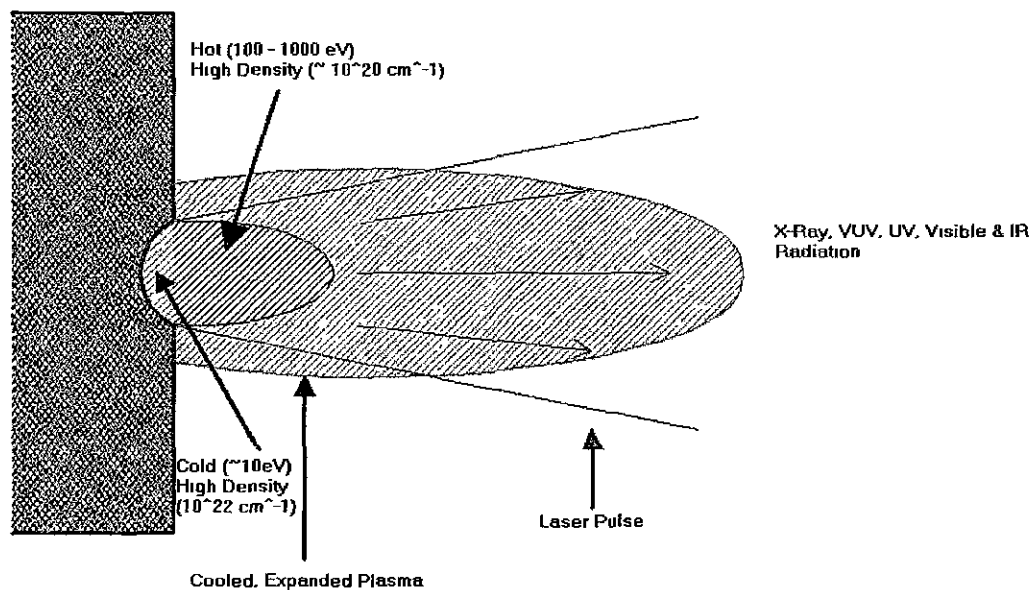


Figure 1. Laser Plasma Formation (after Eliezer, 2002)

The depth to which the laser pulse penetrates the target is called the *optical skin depth* (δ_{OPT}), and is dependent on both the material's physical characteristics and the type of radiation incident on it (Scott & Strasheim, 1970). It can be computed using:

$$\delta_{OPT} = \sqrt{\frac{2}{\omega\mu\sigma}} \quad [2.6]$$

In the above, ω is the angular frequency of the laser radiation, μ is the magnetic permeability of the material and σ is the conductivity of the target material. In the case of a target composed mainly of iron and a Nd:YAG laser operating at its fundamental frequency (1064 nm), the optical skin depth is about 9.5 nm. As

previously stated, the optical energy is propagated through the target via collisional relaxation. For a laser pulse of duration τ , the *thermal penetration depth* δ_{TH} into the target can be estimated by

$$\delta_{TH} = \sqrt{2 \left(\frac{K}{\rho C} \right) \tau} \quad [2.7]$$

In this equation, K is the material's thermal conductivity, ρ is the density and C is the specific heat capacity. The thermal penetration depth of a 6 ns laser pulse into an iron target is therefore about 520 nm, significantly higher than the optical skin depth. In the case of shorter pulse lasers (e.g. Titanium Sapphire lasers have pulse lengths of the order 10 femtoseconds to a few picoseconds), target craters are often much cleaner (Vadillo & Laserna, 2004) than ns pulses since the short pulse length effectively "scoops" material out of the target and isn't subject to the vagaries of thermal ablation in the same manner.

There is an energy threshold in the ablation process, below which material ablation will not occur (Moenke-Blankenberg, 1989). The *fluence* on the target surface is the amount of energy per unit area incident on a target. Material begins to be ablated when the energy absorbed by the target exceeds the latent heat of vaporisation of the material, L_v . This threshold is given by:

$$F_{Th} = \rho L_v \sqrt{\frac{K}{\rho C} \tau} \quad [2.8]$$

Note that the above stated threshold is sufficient for material vaporisation only; the ionisation process requires enhanced absorption of the laser beam. The threshold fluence for a 6 ns pulse incident on an iron target is calculated to be about 1.4 J/cm². If we take the *power density* to be the fluence divided by the pulse duration, we see that the minimum power density on target required for material ablation is about 2.4 x 10⁸ W/cm². This figure is easily achieved by focusing a laser pulse onto a target. Power densities of up to 10¹² W/cm² may be achievable using short focal length (< 20 cm) lenses to focus pulses from a modern, Q-switched laser

During the ablation process, some atoms are ionised by the incoming radiation. Considering that each photon from a Nd:YAG laser has an energy of about 1.2 eV and that the ionisation potential of even the most readily ionised element (Caesium, with an ionisation energy of 3.9 eV) is more than 3 times higher than this energy, clearly there is some other process involved in the initial electron liberation. One of the processes is known as *Multi-Photon Ionisation* (MPI). This happens when an electron absorbs several photons simultaneously (or almost simultaneously - Radziemski & Cremers, 1989) and climbs out of the potential in the atom with

resultant energy $E = 1/2mv^2$. Quantum tunnelling through the potential well of the atom is also cited as a source of free electrons in the ablated material.

The material ablated from the target surface is now a comparatively cold and thin layer of weakly ionised atoms, ions and electrons formed in the first few optical cycles of the laser pulse (Carroll & Kennedy, 1981) known as a *pre-plasma*. The R.M.S. electric field strength of the laser pulse at the target surface in terms of the fluence ϕ is enormous - it is given by

$$\bar{E} = 19.4\sqrt{\phi} \quad [2.9]$$

For a laser pulse with a power density of 10^{10} W/cm², the equivalent electric field would be nearly 2×10^6 V/m. Once this cold and dense layer has been formed, the free electrons in the pre-plasma start to absorb energy from the remaining part of the laser pulse by a mechanism called *Inverse Bremsstrahlung absorption*.

Inverse Bremsstrahlung absorption is a process whereby free electrons absorb photons from the laser beam when they collide with an ion or neutral particle (Eliezer, 2002). Free electrons in the plasma are unable to absorb laser light (Ready, 1971) as the principles of conservation of momentum and energy cannot be simultaneously satisfied unless there is a third, colliding particle present. When the electron is in the electric field of an atom or ion however, momentum is easily conserved across the transient system since the additional particle can change direction.

While the plasma is still in its initial stages, a high percentage of light can pass through the plasma and onto the target surface, so more and more material is ablated. The laser beam suffers from increasing attenuation as the plasma becomes denser however, due to increasing number of free electrons involved in collisional absorption. This continues until the electron density in the plasma has reached a critical value, the *critical density* n_c :

$$n_c = \frac{m_e \omega^2}{4\pi e^2} \cong 1.1 \times 10^{21} \left(\frac{1 \mu m}{\lambda^2} \right) cm^{-3} \quad [2.10]$$

in which m_e is the electron mass, ω is the frequency of the laser radiation, e is the electron charge and λ is the laser wavelength measured in μm . The critical density for radiation at about $1 \mu m$, the fundamental frequency of a Nd YAG laser, is about $10^{21} cm^{-3}$. When the plasma density reaches this value, the incident laser radiation is primarily absorbed by the plasma near the critical density zone. In this phase of the laser pulse, the plasma starts to expand rapidly away from the target surface. This expansion reduces the electron density, and laser light is once more able to pass

through to the target surface relatively undiminished. This cyclical process continues until the laser pulse ceases - at this point, the plasma no longer has an external energy source, and atomic processes dominate energy transfer in the plasma.

2.4 ATOMIC PROCESSES IN LASER PRODUCED PLASMAS

There are 3 main groups of atomic process in laser plasmas which are composed of a process and its inverse: free-free, free-bound and bound-bound. The primary process involves net energy loss to the particles involved, while its inverse involves net energy gain. Both radiative and collisional interactions can account for energy transfer in both cases. A short explanation of each follows in the next few sections.

2.4.1 FREE-FREE PROCESSES

Free-free processes are where two or more particles are involved in an interaction after which they remain free, as shown in Figure 2.

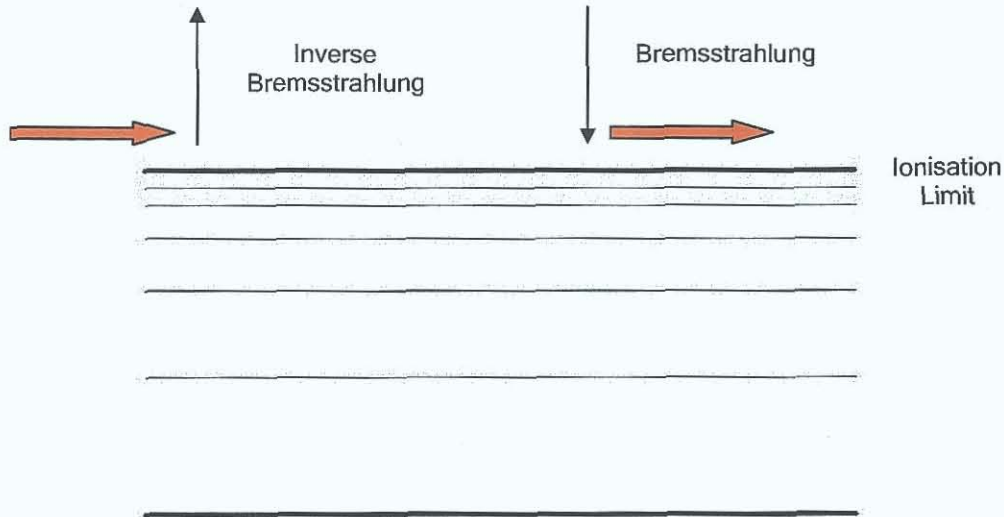


Figure 2: Free-Free Radiative Processes

Bremsstrahlung radiation is caused by collisions between free electrons and ions or neutrals. In these collisions, the electrons lose kinetic energy in the form of broadband radiation. This type of broadband radiation is one of the most characteristic signatures of a laser-produced plasma. The source of this radiation is

mainly due to free electron interactions with ions or neutral species in the laser plasma although in some complex atomic systems, the complicated level structure of ions in a laser plasma can lead to recombination (free-bound) transitions emitting continuum radiation. For example, O'Sullivan et al (1999) shows that open 4f subshells in rare earth metals contribute greatly to continuum emission in laser plasmas.

Bremsstrahlung radiation occurs mainly during the early stages of the laser plasma's lifetime; spatially it lies close to the target's surface. It can be represented by the pseudo-equation (using X for the ion or neutral, e^* or e^{**} for a free electron with kinetic energy greater than the ionisation energy of the atomic species and $h\nu$ for a photon):

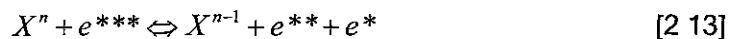


The inverse process (responsible for heating and ionisation in the formation of the plasma) is inverse Bremsstrahlung, as previously described. This interaction can be described as



2.4.2 FREE-BOUND PROCESSES

Free-bound processes can happen in one of two ways, both collisionally and radiatively. In collisional ionisation, an electron collides with an atom or ion, with the result that another electron is ionised from the parent particle, while the exciting electron remains free, albeit with less kinetic energy. Collisional de-excitation (or 3-body recombination) involves a collision between an electron and an ion resulting in the electron dropping into the ion's potential well, with the excess energy absorbed by a free electron in close proximity. These processes are shown as:



In the above, the left side of the equation is the de-excited state while the right is the excited state. The radiative forms of the free-bound processes are photoionisation (the photoelectric effect) and radiative recombination, illustrated in Figure 3 on the following page.

Photoionisation happens when a photon of energy greater than the ionisation potential of the atom or ion is absorbed by an electron. The electron then has enough energy to escape the potential well and leaves the parent particle having energy

$$E = \frac{1}{2}mv^2 = h\nu - E_i \quad [2.14]$$

where $\frac{1}{2}mv^2$ is the kinetic energy of the electron, $h\nu$ is incident the photon energy and E_i is the ionisation potential of the atom/ion. Equation [2.15] below shows the energy transfer process.

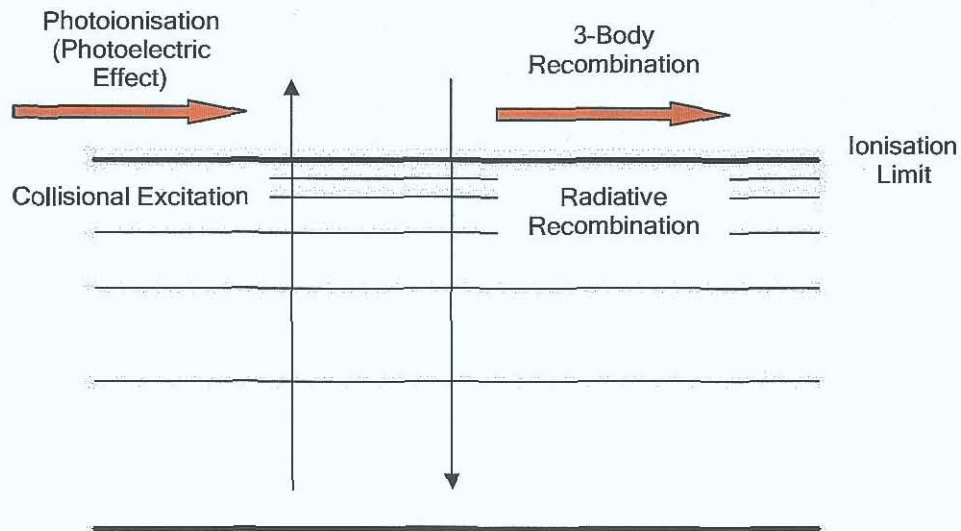


Figure 3: Free-Bound Processes

As we can see, radiative recombination is simply the absorption of an electron into an ion with the surplus energy emitted as a photon. The radiation emitted in this process is also indistinct i.e. spread over many wavelengths and not of fixed energy. In general, free-bound processes occur at intermediate times in the plasma lifetime i.e. when the plasma is in transition from continuum-dominated radiation to line-dominated.

2.4.3 BOUND-BOUND PROCESSES

Bound-bound interactions are responsible for the discrete line emission from the various atomic species in the plasma. Mainly occurring when the bulk of the plasma has cooled significantly from the initial formation, line radiation from the plasma is used mostly for plasma diagnostics and also during LIPS studies. These processes again consist of radiative or collisional interactions. The collisional interactions are very simply "billiard ball" type interactions - 2 atomic species collide with each other with a net energy loss to one particle and a corresponding gain to the other. Collisional de-excitation is the simple inverse of this - an excited electron drops into a free orbital with the surplus energy transferred to the colliding particle in the

form of excitation into a higher energy state. Both processes are shown below in [2.16]:



The radiative bound-bound processes are identical to the collisional ones, with the only difference being that the energy source for the excitation is a photon, seen in Figure 4. The radiative transitions can be shown as:



and are shown in Figure 4 below.

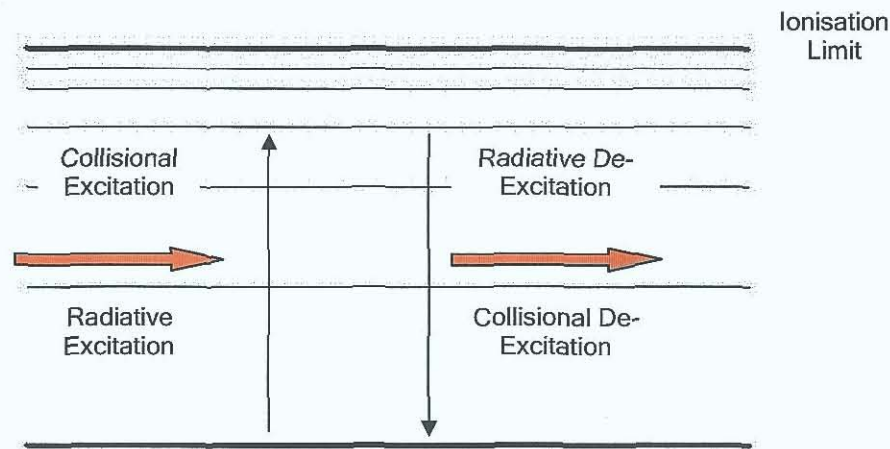


Figure 4: Bound-Bound Processes

2.5 QUANTITATIVE SPECTROSCOPY USING LASER PLASMAS

In order to use the emission from laser-produced plasmas for quantitative spectroscopy, some property of the laser plasma must be intrinsically dependent on the quantity of element under study. In the specific case of laser-produced plasmas, two main methodologies are applied - atomic absorption spectroscopy (AAS) and atomic emission spectroscopy (AES). The basic premise to AAS is that atomic and molecular species in various different states of ionisation will absorb photons at discrete wavelengths depending on the species' electronic structure in the same way that atomic species have a "fingerprint" in the emission under various states of excitation. This corresponds to radiative excitation, shown in Figure 4. AES uses the opposite mechanism, using the hot plasma as an excitation source and essentially waiting for the plasma to cool down and transit from a continuum-dominated emission state to a line-dominated emission state i.e. from continuum dominated to radiative

de-excitation dominated. How this state relates to the concentration of elemental contaminants can be explained as follows

Consider a laser-produced plasma in Local Thermal Equilibrium (LTE - see Appendix A: Equilibrium in Plasmas) of depth X and at temperature T viewed along the optical axis of a measuring instrument. The specific intensity of a spectral line at a frequency ν is defined as the energy emitted from the plasma per unit time, surface area, solid angle and frequency. So, the change in the intensity of a line along a specific optical axis can be expressed by the equation of radiative transfer (after Kim, 1989):

$$\frac{dI(\nu)}{dx} = K(\nu)[B(\nu, T) - I(\nu)] \quad [2.18]$$

In this equation, x is the optical axis along which the plasma is observed and $B(\nu, T)$ is Planck's blackbody function. When this equation is integrated with respect to x between two imaginary planes X distance apart i.e. along the entire length of the plasma on the x axis, we can obtain:

$$I(\nu) = B(\nu, T)[1 - e^{-K(\nu)X}] \quad [2.19]$$

The term $K(\nu)X$ is a measure of the optical thickness of the plasma at the emitting frequency along the path length X . Equations [2.18] and [2.19] are dependent on the assumption that there is no external radiation source outside the bounds of the plasma. When this value is low, the plasma is considered to be optically thin. For laser plasmas in a line-dominated regime, this is typically the case for small concentrations of contaminants in the target, and is a valid assumption in most LIPS applications where detection limits and low concentrations are under study. When the laser plasma is optically thick, it can be treated as a blackbody surface at temperature T .

Normal practice in spectroscopy is to measure the integrated intensity of a spectral line with a central frequency of ν_0 rather than the peak intensity. The integrated intensity is.

$$I = \int_{\nu_0 - \infty}^{\nu_0 + \infty} I(\nu) d\nu \quad [2.20]$$

When this is combined with [2.19], we obtain the following:

$$I \cong B(\nu_0, T) \int_{\nu_0 - \infty}^{\nu_0 + \infty} [1 - e^{-K(\nu)X}] d\nu \quad [2.21]$$

The specific blackbody function can be replaced by $B(\nu_0, T)$ here as the function can be assumed to remain the same for the relatively small width of a single line over which the integration is performed.

As the concentration of the element changes, there is a corresponding change in the integrated intensity of the emitted spectral line due to the change in the number density n_i of the species under analysis - put very simply, more atoms means more emission. The number density here refers to the number of the particular excited species with electrons populating the upper energy level of the observed transition and is contained in the optical density parameter, $K(\nu)X$. The number density is calculated by (after Kim, 1989):

$$n_i = \frac{n_0 g_a e^{-E_a/kT}}{Q} \quad [2.22]$$

where n_0 is the total number density of the species in the same ionisation state, g_a is the degeneracy of this lower energy state, E_a is the energy of the same level relative to the ground state of the species in the same state of ionisation and T is the plasma temperature. Q in equation 2.22 refers to the single particle canonical partition function, accounting for the range of degrees of freedom of an atomic species in a particular ionisation state. It is expressed as:

$$Q = \sum_S g_s e^{-E_s/kT} \quad [2.23]$$

and is summed over all permitted energy levels.

When large concentrations of an atomic species are present in a laser-produced plasma, the optical thickness of the plasma results in a non-linear increase in intensity with rising species concentration due to the larger density of available absorbers in the plasma, other than those at the edge of the plasma. However, at low concentrations (such as those studied in this body of work), the plasma is optically thin with regard to the studied element because of the consequential drop in density of absorbing atomic species. In the optically thin, low concentration case, equation 2.21 can be expanded such that:

$$I = \frac{h\nu_0 X A_{ba} g_a n_0 e^{-E_b/kT}}{Q} \quad [2.24]$$

In the above, A_{ba} is the radiative transition probability from an upper level b to a lower level a and g_b is the degeneracy of the *upper* level (b) of the transition. A diagram showing the relative constants and their relationship to energy levels is shown below

in Figure 5 (Lochte-Holtgreven, 1995). In this diagram, $n_b A_{ba}$ is the transition probability for spontaneous emission, $n_b u_\nu B_{ba}$ is the transition probability for stimulated emission and $n_a u_\nu B_{ab}$ is the absorption probability.

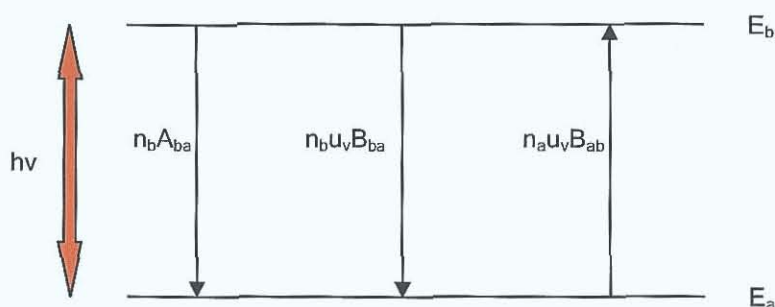


Figure 5: Transition Constants

If we take the number density n_0 of the species as relative to the concentration with the rest of the terms in [2.24] related to conditions in the laser plasma itself, then we can assume that the emission intensity of a spectral line at a certain wavelength is some function of the concentration of the studied species in the laser plasma - in other words:

$$I = f(C) \quad [2.25]$$

This function is known as the analytical calibration function - plots of this intensity versus the concentration of the element under study in the target material are known as analytical calibration curves and form the basis of experimental analytical spectroscopy.

This reliance on the emission from one particular line is sometimes shunned in favour of using 2 lines from a laser-produced plasma - one from the emitting species under study and one from the bulk material. This is the *internal referencing* method. Considerations such as the repeatability of the experiment due to slight changes in the conditions under which the plasma is formed have led to this approach being considered for LIPS applications, although improvements in equipment and analytical technique can largely negate this approach - the current approach favoured in the literature is still to use single emission lines in each quantitative study.

In the internal referencing scheme, the intensities of 2 lines are measured. In low-level detection where the purity of a bulk element is being assessed, the bulk element usually comprises most of the sample. In this case, the bulk element's

concentration can be said to be constant so that the low-level analyte's emission intensity changes linearly with respect to the bulk element's. Calibration curves are therefore constructed with the intensity ratio versus the analyte's concentration. This technique is valid according to the following equation, derived from [2.24] (after Kim, 1989):

$$\frac{I_1}{I_2} = \frac{[v_0 A_{ba} g_b]_1 Q_2 N_1}{[v_0 A_{ba} g_b]_2 Q_1 N_2} e^{-(E_1 - E_2)/kT} \quad [2.26]$$

In equation [2.26], I_1 is the intensity of the low concentration analyte and I_2 is the intensity of the bulk element. If the initial conditions are kept constant then the intensity of the emission from the bulk element should also remain constant - this means that, under the same initial conditions, targets with a variation in analyte concentration should produce different number densities in the upper energy level of the transition leading to a difference in emission intensity. If transitions with similar upper energy levels are chosen, the exponential part of the equation approaches zero, thus removing the ratio's dependence on the temperature of the plasma i.e. because the upper energy levels are at a similar energy, these energy levels are populated similarly with respect to one another. If the upper energy levels were spaced far apart, in a lower temperature plasma there could be a marked discrepancy in the population of these levels.

2.6 ANALYTICAL FIGURES OF MERIT

Two of the most important figures in analytical spectroscopy are the limits of detection and quantification. Both of these figures describe different concepts in terms of the analyte in the target and are derived from Gaussian statistics.

In the first case, the limit of detection (LOD) of an analyte is defined as being "the smallest measure that can be detected with reasonable certainty for a given analytical procedure" by the International Union of Pure and Applied Chemistry (IUPAC, 1978). The limit of quantification (LOQ) has a slightly different definition. "the limit of quantification refers to the smallest concentration or the mass which can be quantitatively analysed with reasonable reliability by a given procedure" (ACS Committee on Environmental Improvement, 1980). Both of these definitions rely on the statistical distribution of data points in a spectrum using the "normal" or Gaussian distribution

The Gaussian distribution is a function which gives the statistical likelihood of an event or data occurring within an interval defined using both the standard deviation (σ) of the data and the average (μ). It is given by the equation:

$$P(x; \mu, \sigma) = \frac{1}{\sigma\sqrt{2\pi}} e^{-(x-\mu)^2/2\sigma^2} \quad [2.27]$$

If the substitution $z = (x - \mu)/\sigma$ is used in equation [2.27], then the Gaussian distribution becomes:

$$\frac{1}{\sqrt{2\pi}} e^{-z^2/2} \quad [2.28]$$

This is known as the *unit Gaussian* or *unit normal* distribution. This equation generates a familiar looking “bell-shaped” curve, as seen below in Figure 6 (after Barlow, 1989).

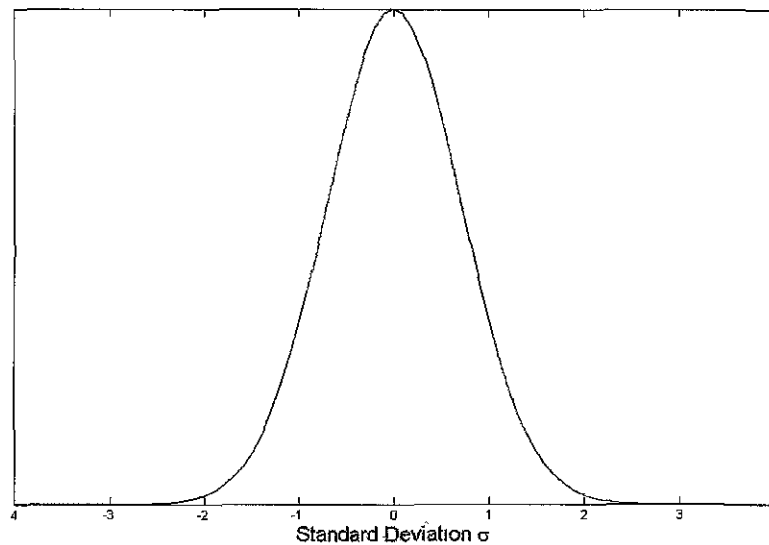


Figure 6: Gaussian Distribution

As plotted, this curve represents a probability distribution of data points with a mean value of 0. This distribution can be applied to statistical events and data in a wide variety of ways; the manner in which it applies to the LOD of a quantitative spectroscopic technique however concerns the integral of the distribution itself. The intervals on the x-axis of Figure 6 refer to multiples of the standard deviation of the distribution. When the curve is integrated using limits defined by the standard deviation from the mean and considering that

$$\int_{-\infty}^{\infty} P(x; \mu, \sigma) dx = 1 \quad [2.29]$$

i.e. that the integral of the distribution curve with $-\infty \leq \sigma \leq \infty$ is equal to 1 (when the integral is normalised to 1). This is an intuitive result, as the probability of any event occurring over an infinite range is 1. When the limits of the integral are changed to values of σ , the calculation of the area results in a fraction of the whole area. In other words, it gives the probability of an event lying within the limits of the integral. So, if an event occurs outside the limits of the integral, the probability of it occurring is $1 - P(-\sigma \leq x \leq \sigma)$. From this fact, if the mean and standard deviation are calculated from the background signal in a spectrum, the probability that a data point lies outside the normal distribution of data can be estimated, depending on the level of certainty required. For instance, if the point lies outside 2σ , then it would lie outside about 95% of data points within the set. Although there have been various different figures used in the literature, from $2\sqrt{2}$ (Boumans & Vrakking) to $3\sqrt{2}$ (Aziz, Broekaert & Leis, 1982) representing confidence intervals of between 99.74 and 99.99%; the confidence level set by IUPAC for the LOD of a particular analyte in a compound is 3σ , giving a confidence level of 99.87% that a point is not part of the background. That means that the LOD of an analyte is 3 times the standard deviation in the background signal, with the constant for the LOQ being 10

The LOD and LOQ can be obtained from a calibration curve relatively easily. In a calibration curve, the intensity or line ratio is plotted on the y-axis versus the concentration of analyte on the x-axis. It can then be said that (IUPAC, 1978)

$$L.O.D. = \frac{3\sigma_B}{S} \quad [2.30]$$

σ_B is the standard deviation in the background signal of the spectrum with the lowest concentration of analyte as plotted in the calibration curve, and S is the slope of the curve. This is justified by the assumption that, in a calibration curve with slope S , any x value (elemental concentration) can be obtained by dividing the intensity by the slope at a certain point ($y / (y/x) = x$). When the definition-stipulated value of 3σ is substituted for the intensity of the analytical line, the limit of detection is calculated.

2.7 SUMMARY

A basic description of the main processes involved in laser ablation of matter has been made. The most salient points regarding laser absorption by the target

material, laser plasma expansion and the processes involved in emission by atomic species in the laser plasma have been outlined and defined.

The *relationship* between atomic emission and quantitative Laser-Induced Plasma Spectroscopy has also been defined, with a description of how the emission intensity from the analyte's atomic species relate to the concentration of the analyte in the target and how the limit of both detection and quantification can be determined from these intensities.

REFERENCES

- ACS Committee on Environmental Improvement: "Guidelines for Data Acquisition and Data Quality Evaluation in Environmental Chemistry", *Analytical Chemistry*, **52**, pp. 2242 - 2249 (1980).
- Aziz A, Broekaert JAC & Leis F: "Analysis of Microamounts of Biological Samples by Evaporation in a Graphite Furnace and Inductively Coupled Plasma Atomic Emission Spectroscopy", *Spectrochimica Acta Part B*, **37**, pp. 369 - 379 (1982).
- Barlow RJ: *Statistics: A Guide to the Use of Statistical Methods in the Physical Sciences*, Wiley, 1989
- Brech F & Cross L: "Optical Microemission Stimulated by a Ruby Maser", **16**, no. 2, p. 59 (1962).
- Bekefi G. *Principles of Laser Plasmas*, Wiley-Interscience, 1976.
- Boumans PWJM & Vrakking JJAM: "Detection Limit Including Selectivity as a Criterion for Line Selection in Trace Analysis using Inductively Coupled Plasma-Atomic Emission Spectrometry (ICP-AES) - a Tutorial Treatment of a Fundamental Problem of AES", *Spectrochimica Acta Part B*, **42**, pp.819 - 840 (1987).
- Carroll PK & Kennedy ET: "Laser-Produced Plasmas", *Contemporary Physics*, **22**, no. 1, pp. 61 - 96 (1981).
- Chen FF: *Introduction to Plasma Physics and Controlled Fusion - Volume 1: Plasma Physics (Second Edition)*, Plenum, 1984
- Cremers DA & Radziemski LJ: *Laser-Induced Plasmas and Applications*, Dekker, 1989.
- Eliezer S: *The Interaction of High-Power Lasers with Plasmas*, Institute of Physics Publishing, 2002
- Hughes TP: *Plasmas and Laser Light*, Hilger, 1975.
- IUPAC, Analytical Chemistry Division: "Nomenclature, Symbols, Units and their Usage in Spectrochemical Analysis - II. Data Interpretation", *Spectrochimica Acta Part B*, **33**, pp. 241 - 245 (1978)
- Kennedy ET et al.: "XUV Absorption Spectroscopy with Laser-Produced Plasmas - A Review", *Physica Scripta*, **34**, pp 77 - 92 (1991)
- Kim YW: Chapter 8 of *Laser-Induced Plasmas and Applications*, Dekker, 1989.
- Lochte-Holtgreven W: *Plasma Diagnostics*, AIP Press, 1995.
- Moenke-Blankenberg L. *Laser Microanalysis*, Wiley, 1989.
- O' Sullivan G et al.: "Supercomplex Spectra and Continuum Emission from Rare-Earth Ions: Sm, A Case Study", *Journal of Physics B*, **32**, pp. 1893 - 1922 (1999).
- Ready JF: *Effects of High Power Laser Radiation*, Academic Press, 1971.
- Scott RH & Strasheim A: "Laser Produced Plasmas for Analytical Spectroscopy", *Spectrochimica Acta Part B*, **25**, pp. 311 - 332 (1970).

Vadillo JM & Laserna JJ: "Laser-Induced Plasma Spectrometry: Truly a Surface Analytical Tool", *Spectrochimica Acta Part B*, **59**, pp. 147 - 161 (2004).

CHAPTER III: EQUIPMENT AND LABORATORY SYSTEMS

This chapter serves as a basic description of the various different pieces of experimental equipment used during the course of the project. These systems can be broken down into plasma generation, light emission and detection.

3.1 OVERVIEW

LIPS experiments tend to be simple experiments consisting of as few pieces of equipment as possible. In comparison to other spectroscopic techniques such as ICP-AES (Inductively Coupled Plasma Atomic Emission Spectroscopy) and ETA-AAS (Electrothermal Atomisation Atomic Absorption Spectroscopy), the complexity of both the excitation and detection processes are very much reduced (Winefordner et al., 2004). The basic components of all LIPS experiments are a pulsed laser, focusing optics, a spectrometer/detector combination and a device to synchronise the laser and detector. Although additional components may be required in some experiments, configurations are mostly consistent with the main variable parameters being the spectral range and response and both temporal & spectral resolution.

In the VUV part of the spectrum, the configuration is a little more complex due to the nature of the radiation under investigation. Since air is a VUV absorber, experiments must be performed in either partial or near total vacuum conditions. This means that the target, spectrometer and detector must be held under vacuum conditions. As gases are sometimes used to buffer laser plasma expansion, partial pressures must be generated separately from the spectrometer. However, despite these differences, the basic set-up remains the same. Figure 1 shows a basic diagram of the whole system used in the course of the research reported here.

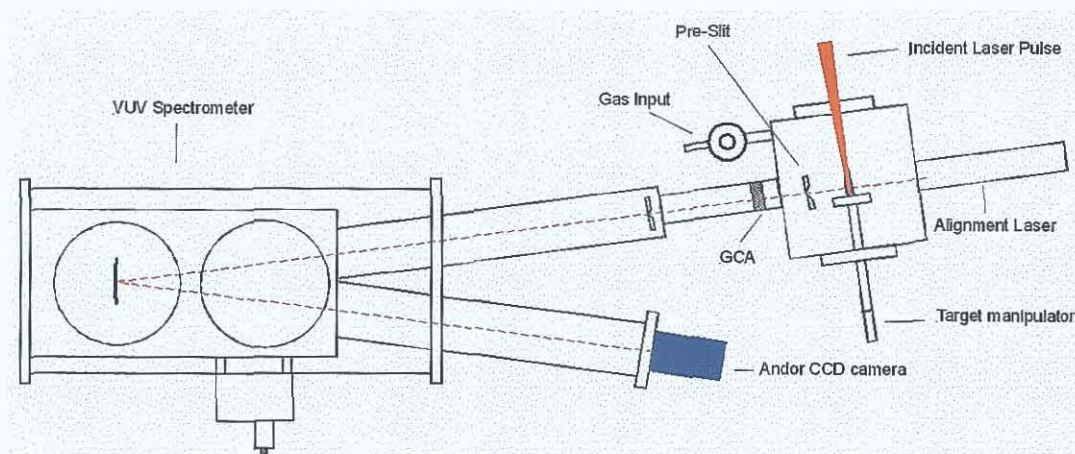


Figure 1: Experimental System Overview

As can be seen, the system consists of generation, dispersion and detection components i.e. the laser pulse & target chamber, the spectrometer & grating and the CCD camera respectively. A description of major components and their methods of operation and synchronisation are given in the following sections.

3.2 LASER SYSTEM - CONTINUUM SURELITE III-10

The laser used to create the steel plasmas was a Continuum Surelite model III-10. This laser, at its optimum output, is capable of producing an 820 mJ pulse of energy at a wavelength of 1064 nm (the Nd:YAG fundamental wavelength) in 6 ns. The variation in pulse energy is typically < 1%, making this instrument ideal for laser plasma experiments where repeatable results are necessary. Figure 2 shows a diagram of the internal configuration of the Surelite III-10, along with the temporal profile of the beam, as observed using a photodiode and oscilloscope.

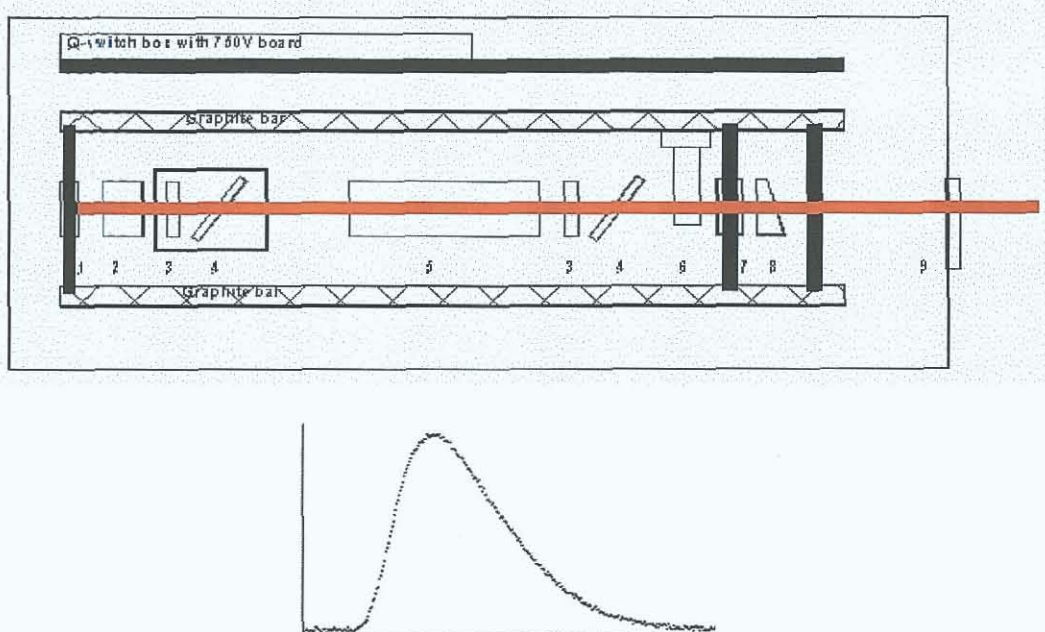


Figure 2: Surelite III-10 Laser and Pulse Temporal Profile

The labelled parts are as follows:

1. Rear mirror, 100% reflectance
2. Pockels cell
3. $\lambda/4$ plate
4. Dielectric polariser
5. Laser head - 2 flashlamps, Nd:YAG rod, cooling system
6. Intra-cavity shutter
7. Gaussian mirror
8. Output beam compensator

9. Exit port shutter

The laser itself has a fixed internal pulse frequency of 10 Hz, although minor variations in this rate must be used while the laser is in external triggering mode; in “normal” operation the laser is pulsed at about 9.8 Hz.

Figure 3 shows the variation in the output pulse energy when the flashlamp voltage and Q-switch timing are changed. All measurements were made with a Coherent FieldMax-TO power meter and a Coherent PM10V1 thermopile sensor.

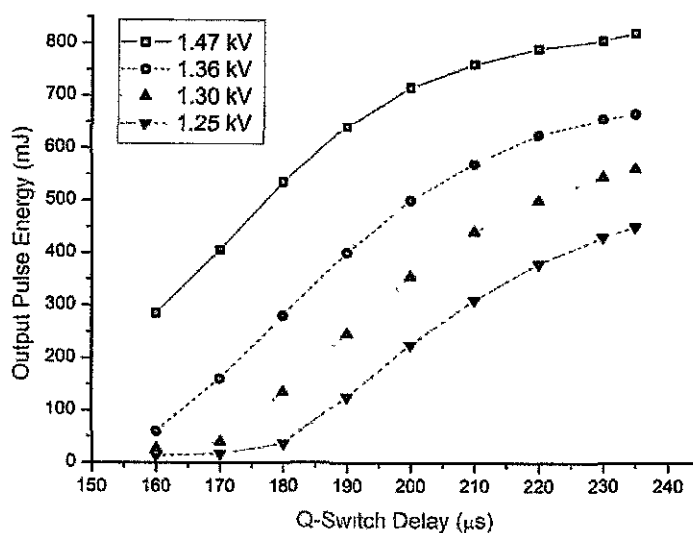


Figure 3: Laser Pulse Energy Variation

While modifying the Q-switch timing is an effective method of varying the pulse energy, it is generally not recommended by the manufacturer as it can have a detrimental effect on the beam quality which, in normal operation, is claimed to be 95% Gaussian. At the optimum Q-switch timing of 235 μs, the pulse has good shot-to-shot uniformity and repeatability (>99%). However, when the Q-switch timing is modified, the manufacturers claim that the beam profile destabilises significantly. With this in mind, the flashlamp voltage was altered to achieve the desired pulse energy. This has the effect of maintaining the Gaussian profile of the laser pulse but reducing the number of photons produced in each laser pulse, thus lowering the power.

The actual laser pulse is produced in the Surelite in the following manner. The laser rod is a Yttrium Aluminium Garnet crystal, $Y_2Al_5O_{12}$, doped with about between 0.9 and 1.4% of Nd^{3+} ions. It measures 115 mm long and has a diameter of 9 mm

with both ends coated in hard anti-reflection coatings. The laser head incorporates the rod and a pair of linear flashlamps (Xenon gas at between 1 and 3 atmospheres) surrounded by a high brilliance magnesium oxide diffuser, resulting in high pumping efficiency in the rod. This has the effect of minimising thermal loading and reducing power consumption by the laser, creating good pumping homogeneity and concomitantly high gain, high quality beams. The entire assembly is cooled with an onboard reservoir of distilled, deionised water.

The flashlamps discharge in 200 μ s producing an intense white light pulse. This light is absorbed by the crystal and population inversion is achieved. A Pockels Cell creates the actual output pulse as follows. As the radiation travels through the laser cavity (defined by the mirrors at either end), they pass through the assembly to the left of Figure 2, the parts marked 1 to 4. The pulse emerges from the rod unpolarised, until it reaches the dielectric polariser which is at an angle of 57° to the optical axis of the laser. This transmits horizontally polarised light to a $1/4$ wave plate which circularly polarises the radiation. With the Pockels cell in the "off" state (uncharged, 0V), there is no change in polarisation as the light passes through, leaving the pulse polarization in the same orientation as it entered. The light reflects from the mirror at the back, again entering the Pockels cell and going straight through to the $1/4$ wave plate, which changes the polarization to vertical. On meeting the dielectric polariser for the second time, the pulse is rejected and not allowed to re-enter the rod as the orientation of the polariser is horizontal. The total change in polarisation when leaving and meeting the dielectric polariser is, therefore, 90° . Figure 4 below shows a visual representation of the process.

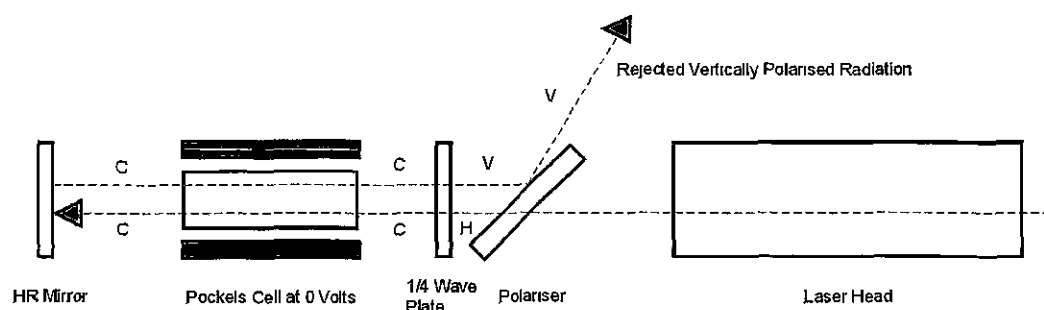


Figure 4 Laser Operation - Pockels Cell "Off"

In the above diagram, H stands for horizontally polarised, C for circularly polarised and V for vertically polarised.

With the Pockels Cell in the "on" state (charged, 3.6 kV), a different process occurs. The same process is repeated until the pulse enters the Pockels Cell for the

first time. The Pockels Cell is a KD*P crystal which, when charged to a voltage of 3.6 kV, acts like a $\frac{1}{4}$ wave plate. When the pulse is incident on the cell, it causes a phase lag of 90° , resulting in circularly polarised radiation. The pulse is reflected from the mirror and a further 90° phase lag is *again* caused by the cell, leaving the pulse circularly polarised but 180° out of phase with its initial state entering the Pockels Cell. The $\frac{1}{4}$ wave plate horizontally polarises the light again, albeit 180° out of phase to its emergence from the dielectric polariser. With the radiation in this state of polarisation it passes freely through the dielectric polariser and enters the rod, producing a high energy pulse emitted from the laser (see Figure 5 below).

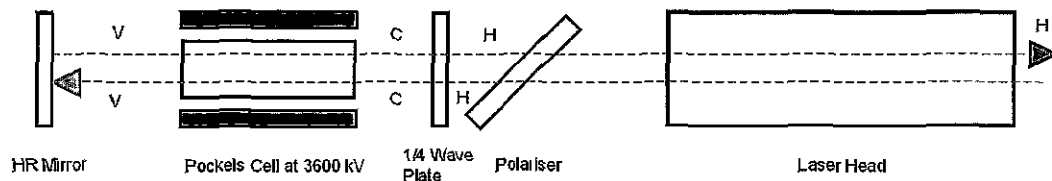


Figure 5 Laser Operation - Pockels Cell "On"

3.2.1 LASER STEERING AND FOCUSING

The laser pulse was focussed onto the surface of the target using both cylindrical and spherical plano-convex lenses. All lenses were mounted using holders that were adjustable in 3 dimensions to ensure precise focusing on the target. The lens material was BK7, which has a high transmission at 1064 nm, the fundamental Nd:YAG frequency and were anti-reflection coated. The smallest size spot a high quality Gaussian laser pulse can be focussed into is determined by 2 separate factors - spherical aberrations due to the optical system and the diffraction limit of the lens itself. The smallest spot diameter allowing for spherical aberration of the optical system is given by (Moenke-Blankenberg, 1989):

$$d_{\text{aber}} = f \left(\frac{d}{f} \right)^3 \frac{\left[n^2 - (2n+1)k + (n+2) \frac{k^2}{n} \right]}{32(n-1)^2} \quad [3.1]$$

where d is the input laser beam diameter, n is the refractive index of the lens material and f is the focal length. The constant k is related to the radii of curvature of the lens by:

$$k = \frac{R_2}{(R_2 - R_1)} \quad [3.2]$$

With light incident on the plane side of a plano-convex lens $k = 0$ while if the beam is incident on the convex side (as in all the LIPS experiments conducted in this work), $k = 1$. This means that using a 100 mm spherical plano-convex lens made from BK7 ($n = 1.50669$ @ 1060 nm - Melles Griot, 2004) and a beam of diameter 9 mm, a minimum spot size of 5.2 μm is achievable.

If a diffraction-limited system is used then the diffraction-limited diameter d_{diff} is calculated using (Hecht, 1998):

$$d_{diff} = \frac{2.44\lambda f}{d} \quad [3.3]$$

The minimum calculated spot size possible using this focussing scheme is 28.8 μm - more than 4 times larger than the size obtained using the spherical aberration limitation scheme. This means that the system is predominantly diffraction limited and that the minimum spot size achievable with the laser beam under ideal focussing conditions is of the order of 30 μm .

3.3 TARGET CHAMBER & TARGETS

The target chamber used as part of the experimental system was a simple aluminium block with a partially hollowed interior. While the block is cubic with sides of 12.5 cm, the interior has been hollowed by simply drilling cylindrical holes through the block. Each hole has been drilled from face to opposite face, the radius of each cylinder is 3.5 cm. This makes for a total internal volume of about 0.75 l. All sides were polished to accommodate standard o-ring flanges, which require rubber o-rings to form a vacuum tight physical seal between outside fittings such as windows and connectors and the chamber itself. A photo of the chamber is shown in Figure 6.

The laser pulse entered the target chamber via an interchangeable window on the front of the cube. Since the debris produced by the laser plasma expands perpendicularly to the target surface and the target surface was parallel to the window, the inside of the window was subjected to the frequent build-up of ejecta from the target. It was necessary to clean or replace the windows regularly i.e. when a stage was reached where it was difficult to see the target through the window, as deposition on the window from the target blocked the view to the target - the laser itself kept its own pathway through the glass relatively clear.

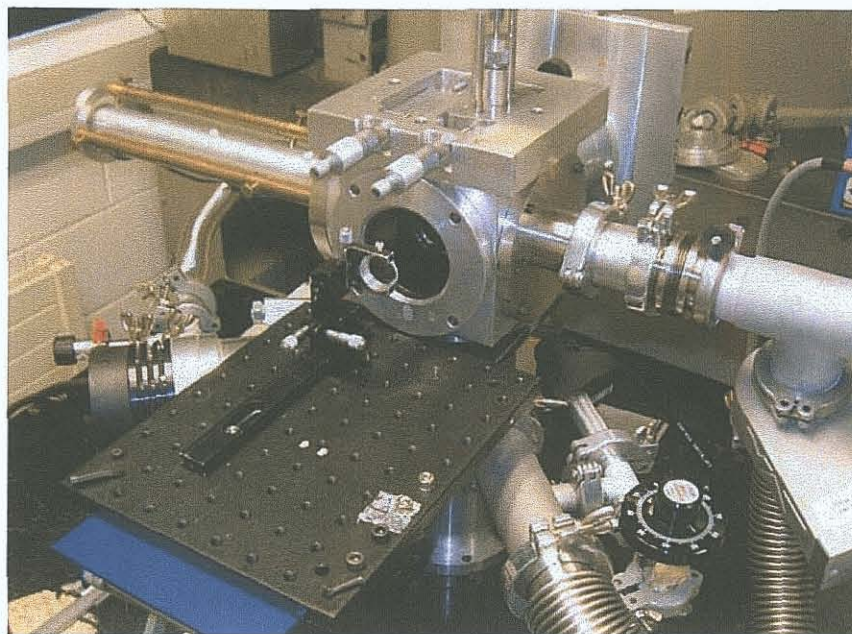


Figure 6: Target Chamber

In order to optically align the system with the spectrometer and CCD camera, a helium neon laser was attached to one side of the chamber. This was mounted inside a 2-dimensional translation stage and adjusted when the entire system was vented i.e. not in vacuum so the laser beam passed straight through the entrance slit of the spectrometer, illuminated the centre of the grating and was reflected onto the centre of the "exit" arm of the spectrometer when the grating was set to the zero order position. It was also important to align the Glass Capillary Array (GCA, as described in Section 3.3.2) with the optical axis. This was done by placing the GCA in its holder in the optical axis, shining the laser through it and ensuring the characteristic "speckle" pattern was centred on the spectrometer entrance slit. After doing this, the target surface could be easily aligned with the optical axis of the experiment by moving the surface until the edge of the He-Ne laser beam was blocked by the target.

The targets themselves were mounted on an externally controlled XYZ stage, shown in Figure 7. The target was screwed onto a post, which was coupled to a micrometer outside the chamber. The post itself went through a pair of aluminium plates that could be adjusted by separate micrometers on the X and Y axes, giving 3 dimensional control of the target in the chamber.

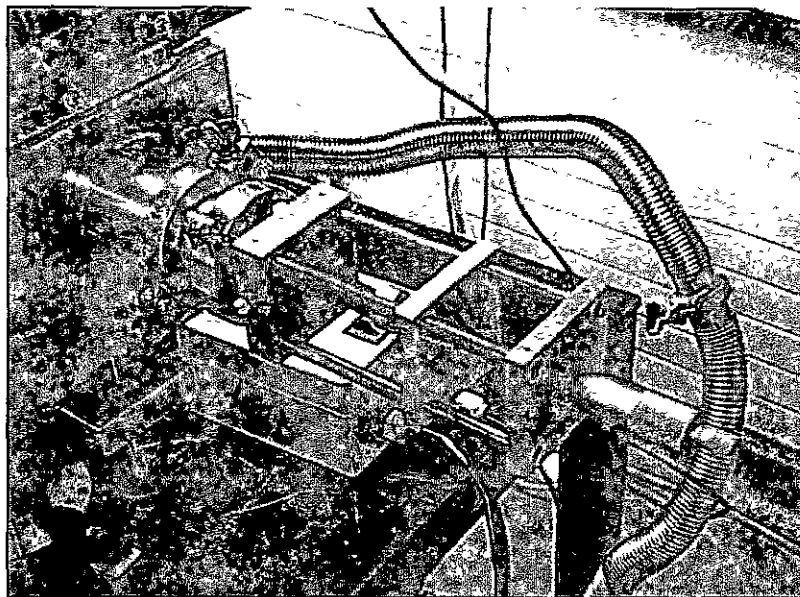


Figure 7 Target Manipulator

The Z stage was the most important in the experiment, as this stage permitted movement of the target into and out of the optical axis. Using this property and the pre-slit described later in this chapter, spatial segments of the plasma could be selected to a good degree of accuracy. As the target was moved in the Z axis, the lens holder was used to refocus the laser beam onto the target surface by the same distance so that identical conditions could be studied for variations in distance from the target surface. Since the targets themselves were cylindrical in shape, a fresh surface could be exposed by rotating the post.

The targets used in this work were critical for both the validity and repeatability of the experiments performed. A wide range of targets with varying analyte concentrations were purchased from Glen Spectra Reference Materials™ - a more complete description of their content is available in Appendix B Targets. For initial studies, a single sample with a high concentration of the analyte was chosen and placed in the target chamber. When optimum conditions were extrapolated from studies on the single high concentration target, samples with varying concentrations of analyte were machined and placed into a carousel which had space for up to 6 targets, shown in Figure 8



Figure 8: Target Carousel

In this way, multiple samples could be studied whilst maintaining both atmospheric and spatial conditions. One of the advantages of LIPS is that targets require very little preparation for study - this was achieved in vacuum conditions in the chamber by firing unfocused laser shots onto the target surface to remove any surface contaminants like dirt or, because some of the targets were binary samples (samples containing just 2 elements), rust. In addition to these precautions, the target surface was rotated in order to expose a fresh surface after every train of shots - this reduced possible effects of cratering on the target surface.

3.3.1 PRE-SLIT

One of the main differences between this series of studies and those performed by other research groups is the use of a pre-slit to shield continuum radiation near the target surface from the detector. Generally, this is done temporally, but a pre-slit allows temporal integration over long periods relative to the lifetime of the laser plasma whilst adding the ability to select different spatial regions in the plasma where varying conditions may be investigated.

The pre-slit used in the experiments described in chapters 4 & 5 was simply an adjustable slit mounted in the target chamber approximately 30 mm from the plasma source. It had a set width of 250 μm , meaning that radiation from a "slice" of plasma roughly the same width as that of the pre-slit was unimpeded in its passage towards the spectrometer. The pre-slit was fixed on the optical axis, with its alignment

performed after the major alignment of the He/Ne laser to the spectrometer's entrance and exit slits.

3.3.2 GLASS CAPILLARY ARRAYS

Glass Capillary Arrays (GCAs) are devices that allow pressure differences to exist between 2 separate parts of a vacuum system while leaving the aperture between these 2 areas mostly transparent to light. A GCA is basically a glass plate with very fine holes bored in it - these are capable of maintaining up to 3 orders of magnitude pressure differences between sides, depending on the individual capillary diameters and the thickness of the array itself. A microscope image of a GCA is shown in Figure 9 below, taken from the Burle Industries Inc. website. The GCA shown has a pore diameter of 5 μm .

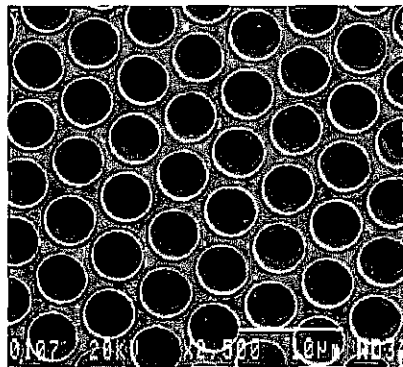


Figure 9. Microscope Image of a Typical GCA, © Burle Industries Inc.

The Collimated Holes Inc. GCAs used in the experiments were 25 mm in diameter, 3 mm thick and had a pore diameter of 50 μm . Made from lead-alkali silicate, they weren't transparent to VUV radiation but information from the manufacturer stated that they had a 50% open area i.e. 50% of normally incident radiation is transmitted. As will be explained later on in section 3.4.4, the spectrometer's entrance slit was large compared to the radiation wavelength and, as such, dispersion across the entire grating was impossible. Light from the plasma itself is radiated in all directions though, so the maximum acceptance angle of the GCA (i.e. the largest angle light from the plasma could go through the GCA at) became important. This can be calculated from the simple formula:

$$\theta = \text{Tan}^{-1}\left(\frac{D}{l}\right) \quad [3.4]$$

If we take D to be the pore diameter (50 μm) and l to be the thickness of the GCA (3 mm), we end up with an acceptance angle of just under 1° or about 17 mrad.

3.4 1 M ARC VM-521 VUV SPECTROMETER/CONCAVE GRATING

The spectrometer used was a 1 m normal incidence Acton Research Corporation VM-521 using a 1200 grooves/mm Bausch and Lomb Al+MgF₂ coated holographically-ruled diffraction grating. The stated spectral range of the spectrometer is from 30 to 325 nm but in actuality this is reduced by the efficiency of the grating and detector at higher wavelengths. The lower limit is considered to be the transition wavelength between VUV and EUV/XUV radiation, as grazing incidence spectrometers must be used due to poor reflectivity of normal and near normal incidence devices below this.



Figure 10: ARC VM-521 Spectrometer

The Al/MgF₂ coating on the grating means that there is enhanced reflection efficiency at VUV wavelengths. The spectrometer uses an off-Rowland circle mount for the diffraction grating. This means that, if an image is in focus on the entrance slit of the spectrometer, it will be in focus on the exit slit. How this works is explained in more detail below, the theory therein is taken substantially from Samson (1967) with subsequent, more specific elucidation by Doyle (1995) and Meighan (2000).

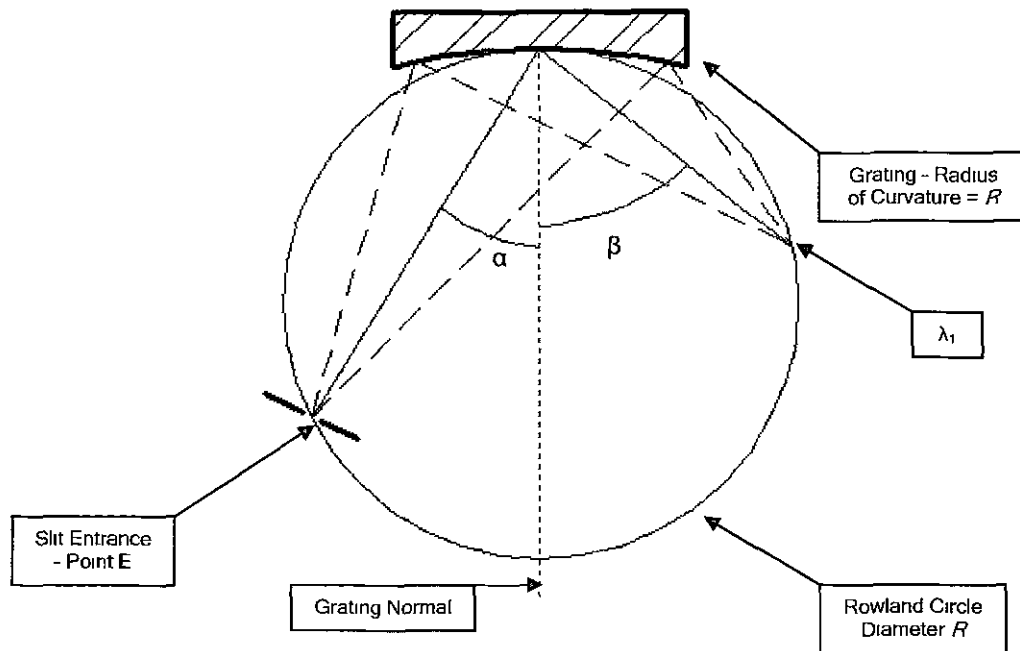


Figure 11 Rowland Circle

The Rowland circle, as shown in Figure 11, is the name given to a spectrometer/grating combination that bases its operation on having a concave grating with radius of curvature R with entrance and exit slits located on an extrapolated circle of radius $R/2$. This not only gives the dispersion properties of a plane diffraction grating, but also adds the focusing qualities of a concave mirror

The grating is placed in the spectrometer as in Figure 12 so that both the entrance slit and CCD camera face lie on the Rowland circle when the grating is at the zero order i.e. both the incident and reflected/dispersed radiation occur at an angle of 75° to the grating normal in the case of the diffraction grating currently in use

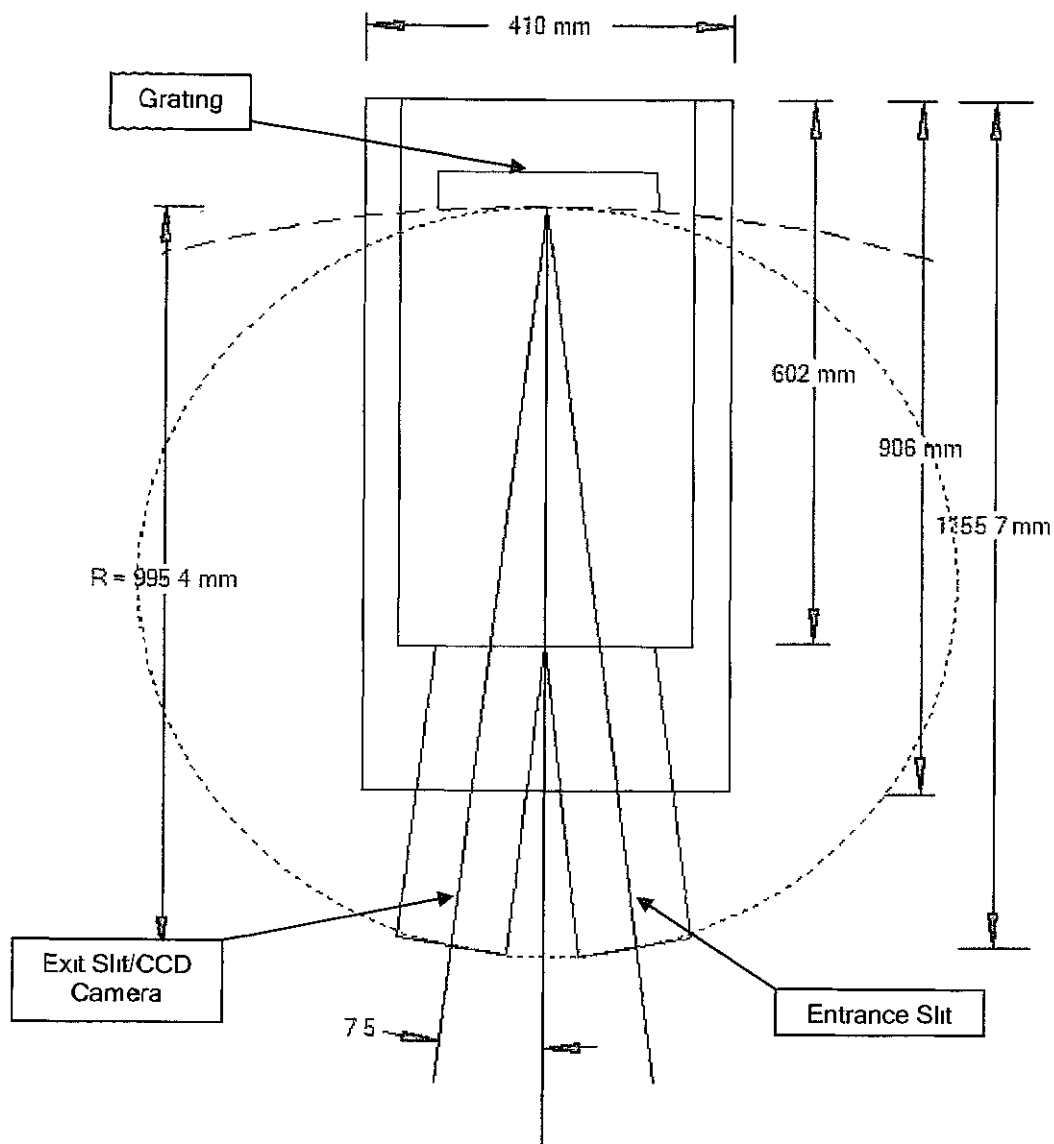


Figure 12 ARC VM 521 VUV Spectrometer Schematic

3.4.1 GENERAL THEORY OF THE CONCAVE DIFFRACTION GRATING

We start by imagining a concave grating in a Cartesian co-ordinate system. If the centre of the grating lies at point O , the x and z axes lie perpendicular and parallel to the grating respectively, as shown in Figure 13 below. Consider an object light source A on the entrance slit with the corresponding image formed at B , the image plane, and a point P being any arbitrary point on the grating itself. In order for 2 light rays to constructively interfere and produce an image at point B , the path length between them must be an integer number of wavelengths i.e. $m\lambda$ where m is the spectral order of the radiation. When we consider reflection from 2 adjacent grooves ("lines") on a ruled diffraction grating a distance w apart, we can surmise that the path

difference between the 2 rays is now $m\lambda w/d$ where d is the inter-groove spacing, the number of lines per mm of grating using S.I. units.

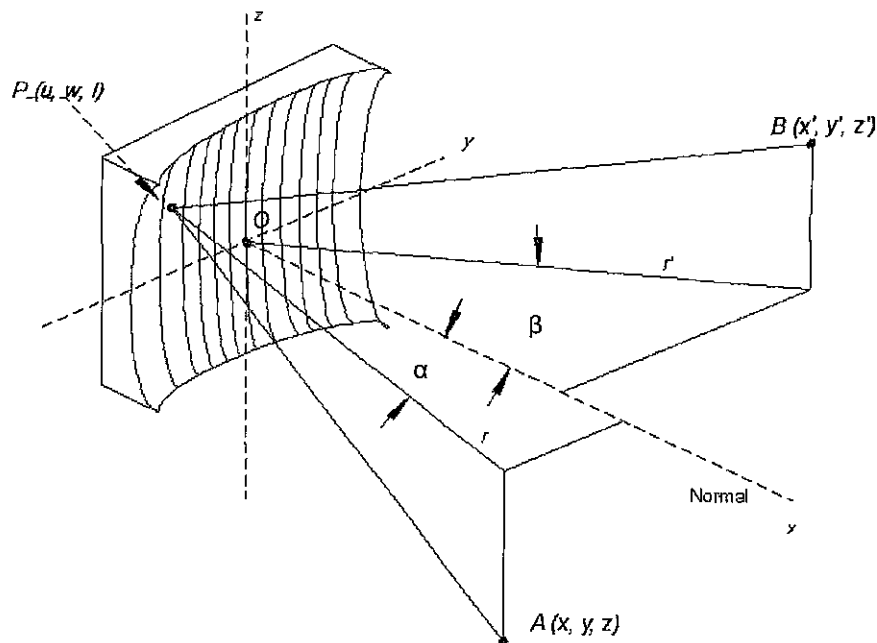


Figure 13 Image Formation Schematic (after Samson)

In order to focus light from A onto B from any point P on the diffraction grating, the path length taken by the light rays must satisfy the equation

$$F = AP + BP + \left(\frac{wm\lambda}{d} \right) \quad [3.5]$$

In equation [3.5],

$$(AP)^2 = (x-u)^2 + (y-w)^2 + (z-l)^2 \quad [3.6]$$

$$(BP)^2 = (x'-u)^2 + (y'-w)^2 + (z'-l)^2 \quad [3.7]$$

F is called the *Optical Path Function* and represents the discrete lengths light must travel in order to be focused onto B for any intermediate point P on the diffraction grating.

Both [3.6] and [3.7] can be rewritten using cylindrical co-ordinates, using $x = r \cos \alpha$, $y = r \sin \alpha$, $x' = r' \cos \beta$ and $y' = r' \sin \beta$. Fermat's principle of least time can be used to state that point B is located in such a way that the path function F will be an extreme for any point P . In the case of a fixed entry/exit vacuum spectrometer, A and B are fixed and P can be any point on the surface of the diffraction grating. This leads us to the conclusion that for F to be an extreme,

$$\begin{aligned}\frac{\partial F}{\partial l} &= 0 \\ \frac{\partial F}{\partial w} &= 0\end{aligned}\quad [3.8]$$

In the ideal case, both expressions in [3.8] could be satisfied simultaneously to obtain a perfect focus at a point B . This is, unfortunately, impossible using a concave grating. In practice, there are 2 focal points in the system: a horizontal or "primary" focal point where light is focused vertically i.e. into tight lines and a vertical or "secondary" focus where light is focused onto a horizontal plane. The first case is desirable for spectroscopic systems as the maximum resolution of spectral lines can be achieved with a tight horizontal focus

To get the best primary focal point for B , the following condition must be satisfied:

$$\frac{\cos^2 \alpha}{r} + \frac{\cos^2 \beta}{r'} = \frac{\cos \alpha + \cos \beta}{R} \quad [3.9]$$

where R is the radius of curvature of the diffraction grating.

The vertical focus is important when considering the astigmatism (i.e. how well focused the spectrum is at the exit of the spectrometer) of the spectroscopic system and is expressed by

$$\frac{1}{r'} = \frac{\cos \alpha + \cos \beta}{R} - \frac{1}{r} \quad [3.10]$$

Using Fermat's principle of least time again, it can be shown that for the central ray with path AOB ,

$$\left(1 + \frac{z^2}{r^2}\right)^{\frac{1}{2}} (\sin \alpha + \sin \beta) = \frac{m\lambda}{d} \quad [3.11]$$

Realistically, (z^2/r^2) tends to 0 for real systems as the ratio of the image height (z) to the distance it travels to the grating surface (r) is small, in the case of the VM-521 spectrometer, (z^2/r^2) reaches a maximum of 2.5×10^{-5} when the entrance slit is fully illuminated as the full height of the entrance slit is 10 mm while r is 995.4 mm. Applying this to [3.8], we end up with the familiar grating equation:

$$\pm m\lambda = d(\sin \alpha \pm \sin \beta) \quad [3.12]$$

The \pm is present because of the presence of both "inside" and "outside" orders of dispersed light - the outside order (negative) is where the spectrum lies between the central image ($\alpha = \beta$) and the grating tangent, the inside order is where the spectrum lies between the central image and the grating normal. The VM-521 spectrometer uses the spectrum on the inside order, so only the positive case of [3.9]

is needed to describe the dispersion characteristics of the spectrometer/grating set-up i.e. the following grating equation is used:

$$m\lambda = d(\sin \alpha - \sin \beta) \quad [3.13]$$

since α and β lie on opposite sides of the grating normal.

3.4.2 DISPERSION

Dispersion refers to the way different wavelengths are distributed across the Rowland circle - the most commonly used phrase, angular dispersion, refers to the grating's ability to disperse radiation of different wavelengths per unit angle, $\partial\beta/\partial\lambda$. This can be determined (assuming a fixed angle of incidence) by differentiating [3.13]:

$$\frac{\partial\beta}{\partial\lambda} = \frac{m}{d \cos \beta} \quad [3.14]$$

A more useful property of the grating to know is the *Reciprocal Linear Dispersion*, $d\lambda/dl$, which gives us the degree to which radiation is dispersed along the Rowland circle. The linear dispersion of the system can be re-expressed to include $\Delta\beta$ in the following manner

$$\frac{\Delta\lambda}{\Delta l} = \frac{\Delta\lambda}{\Delta\beta} \times \frac{\Delta\beta}{\Delta l} \quad [3.15]$$

If $R\Delta\beta = \Delta l$, then [3.15] becomes

$$\frac{\Delta\lambda}{\Delta l} = \frac{1}{R \left(\frac{\Delta\beta}{\Delta\lambda} \right)} \quad [3.16]$$

From [3.14] we then have the expression for the *Plate Factor*

$$\frac{d\lambda}{dl} = \frac{d \cos \beta}{mR} = \frac{1}{d} \left(\frac{\cos \beta}{mR} \right) \times 10^3 \text{ nm/mm} \quad [3.17]$$

where $1/d$ is the number of ruled lines per millimetre on the grating and R is the radius of curvature of the Rowland circle measured in metres. As such, these expressions are not entirely suitable for a complete description of the spectrometric system as they assume a fixed angle of incidence. That would require that the exit arm be rotatable about the Rowland circle which is an impractical solution for most laboratory applications. Luckily, an *Off-Rowland Mount* may be used to compensate for this shortcoming.

3.4.3 OFF-ROWLAND MOUNT & SPECTRAL CHARACTERISTICS

The off-Rowland mounting system for a concave grating is based on moving the grating on a fixed path through an angle θ to the grating normal. When the grating is unrotated, the angles of incidence and reflection are the same i.e. $\alpha = \beta$, $\theta = 0$ and the centre of the Rowland circle remains on the bisector of the entrance arms. However, when the grating is rotated so that a portion of the inside spectrum appears on the exit slit/detector, the grating and concomitantly the Rowland circle undergo a rotation & displacement through some angle θ & distance x respectively as can be seen in Figure 14 below.

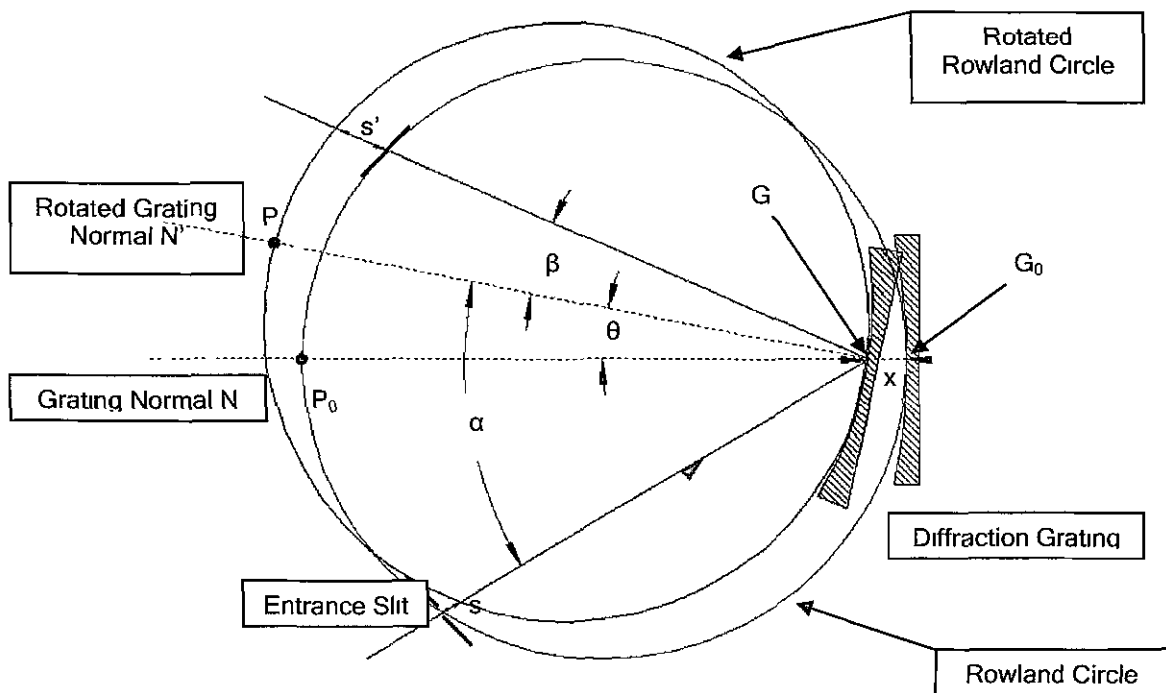


Figure 14 Spectrometer in Normal Incidence and Near Normal Incidence Configurations

In Figure 14 we can see that the entrance slit and exit slit/detector have undergone translations through distances designated s and s' respectively with the grating being moved a distance x along the grating normal. We can construct from the above diagram that

$$R \cos \alpha + s = R \cos \beta - s' \quad [3.18]$$

where R is the radius of curvature of the grating. Letting α_0 be the angle subtended by the entrance arm at $\theta = 0$ (7.5°), we can say that if the angular change in α over the observed wavelength range is small and we assume $s = s'$ that

$$s = R \sin \alpha_0 \sin \theta \quad [3.19]$$

Using Figure 14, we see that

$$R = x + GP_0 \quad [3.20]$$

Since

$$GP_0 \cong R \cos \theta \quad [3.21]$$

we see that the linear movement x along the bisector of the spectrometer's entrance and exit arms can be written as

$$x = R(1 - \cos \theta) \quad [3.22]$$

The literature accompanying the spectrometer states that for the device's operating range of 30 - 325 nm, the grating will rotate from 0° to 20° . Therefore, the total linear translation of the grating along the grating normal N (from Figure 14) using equation [3.22] will be from 0 to 60 mm.

The grating currently used in the VM-521 spectrometer is blazed for 80 nm radiation in the first order. This term refers to the amount of incident radiation on the grating of a certain wavelength dispersed in first order i.e. the grating works most efficiently at reflecting light at 80 nm.

3.4.4 RESOLUTION

Spectral features are said to be barely resolvable if the maximum point of one line falls at the minimum of another (Smith & King, 2000) i.e. 2 lines can be resolved if the "saddle point" (i.e. the depression between two spectral peaks that are close together) between them is $8/\pi^2$ (about 81%) of the maximum line intensity, as explained more thoroughly in Hecht (1998).

Modifications to this criterion have been made by Namioka (1959) implying that the correlation between spectral maximum and minimum are unnecessary; the $8/\pi^2$ parameter is still required however. The theoretical limit to the resolving power of an instrument is given by

$$\Delta\beta = \frac{\lambda}{Nd \cos \beta} \quad [3.23]$$

The resolving power \mathfrak{R} is defined as $\Delta\lambda / \lambda$. If $\Delta\lambda$ is expressed in terms of $\Delta\beta$, we see that

$$\Delta\lambda = \Delta\beta \cdot \frac{d\lambda}{d\beta} \quad [3.24]$$

Using [3.14] and [3.23], we redefine the above as

$$\Delta\lambda = \frac{\lambda}{mN} \quad [3.25]$$

So

$$\mathfrak{R} = \frac{\lambda}{\Delta\lambda} = mN \quad [3.26]$$

where m is the order of the radiation and N is the number of illuminated grooves. An alternative form used primarily by Namioka (1959) states that

$$\mathfrak{R} = \frac{Wm}{d} \quad [3.27]$$

In this case, W is the width of the grating exposed to radiation.

The resolution of the instrument at a specific wavelength is optimised for discrete illuminated widths of the grating, W_{OPT} . On analysis of the optical path function, Namioka (1961) calculated this width to be

$$W_{OPT} = 2.38 \left[R^3 \lambda \frac{\cos \alpha \cos \beta}{(\sin^2 \alpha \cos \beta + \sin^2 \beta \cos \alpha)} \right]^{\frac{1}{4}} \quad [3.28]$$

where R is the radius of curvature of the diffraction grating, α is the angle of incidence on the grating and β is the angle of diffraction. From [3.24], we can see that W_{OPT} changes for varying wavelengths. Mack, Stehn and Edlén have showed that when W is less than or equal to $0.85(W_{OPT})$, then the resolving power \mathfrak{R} is as [3.26] and [3.27].

The actual illuminated width of the diffraction grating in the experiments conducted and reported in chapters 4 & 5 is significantly lower than W_{OPT} . Considering the GCA and spectrometer entrance slit alone, the GCA has an acceptance angle of 17 mrad (section 3.3.2), the maximum illuminated grating width is about 33 mm, slightly more than a third of the grating's 96 mm width. A maximum theoretical resolving power \mathfrak{R} is then calculated to be about 40,000. In practice, this figure is far lower due to imperfections on the grating surface, the width of the entrance slit and most importantly in this case, the pixel size of the CCD camera on the exit arm of the spectrometer. Information on the spectrometer provided by the manufacturer states that for the current grating, the resolving power of the spectrometer at the blaze wavelength of 80 nm and for an entrance slit width of 10 μm is 5,700.

The instrumental width of an optical component is the degree to which discrete lines are broadened over a spectral range by components of an optical system, as opposed to broadening by processes associated with the plasma itself. Using equation [3.17], the grating plate factor, we can derive an expression for the

grating dispersion for varying angles of incidence to the grating. From Figure 14, we see that since both entrance and exit arms of the spectrometer are at 7.5° to the normal, we can assume that at a different angle of incidence i.e. when the grating has been rotated in order to disperse a different wavelength range onto the exit, $\alpha = 7.5 + \theta$ and $\beta = 7.5 - \theta$, where θ is the angle through which the grating has been rotated. The grating equation is now rewritten as

$$m\lambda = d(\sin 7.5 \cos \theta + \cos 7.5 \sin \theta - \sin 7.5 \cos \theta + \cos 7.5 \sin \theta) \quad [3.29]$$

which reduces to

$$m\lambda = 2d(\cos 7.5 \sin \theta) \quad [3.30]$$

The linear dispersion is redefined in terms of $\delta\theta$ so that

$$\frac{\delta\lambda}{\delta l} = \frac{\delta\lambda}{\delta\theta} \cdot \frac{\delta\theta}{\delta l} \quad [3.31]$$

where

$$\frac{\delta\lambda}{\delta\theta} = \frac{2d \cos 7.5 \cos \theta}{m} \quad [3.32]$$

and

$$\frac{\delta\theta}{\delta l} = \frac{\delta\theta}{\delta\beta} \cdot \frac{\delta\beta}{\delta l} = \frac{1}{2} \cdot \frac{\delta\beta}{\delta l} = \frac{1}{2R} \quad [3.33]$$

The reciprocal linear dispersion of the grating as a function of grating angle is now written in its final form as being

$$\frac{\delta\lambda_\theta}{\delta l} = \frac{d \cos 7.5 \cos \theta}{mR} \quad [3.34]$$

At the blaze wavelength of 80 nm where the grating is at an angle of 2.75° to the grating normal, the dispersion is calculated to be about 0.829 nm/mm, which agrees well with the manufacturer's stated dispersion of 0.83 nm/mm

We can now estimate the actual resolving power of the system. Namioka (1961) has defined $\Delta\lambda$ as

$$\Delta\lambda = \frac{W_s d}{R} \quad [3.35]$$

For a standard slit width of $50 \mu\text{m}$, the corresponding instrumental width of the grating/spectrometer is 0.042 nm.

Since the Andor CCD camera (chapter 3.5) is 26.6 mm wide and has 1024 pixels along this axis, we know that the camera has a capture interval of about 22 nm from end to end. It also means that the spectral distance between pixels is about 0.0215 nm. A previous estimation by Khater using low pressure Helium and Argon discharges in the 75 - 85 nm range produced lines which had a Full Width at Half

Maximum (FWHM) of about 2.1 pixels. Thus, the instrumental width of the entire optical system was 0.045 at 80 nm, a good comparison to the theoretically calculated value of 0.042 nm. The resolving power \mathcal{R} of the system using the values above is approximately 1780 at 80 nm using a 50 μm entrance slit width.

3.5 ANDOR TECHNOLOGY CCD CAMERA

The radiation detection system used in the LIPS experiments was a back-illuminated, VUV-sensitive Andor Technology CCD camera; model number DV420-BN. CCD cameras are, very basically, devices which convert photons into electronic charge that can be quantified easily. The CCD chip is a 2 dimensional array of Metal Oxide Semiconductor (MOS) capacitors. A single capacitor ("pixel") is shown in Figure 15 (after Holst, 1996).

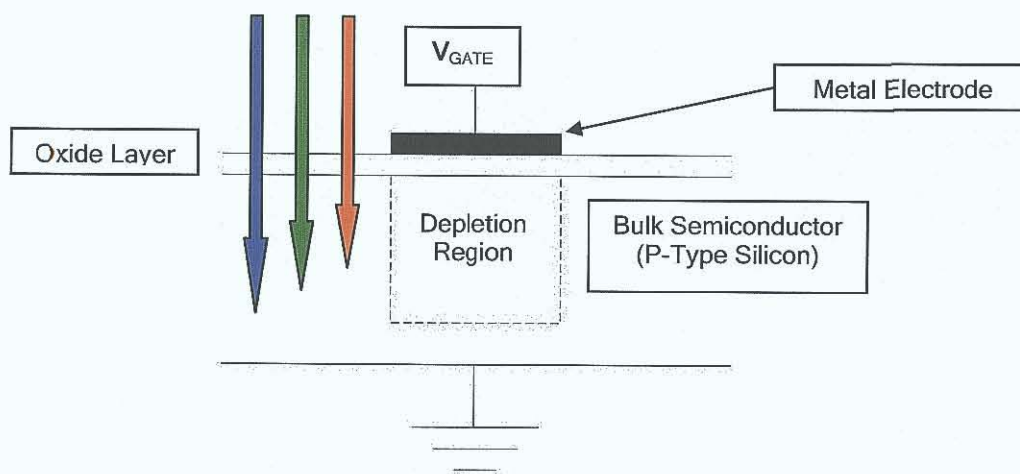


Figure 15: P-Type Silicon MOS Gate (after Holst, 1996)

When a positive voltage is applied to the gate of the sensor, the holes in the p-type material are filled with electrons and they virtually migrate towards the ground of the device. When the sensor is used to quantify and measure light intensity, photons are incident on the surface of the sensor and penetrate gate structure to a certain degree. As they pass through the gate structure and into the depletion region of the sensor, either one or more electron-hole pairs are produced. It's these positive or negative charges that can then be read and interpreted as light intensity. It should

be noted that Figure 15 is not to scale - the depletion region produced is on the nm/ μ m scale, whereas the bulk chip is generally millimetres thick.

The gate structure is the main cause of losses in front-illuminated systems, as it will absorb photons to a varying degree down to about 350 nm, below which nearly all of the incident radiation is absorbed by the gate. Indeed, for an electron-hole pair to be produced in the first place the wavelength of the incident photon must be at least 1100 nm as the bandgap in silicon is about 1.2 eV. For detection at wavelengths lower than 350 nm, a back-illuminated or back-thinned chip is used. Such chips operate in reverse compared to the usual front-illuminated arrays in that the gate structure is *not* on the side of the sensor facing the incoming radiation. This way, the radiation can be absorbed directly by the depletion region by thinning the bulk semiconductor material until it appears to be transparent, about 10 - 15 μ m thick (Andor Technology, 2006).

When the light has been collected, charge for each pixel must then be read and transferred to a computer. In the DV-420BN, this is done using the *Progressive Scan* readout method, as shown in Figure 17 on the following page. This means that by "clocking" the array of pixels i.e. alternating the gate voltage on each pixel, the charge on each pixel can be transferred down into a device which both collects and addresses each charge called the shift register. The shift register can then pass the train of electronic pulses through an amplifier and on to a 16 bit digitising card in a PC so an image or spectrum can be seen on the computer screen. The 16 bit digitiser has the limitation of only being able to read up to 2^{16} counts from the CCD camera, so the camera in use has a saturation level of 65536 counts/pixel.

In the LIPS experiments conducted in chapters 4 & 5, the camera was used in "full vertical binning" mode. When a CCD camera is binned, it means that all the charges accumulated from specified pixels are added together. Full vertical binning refers to charges from an entire vertical column of pixels being summed. An unbinned image on the CCD camera chip is shown below in Figure 16.

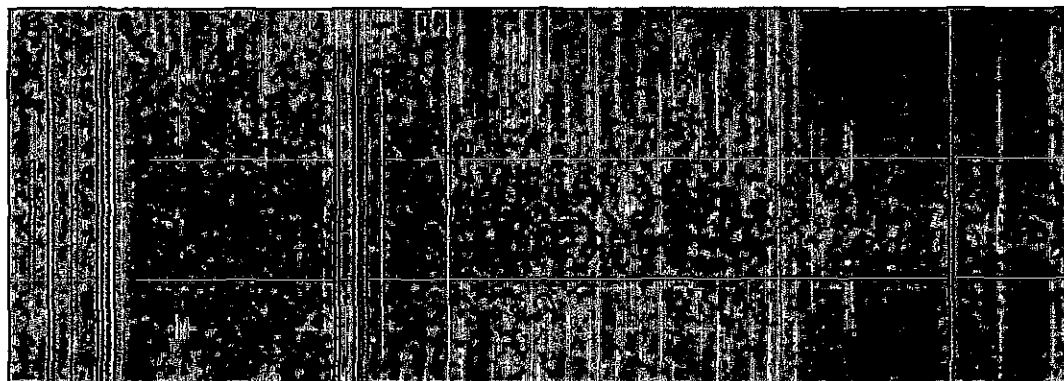


Figure 16. Unbinned CCD Camera Image

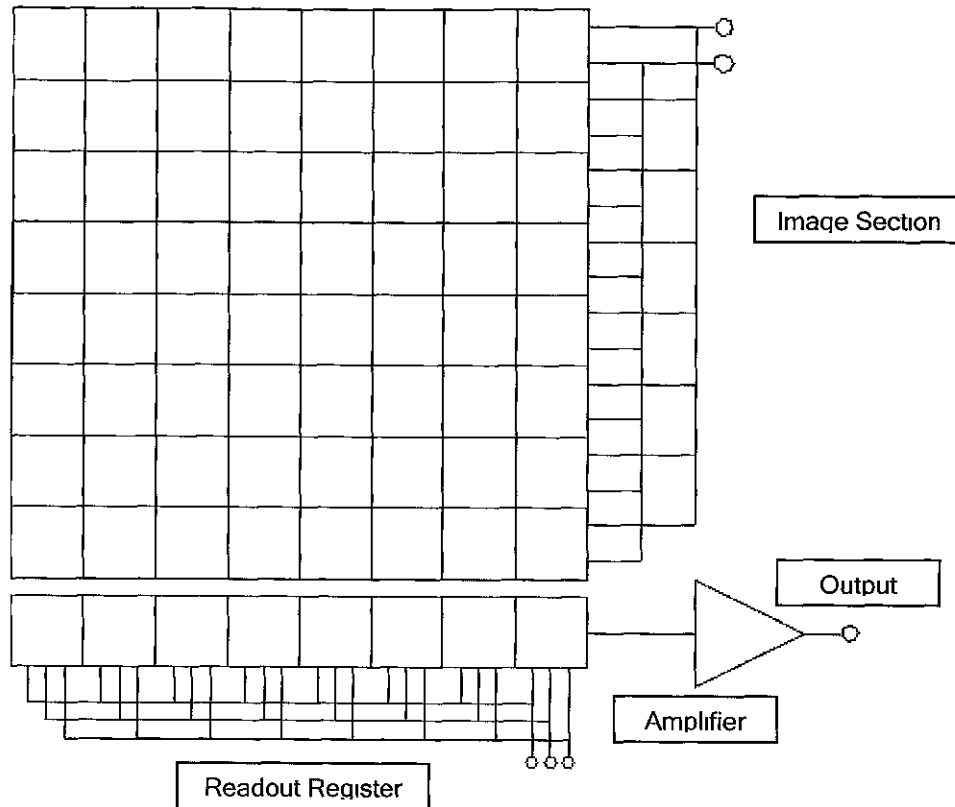


Figure 17. Full Frame CCD Chip

Binning has 2 advantages - it reduces the noise present in the spectra as the noise on each pixel is not amplified individually and it also increases the readout speed. An incorrectly aligned CCD camera may affect spectra however, with spectral lines being summed in several columns. The 16 bit saturation limit also applies in full vertical binning mode, so saturation levels displayed by the camera software are a maximum of 65536 counts/column.

3.5.1 QUANTUM EFFICIENCY & NOISE

The quantum efficiency of the CCD camera is a measure of the sensitivity of the camera at varying wavelengths of incident radiation. As mentioned previously, front-illuminated cameras tend to be opaque to radiation below about 350 nm - these cameras are said to have a quantum efficiency of ≈ 0 at these wavelengths. On the other hand, a perfect camera would be said to have a quantum efficiency of 1 i.e every photon incident on the detector face would be absorbed into the depletion region in each pixel. In practice, CCD cameras lie somewhere in between these two

extremes. For the DV-420BN, in its normal operating range of 30 - 130 nm the quantum efficiency lies between 19 and 42% respectively. At the spectrometer/grating blaze wavelength of 80 nm, the efficiency is 30% (after private communication with the manufacturer).

Noise in the camera was dealt with in two ways. The first was cooling of the CCD chip. A Peltier-type cooler permits thermoelectric cooling of the CCD chip to temperatures as low as -40°C without an external water flow and -80°C with. Since such extreme temperatures can damage the CCD chip due to ambient water vapour condensation, the camera was cooled to -20°C in normal operation. At this temperature, the dark current was reduced to a specified level of about 3 electrons/pixel/second.

Noise was removed from spectra by subtracting a pre-recorded background spectrum, something done automatically by the camera software. Background spectra were taken in exactly the same conditions as the spectra themselves but without the laser in operation. In this way, the background count was reduced dramatically. Test spectra consisted of 20 accumulations, so a corresponding background spectrum was recorded in each case. This resulted in an average background value of about 100 counts (dependent on distance from the target and pulse energy) for each column of pixels, giving an average noise value of 0.02 counts/pixel/shot.

3.6 VACUUM GENERATION SYSTEMS

As previously mentioned, air absorbs VUV radiation. This means that experiments must be performed in vacuum conditions if the experimentalist wishes to observe VUV spectral features. Luckily, below a pressure of about 0.1 mBar, air can be considered perfectly transparent to VUV radiation for short path lengths (Henke, Gullikson & Davis, 1993). These pressures are relatively simple to reach using modern vacuum pumps. Two stage rotary pumps were sufficient on both the target chamber and spectrometer, with small (50 l/min) and large (150 l/min) turbomolecular pumps attached as secondary stages respectively on each. An ultimate pressure of 2×10^{-6} mBar was reached on the spectrometer in normal operation, while a slightly higher pressure of 3.5×10^{-6} mBar was achieved on the target chamber, due to its larger number of ports. Both target chamber and spectrometer had Pirani and Penning gauges attached to monitor pressures on a constant basis. In the instances

where gases other than air were present in the target chamber, the pressure gauge had a user-controlled correction factor that can be changed from the gauge controller.

In experiments where ambient gases were used in the target chamber, a needle valve was used to regulate pressure in the chamber from the gas lines. Pressures up to 1 mBar were used in the target chamber which meant that the pressure in the spectrometer rose, since the aforementioned GCA is capable of maintaining only 3 orders of magnitude differences in pressure. This meant a rise in the spectrometer pressure up to 10^{-4} mBar, low enough that a significant change in detection conditions was avoided.

3.7 SYSTEM TIMING & SYNCHRONISATION

Synchronisation in laser plasma experiments is very important given the transient nature of the plasmas created. Since the typical emission lifetime of a laser plasma in vacuum is of the order of microseconds, it is important that the appropriate radiation collection systems have the capability of being finely manipulated to a high degree of precision. As such, the timing in the LIPS experiments was controlled almost exclusively by the CCD camera software in the following manner.

The Surelite III-10 is capable of operating on its own internal timing structure or it can be controlled externally. The more accurate of the two is the full external triggering scheme which has a jitter of ± 1 ns, as compared to the semi-external mode which has a jitter of ± 10 ns. This means that triggering of both the flashlamps and the Pockels cell by an external source is required. In this instance, the Stanford Research Systems model DG535 delay generator was used. The DG535 is capable of producing extremely sharp TTL pulses of very low width at a fixed frequency, has several outputs that can be synchronised with one another and can also be triggered externally. Here, the DG535 was triggered externally using the Multi I/O box provided with the CCD camera. The timing scheme used for experiments is shown on the next page in Figure 18. All the pulses shown are 5 V TTL.

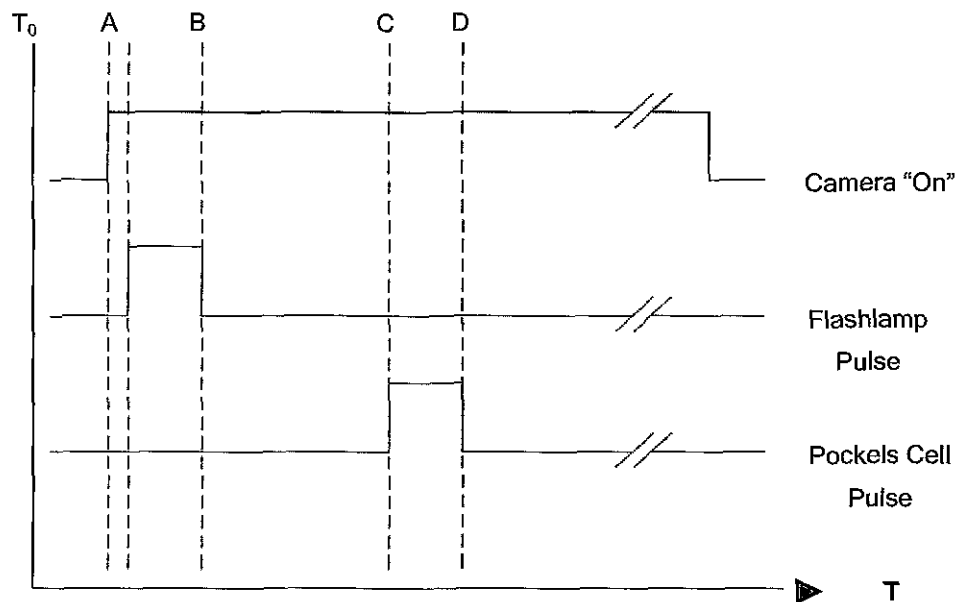


Figure 18: Experimental Timing Scheme

The laser operates at a frequency of 9.882 Hz which cannot be changed. Owing to this, the above timing scheme is repeated at this frequency for the desirable number of repetitions. At T_0 , the camera is switched on using software provided with the camera. In the camera's own internal timing, the accumulate cycle is the amount of time between each exposure i.e. the time when the CCD chip captures light. This is determined by the cycle time of the laser, so the accumulate cycle time is 102 ms. This corresponds to an exposure time of 39 ms, shown as "camera 'on'" in Figure 18. There is a short time between the camera switching on and the delay generator sending the first pulse to the laser, the flashlamp trigger pulse which is 10 μ s in duration. The second pulse is the Pockels Cell pulse i.e. the pulse which switches on the Pockels Cell, also 10 μ s long. This is sometimes used as a method of controlling laser energy, although the spatial characteristics of the beam suffer as a result (see section 3.2). The laser pulse itself is produced at the rising edge of the Pockels Cell pulse, and has a duration of 6 ns. After the laser pulse has impacted the target surface, the plasma is produced, observed and extinguished before the commencement of the next pulse train.

3.8 SUMMARY

The equipment used in the VUV LIPS experiments has been described with the method in which it was used explained. The major features of the experimental components including the spectrometer & grating, the CCD camera and the Nd:YAG laser have all been individually expounded on and each part they play detailed. The physical process that each part works on was defined as is relevant to the experiments in the following chapters.

REFERENCES

- Andor Technology: *Scientific Digital Camera Solutions*, © Andor Technology 2006.
- Burle Industries Inc.: <http://www.burle.com/cgi-bin/byteserver.pl/pdf/tp184.pdf>, GCA product data sheet.
- Doyle B: "A 1m Normal Incidence Multi-Channel Spectrometer for Laser Plasma Spectroscopy". M Sc thesis, Dublin City University (1995)
- Hecht E: *Optics: Third Edition*, Addison Wesley, 1998
- Henke BL, Gullikson EM & Davis JC: "X-ray Interactions: Photoabsorption, Scattering, Transmission, and Reflection at $E = 50 - 30000$ eV, $Z = 1 - 92$ ", *Atomic Data and Nuclear Data Tables*, **54**, no 2, pp. 181-342 (1993).
- Holst GC: *CCD Arrays, Cameras and Displays*, JCD Publishing and SPIE Optical Engineering Press, 1996.
- Khater M: "Spectroscopic Investigations of Laser-Produced Steel Plasmas in the Vacuum Ultraviolet". Ph.D. thesis, Dublin City University (2002).
- Mack JE, Stehn JR & Edlén B: "On the Concave Grating Spectrograph, Especially at Large Angles of Incidence", *Journal of the Optical Society of America*, **22**, p. 245 (1932)
- Meighan O: "XUV and VUV Photoabsorption and Emission Studies in Thorium and Other High-Z Laser Plasmas". Ph.D. thesis, Dublin City University (2000).
- Melles Griot: Lens Data Sheet, *Melles Griot Catalogue* (2004).
- Moenke-Blankenberg, L. *Laser Microanalysis*, Wiley, 1989.
- Namioka T: "Theory of the Concave Grating I", *Journal of the Optical Society of America*, **49**, pp. 446 - 460 (1959).
- Namioka T: "Theory of Ellipsoidal Concave Grating I.", *Journal of the Optical Society of America*, **51**, pp. 4 - 16 (1961).
- Samson JAR: *Techniques of Vacuum Ultraviolet Spectroscopy*, Wiley, 1967.
- Smith FG & King TA. *Optics and Photonics: an Introduction*, Wiley, 2000
- Winefordner JD et al.: "Comparing Several Atomic Spectrometric Methods to the Super Stars: Special Emphasis on Laser Induced Breakdown Spectrometry, LIBS, a Future Super Star", *Journal of Analytical Atomic Spectrometry*, **19**, pp. 1061 - 1083 (2004)

CHAPTER IV: SULPHUR DETECTION IN STEEL: VACUUM CONDITIONS

Experimental work on sulphur detection in steel matrices began with investigations of detectable sulphur lines in the Vacuum Ultraviolet region of the spectrum under vacuum conditions. This work was used to form an initial understanding of the emission characteristics and the best wavelength region in which to perform basic spectroscopic studies. Surveys of the VUV region were conducted under a varied number of parameters - the most salient results and subsequent detection limits for sulphur are presented here.

4.1 INTRODUCTION

As a precursor to the ultimate goal of reducing the achievable detection limit of sulphur in steel, an initial investigation into sulphur emission under vacuum conditions was conducted. This initial parameterised study forms a baseline for comparison of the vacuum VUV technique against other, similar studies made on sulphur detection using LIPS and also possible further investigations into sulphur detection using the VUV region. As a study of sulphur emission in different conditions, an understanding of emission under vacuum was the simplest starting point for a wider investigation into the characteristics of the laser plasma and how the various components behave in different conditions.

4.1.1 VUV TRANSMISSION COEFFICIENTS

Several sulphur lines in the deep VUV (below 100 nm) have been used as both temperature (Curdt, 1997) and density (Laming, 1997) diagnostics for applications in stellar physics, but to date no group has used these deep VUV lines for quantitative analysis using LIPS. The reasons for these are twofold - experiments in the VUV tend to be more difficult to perform than experiments in the UV, visible or IR ranges as vacuum systems must be used due to significant atmospheric absorption of VUV radiation as seen below in Figure 1 (CXRO Matter Interaction Calculator).

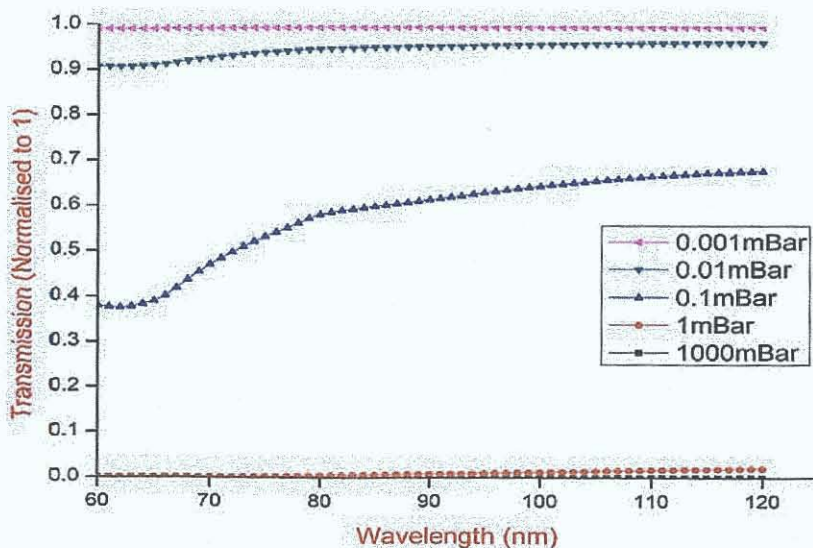


Figure 1: Calculated Gas Transmission Curves for VUV Radiation at Different Pressures (1 m path length)

As plotted, it can clearly be seen that VUV transmission in the mid to deep VUV range is poor for pressures ranging from atmospheric pressure down to 1 mBar. Only below pressures of 1 mBar do the transmission coefficients start to increase to acceptable levels for emission spectroscopy. All data has been plotted for transmission through air for a total distance of 1 m using the CXRO interaction tool (ref CXRO). Since most LIPS applications (especially analysis of industrially important metals) are geared towards online analysis of materials, the VUV region has several critical shortcomings that have limited the study of this area, the main one being the need for evacuated apparatus, again due to atmospheric absorption.

A solution used by Sturm et al. was to use VUV lines in the near VUV i.e. lines above 175 nm. At this wavelength, absorption by air isn't critically significant to the result of the experiment and elemental lines can be resolved reasonably unperturbed by the ambient atmosphere. This approach is satisfactory for many applications, but ultimate sensitivities tend to lie with the stronger resonant emission lines, which are found deeper in the spectrum. One possible change in the experimental apparatus for an industrial configuration of the vacuum system would be to forego the use of a turbomolecular pump on the spectrometer - this would further reduce the equipment cost whilst still producing an ultimate pressure approaching 10^{-2} mBar. At this pressure, radiation from the laser plasma has a 90% or greater transmission coefficient through the spectrometer - perfectly acceptable for emission spectroscopy.

4.2: TIME INTEGRATED SPACE RESOLVED LIPS

Time-Integrated Space-Resolved (TISR) LIPS is a breakaway from the standard LIPS experiment often seen in the literature (e.g. Hemmerlin, 2000). These standard studies generally exploit the temporal nature of the laser-produced plasma, using a time-gated detector to capture different expansion stages of the plasma. As discussed in chapter 2, one of the main features of a laser-produced plasma is the broadband continuum emission produced in the initial stages of plasma formation and expansion. As the plasma cools and expands, the continuum emission from the hot plasma dies off and is replaced by a longer-lived line emission phase. A time-resolved detector has the advantage of non-capture in these early stages with capture times optimised for line emission phases later in the plasma. One disadvantage is that line emission from these early stages of the laser-produced plasma expansion is also blocked. This emission is generally more intense than that produced at later times, but with the continuum emission correspondingly high it is

impractical to study emission at this point since the most relevant figures in the technique are line emission intensity and the standard deviation in the background emission levels. Figure 2 (after Eliezer, 2002) is a representation of a typical laser-produced plasma - note the spatial distribution of the hot and cold zones in the plasma.

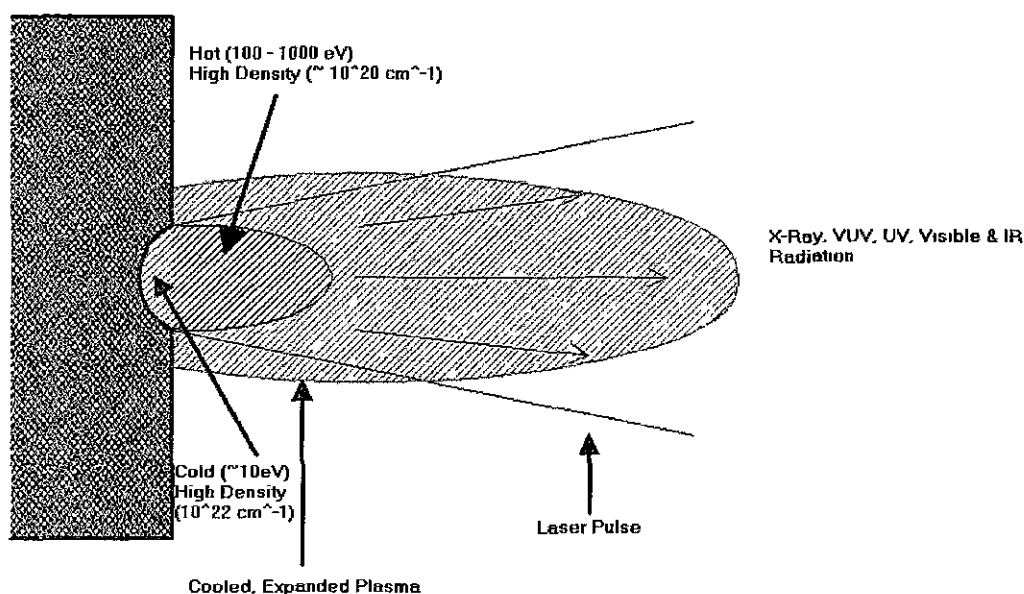


Figure 2 Typical Laser-Produced Plasma (After Eliezer, 2002)

The solution used in the present work is one based on the spatial characteristics of the continuum radiation in the plasma. As the plasma expands out from the target surface, continuum emission is replaced by line emission due to a drop off in the electron density and temperature in the plasma (Radziemski & Cremers, 1989). This means that radiation from the entire duration of the laser-produced plasma lifetime can be captured if the zone close to the target surface is shielded from the spectrometric system. This was achieved with the pre-slit, as described in chapter 3, section 3.3.1 Figure 3 shows the difference in spectra (taken with identical plasma formation conditions) at different distances from the target's surface. An interesting feature to note is that the line emission decreases by about half for each 0.5 mm step in distance from the target surface.

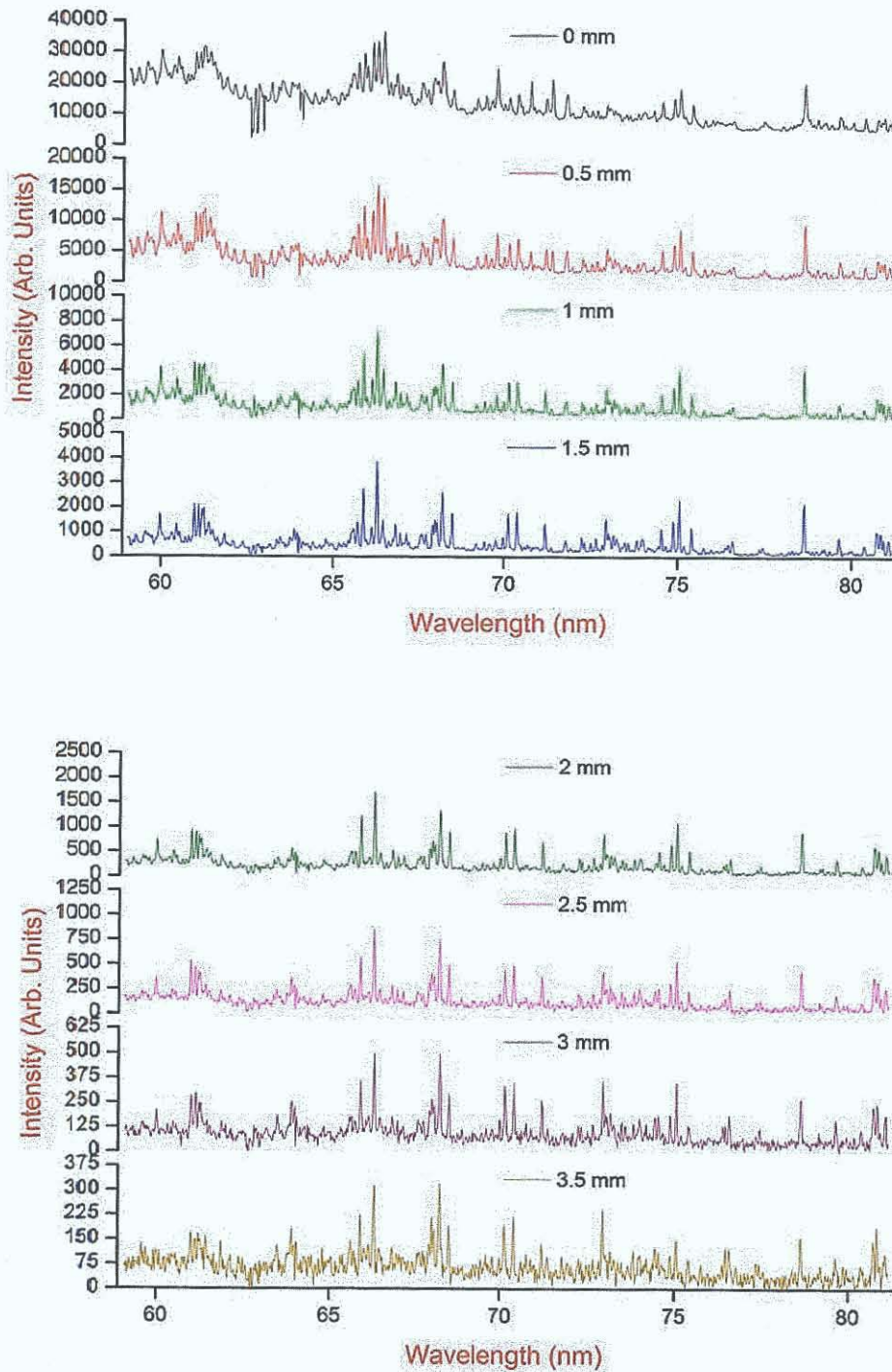


Figure 3: Intensity Variation with Spatial Distance - 100 mm Spherical Lens

The conditions under which the spectra were recorded were an accumulation of 20 820 mJ pulses focussed using a 100 mm plano-convex lens at a depth of 1 mm below the target surface. It can clearly be seen from the above figure that there are marked differences in both the intensity and underlying structure of the plasma

spectra as the perpendicular sampling distance increases. The black spectrum at the top of figure 3 is that of the laser-produced plasma captured at the target surface (0 mm) and shows the typical sloped shape of continuum emission from the laser-produced plasma overlaid with line emission from later stages of the laser-produced plasma as it expands and cools. As the distance increases, the radiation intensity concomitantly decreases - it is using this property that optimisation studies are conducted

Effects can be seen for changes in experimental conditions such as a variation of the laser spot size, a variation in the incident power density and considerations like the width of the spectrometer's entrance slit. All of these parameters must be varied in order to find optimal conditions for analysis of the sulphur levels in the laser plasma. As discussed in chapter 2, section 2.6, these parameters can have a significant influence on the sensitivity of the analytical technique.

As conditions influencing the formation of the laser-produced plasma are changed, the signal to background ratio of line emission to background emission in the spectrum changes accordingly. As explained in chapter 2, section 2.6, the Limit of Detection (LOD) is calculated using a ratio of the standard deviation (σ) to the slope of a line called the calibration curve which plots the intensity of a spectral feature against the concentration of the emitting species in the target. The general trend is to use the signal to background ratio of a spectrum to gauge the merit of a set of parameters in comparison with one another. In the present study, the author used the signal divided by the actual standard deviation in the background levels of each spectrum in order to more accurately observe the optimum conditions for analytical study since the standard deviation is the actual figure used in the LOD calculations

Conditions can be modified in such a way as to show where samples may be analysed with the greatest sensitivity by observing where the Signal to Standard Deviation Ratio (SSDR) peaks. In the following sections, the laser-produced plasma formation parameters are modified systematically in order to determine the initiation conditions where the TISR-LIPS technique can be applied most successfully. First of all however, a suitable line was required so that a truly comparative study was possible.

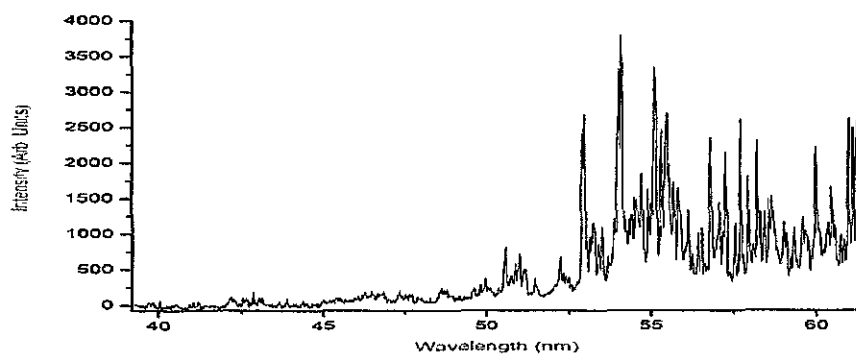
4.3 LINE IDENTIFICATION

Choosing a line as a basis for analytical studies on spectra can pose some difficulties for the experimenter. Spectral line databases such as the Kurucz online atomic line database (ref. Kurucz), Kelly's tables online (ref. Kelly) and the NIST online atomic spectra database (ref. NIST) are essential sources of information on line position and theoretical relative intensity values which are useful when spectra are to be calibrated and lines in them attributed to elements and their respective ionisation stages. The detector software itself has no calibration tables for the type of spectrometer used in these experiments, so manual calibration of line wavelength must be performed. In this case, some critical information on the camera and spectrometer dispersion is known. From previous calculations in chapter 3, we know that the dispersion across the camera face is a little over 21 nm. Since the method of dispersion of the spectrometer grating means that the wavelength "dialled in" to the spectrometer is the central wavelength on the camera face, estimates of line wavelengths can then be made using the available databases and previously calibrated spectral lines.

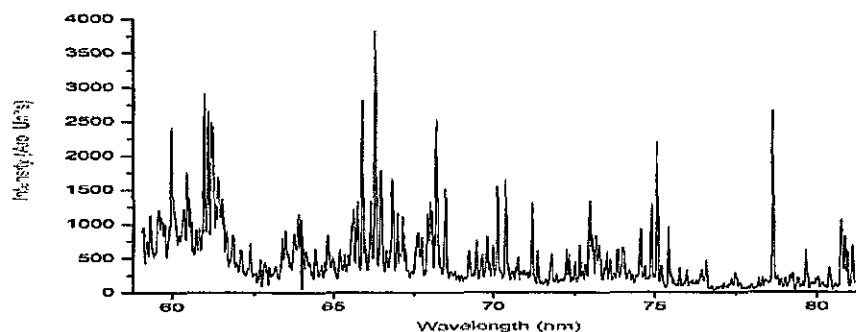
A survey of the VUV region was conducted in order to see which sulphur lines were observable in the wavelength range of the instrumentation. The lower limit of the spectrometer is 30 nm and the upper practical limit is about 140 nm - this is due to second order radiation from the blaze angle of the spectrometer grating (Chapter 3, section 3.4.3) being detected at higher wavelengths and interfering with the natural first order radiation from the laser-produced plasma. The basic premise of the survey was to find a "window" in the iron emission which correlates with emission from a strong sulphur line. It should be noted at this point that many LIPS studies are hampered by the so called "matrix effect" (Winefordner et al., 2004) - background emission from the major constituent of the sample can sometimes swamp emission from minor elements in the sample thus rendering the analytical technique less sensitive than hoped for. The matrix can also have an effect on the calibration curve of an element due to the possibility of some spectral information from the line under analysis being hidden in the background count. By ensuring that lines are only measured in matrix windows, it can be assumed that any lines in these windows are from minor elements in the target. These lines can then be assessed for use in an analytical capacity.

4.3.1 LIPS LINE SELECTION

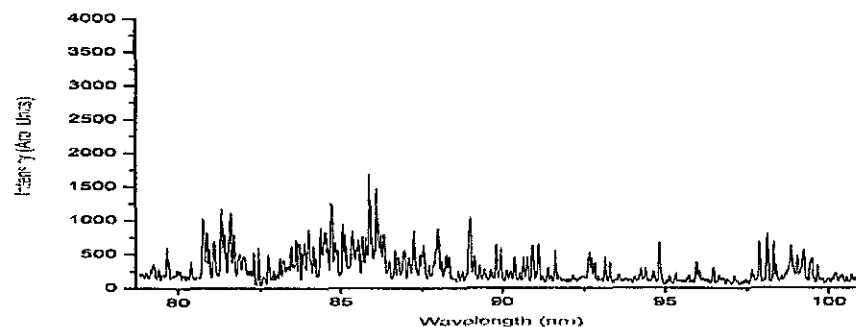
The following series of graphs (Figure 4) are typical of the spectral survey throughout the entire practical VUV range. Intensities in each graph are to the same scale, while plasma formation conditions remain constant: 20 laser shots focussed by a 100 mm spherical plano-convex lens, defocused forward into the target 1 mm with all targets under vacuum - the spectra themselves were recorded at a distance of 2 mm from the target surface to avoid "contamination" from the continuum element of the laser plasma. The target used was a "binary" - a target composed of only two elements, in this case iron and sulphur (the sulphur content is 0.68%).



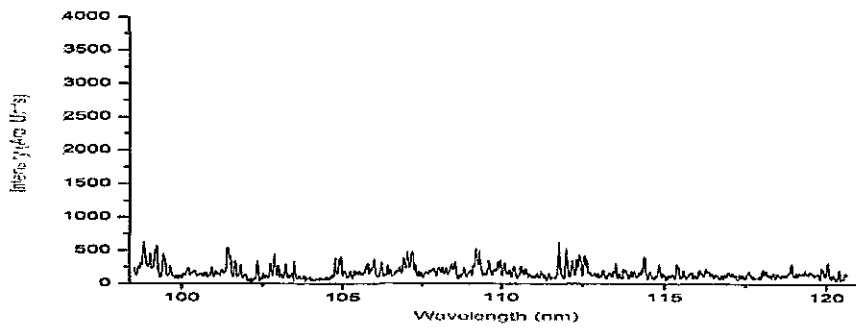
A) 40 - 60 nm



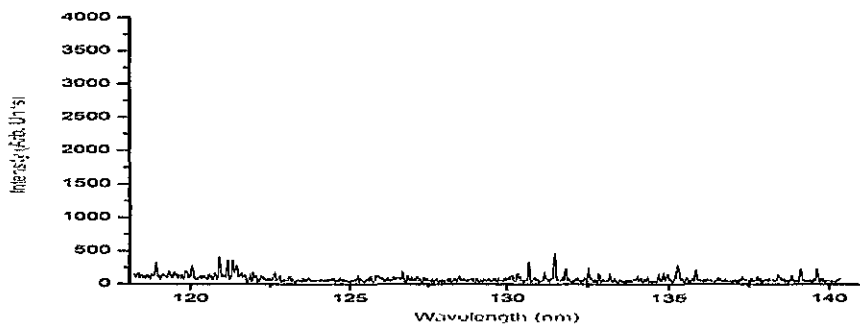
B) 60 - 80 nm



C) 80 - 100 nm



D) 100 - 120 nm

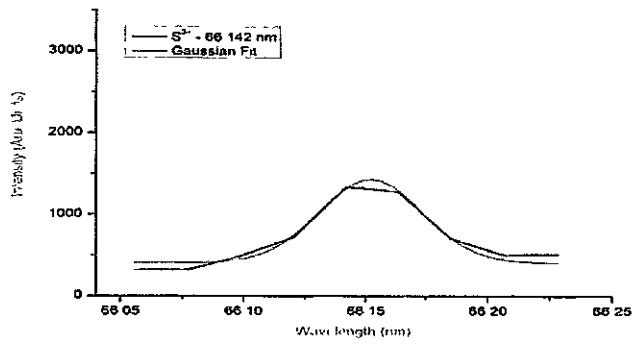


E) 120 - 140 nm

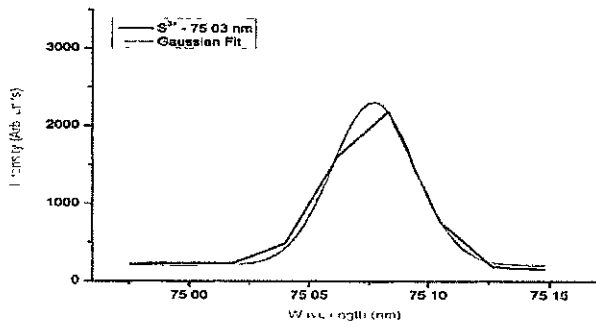
Figure 4 VUV Emission Survey A) 40 - 60 nm, B) 60 - 80 nm, C) 80 - 100 nm, D) 100 - 120 nm, E) 120 - 140 nm

The first major feature of this spectrum is the large emission band running from 50 nm to just over 75 nm. Mainly composed of Fe^{2+} ions, this area is clearly unsuitable for sulphur analysis due to high matrix effects. A strong sulphur line (S^{3+} , 66.14 nm) is occluded by this band. A sharp decrease in emission by all elements runs from 100 to 140 nm, with spectra being composed of weakly emitting iron and sulphur lines. A significant feature of spectrum B, however, is observed near 80 nm. This seemingly isolated line is, in fact the resonant S^{4+} transition at 78.65 nm. From the recorded spectrum, it can be seen that there are few lines in proximity and that the line itself is a strong. Another fortuitous factor with this line is that it lies very close to the blaze wavelength of the spectrometer grating.

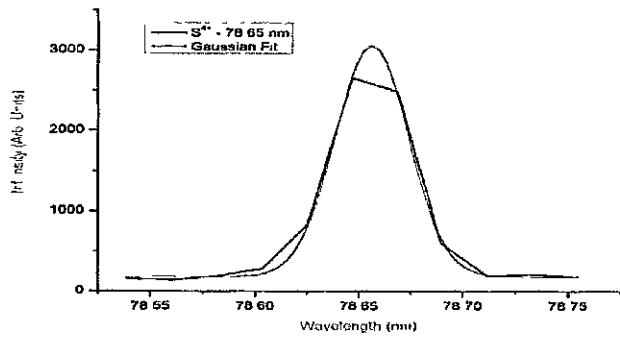
Using Kelly's tables and the line intensity values observed in the spectral survey, several sulphur lines were chosen to compare suitability for optimisation. Figure 5 below shows the lines under comparison.



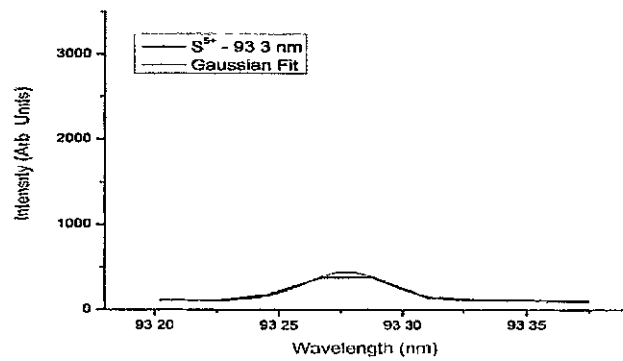
A) 66 142nm



B) 75 03nm



C) 78.65nm



D) 93 3nm

Figure 5: A) S IV - 66 142 nm, B) S IV - 75 03 nm, C) S V - 78.65 nm, D) S VI - 93.3 nm

The red lines in the above series of graphs represent curve fits to the spectral lines using Microcal Origin™ curve fitting and data manipulation software. For further information about spectral curve fitting in this work, please refer to Appendix 1. Table 1 below is a comparison between the relevant attributes of each of the lines presented.

Table 1: Line Comparison

Line (nm)	Peak Height (Arb. Units)	Peak Area (Arb. Units)	R ² Value
S ³⁺ 66.142	1428	54.48	0.972
S ³⁺ 75.03	2304	91.54	0.997
S ⁴⁺ 78.65	3060	127.68	0.999
S ⁵⁺ 93.3	442	14.138	0.995

As seen in the table and from the previous graphs, the clearest line in terms of isolation and size is the S⁴⁺ line found at 78.65 nm. Below in Figure 6 is shown the Grotrian diagram of these energy levels in relation to the ground state of the sulphur atom.

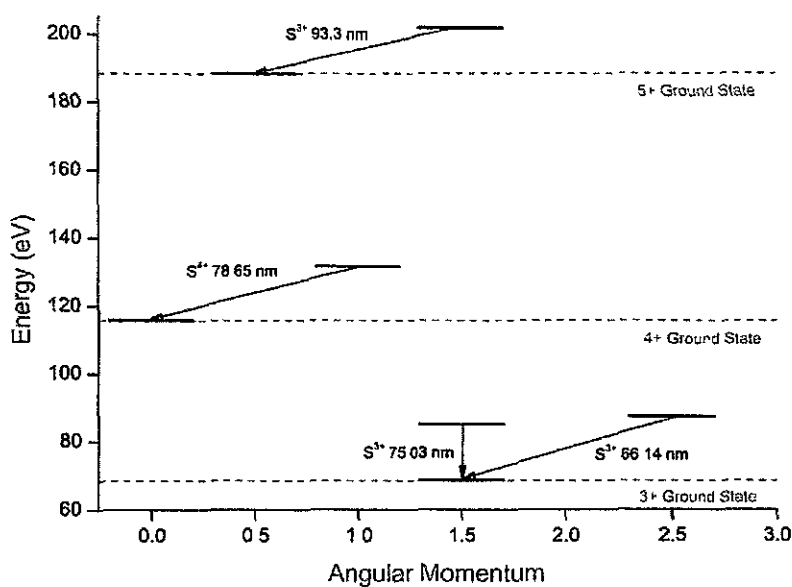


Figure 6: Grotrian Diagram of Relevant Transitions

The transitions resulting in the 4 spectral lines observed are resonant transitions in that they all involve transitions from a higher energy state to the ground energy state of the ion. These transitions are named according to similar transitions in neutral species with the same number of electrons e.g. a S^+ transition would be similar to a transition in neutral phosphorus, and would be called a P-like transition. The S^{4+} transition at 78.65 nm, $2p^63s^2 - 2p^63s3p$, is a Mg-like resonant transition while the S^{5+} transition at 93.3 nm, $2p^63s - 2p^63p$, is the Na-like ground state transition. The other lines investigated were from Al-like S^{3+} with the transition at 66.142 nm ($3s^23p - 3s^23d$) and that at 75.03 nm ($3s^23p - 3s3p^2$) both resonant.

Now that a suitable line had been selected, the next stage in the study was to systematically vary the plasma formation and capture parameters in order to optimise the signal to background ratio (SBR) in each of the spectra. This ratio is calculated by dividing the intensity of the sulphur line by the standard deviation in the background of the spectrum itself (taken from clear parts of the spectrum) using the curve fitting tool in Microcal™ Origin™.

4.4 SPHERICAL VS. CYLINDRICAL LENSES

One of the options available in creating a laser-produced plasma is the type of lens to use. The standard method in VUV laser-produced plasma spectroscopy is to use a spherical plano-convex lens to create the plasma, as this maximises the power density on the target. Such a lens is diffraction limited, as outlined in chapter 3, section 2.1. VUV transitions are typical of ions in a relatively high state of excitation and therefore for a reasonable quantity of VUV radiation to be observed from a laser-produced plasma, a large amount of energy is required to excite an observable number of atoms into the energy states required. The usual approach to laser-produced plasma initiation is therefore to use a spherical lens as it maximises the power density on the target. However, cylindrical lenses which produce line plasmas offer plasma parameters that are markedly different from spot plasmas formed by spherical lenses. Since the pulse energy is spread over a wider area, the power density is lower but the actual plasma volume is larger. This means that there may be energy regimes under which a larger volume of lower temperature plasma produces more radiation from certain lines than a higher temperature but smaller plasma. Figure 7 shows the difference in power density on target for the 2 different types of lenses, both having a focal length of 100 mm.

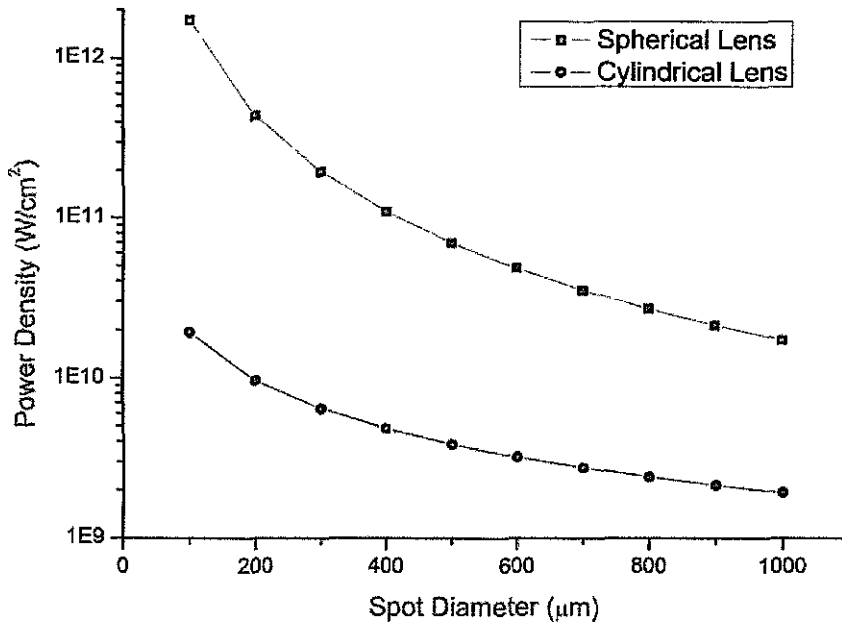


Figure 7: Calculated Power Densities with Varying Focus for Spherical and Cylindrical Lenses

As can be seen above, there is a very large difference in the power densities attainable with both lenses, typically in the region of more than an order of magnitude. In terms of the difference in plasma temperature due to these different power densities, a formula presented by Colombant & Tonon (1973) is used to estimate initial electron temperatures. Although Colombant & Tonon's original paper deals with high-temperature x-ray emitting plasmas, it is still interesting to use the formula:

$$T \approx 5.2 \times 10^{-6} A^{\frac{1}{5}} \left[\lambda^2 \phi \right]^{\frac{3}{5}} \quad [4.1]$$

to *estimate* the plasma's initial electron temperature - this model and associated formulae for calculating some of the characteristics of laser plasmas has been used successfully in the past (see for example Hirsch et al., 2000 and Dunne, O' Sullivan & O' Reilly, 2000). This is due to the fact that similar laser-produced plasmas fit the assumption that for intermediate electron densities (10^{19} - 10^{21}) such as those produced in plasmas created by Nd:YAG lasers, the collisional-radiative equilibrium model can be applied to the laser plasma, at least during the laser pulse itself (see Appendix A: Equilibrium in Plasmas). In [4.1], T is the electron temperature in eV, A is the atomic number of the bulk element in the target, λ is the laser wavelength measured in μm and ϕ is the power density on the target measured in W/cm^2 . In the

case of the data used to plot Figure 7 and assuming a $1.064 \mu\text{m}$ pulse on a target consisting mainly of iron ($A=26$), the following graph (Figure 8) shows the variation in initial temperature of the plasma due to varying power densities

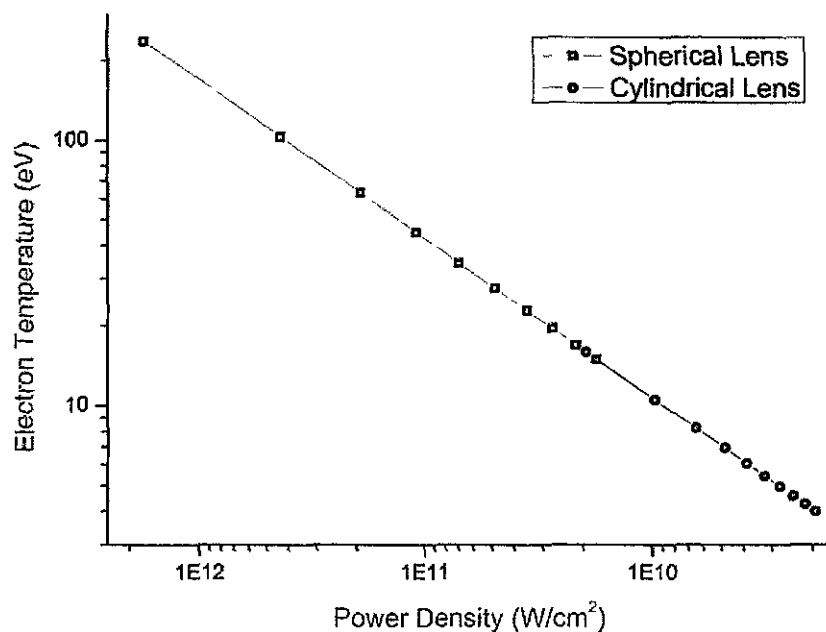


Figure 8 Columbant & Tonon Model Electron Temperatures - Cylindrical and Spherical Lenses

As is immediately seen, there is a large difference in the electron temperatures produced in the initial stages of the laser-produced plasma by each lens; an overlap in temperature is only seen for large defocusing of the spherical lens (1 mm spot diameter) whereas the cylindrical lens must remain tightly focused to achieve similar electron temperatures. The effects of the lower temperature but higher volume plasma can be seen below in Figure 9. Each of the spectra recorded were obtained using 20 820 mJ laser shots focused by a 150 mm cylindrical lens which was subsequently defocused 1 mm below the target surface.

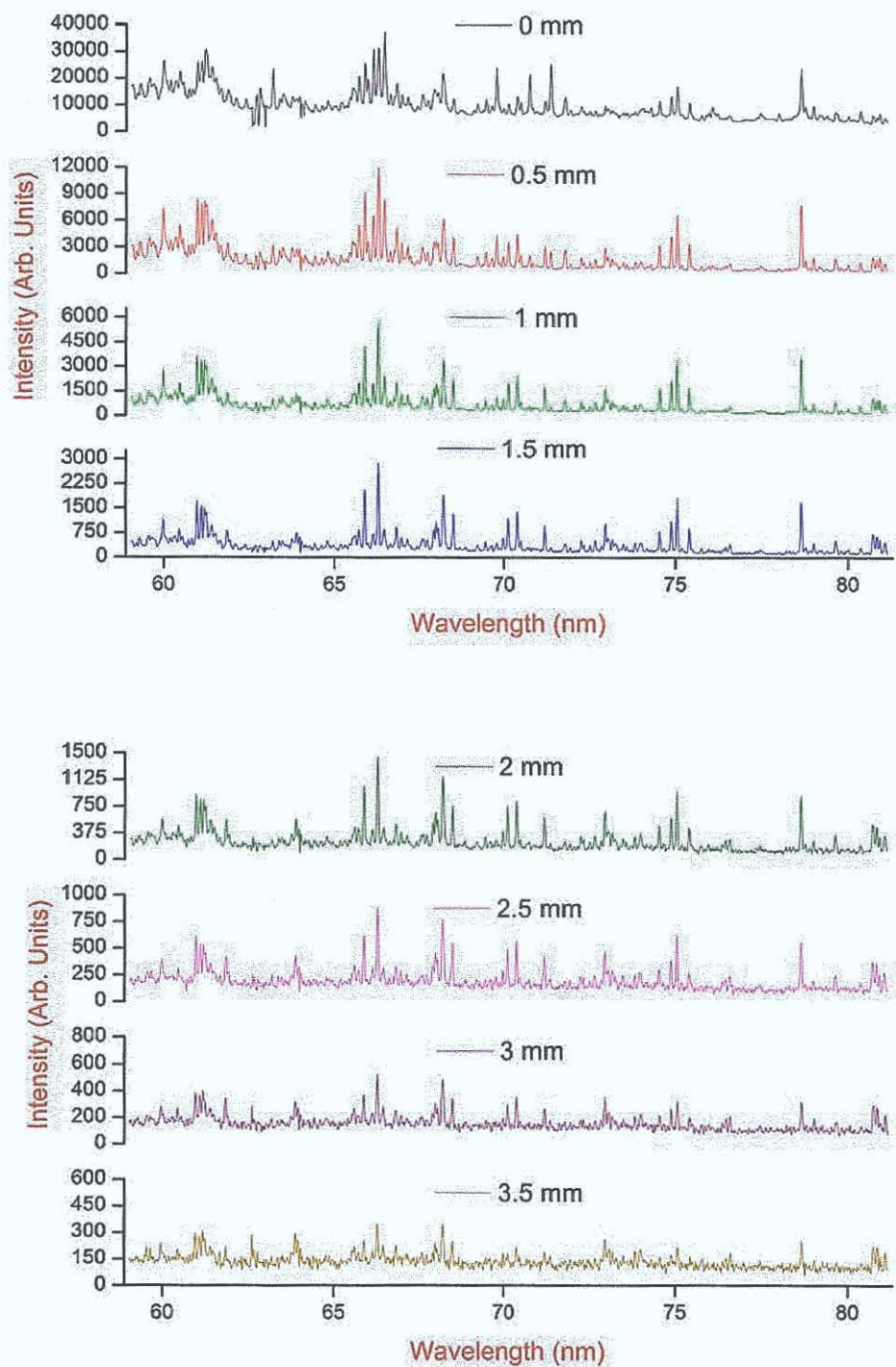


Figure 9: Spatial Spectral Variation using a Cylindrical Lens

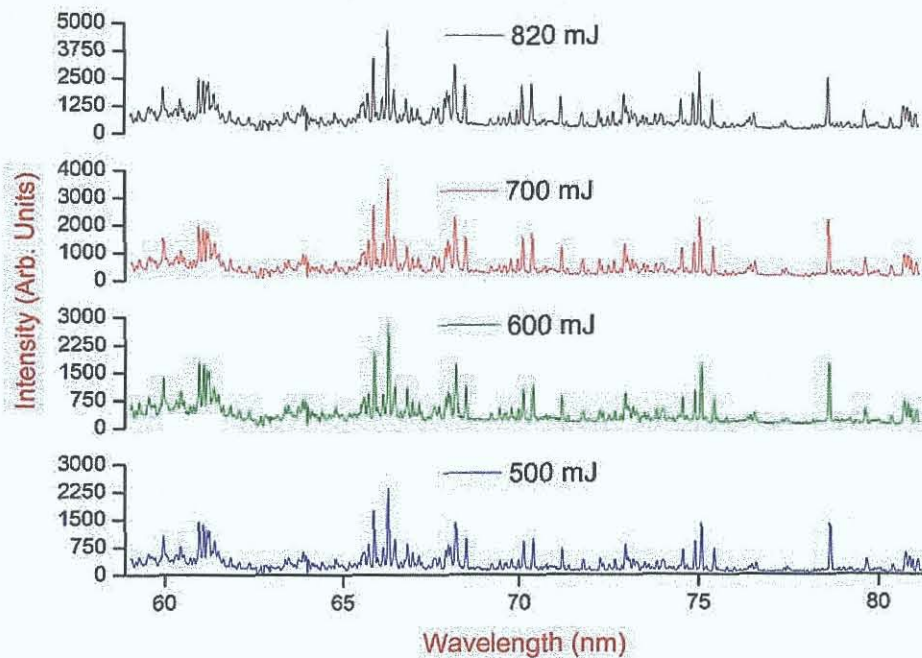
In comparing the above figure with Figure 3, some differences between each become apparent. Although the intensities of both spectra recorded at 0 mm seem more or less similar, there is a sharper drop in intensity with spatial distance in the

cylindrical spectra in comparison to the spherical lens spectra in Figure 3. The background in the spectra also seems to be “flatter” i.e. the effect of continuum radiation is muted in the lower temperature plasma.

The results obtained using both kinds of lenses are presented and compared in the following sections.

4.5 LASER PULSE ENERGY VARIATION

From Figure 3, the optimised Signal to Standard Deviation Ratio (SSDR) for the 100 mm spherical lens is measured to be at the 1.5 mm spectrum i.e. the spectrum recorded at a distance of 1.5 mm from the target surface. As such, the pulse energy was varied in steps of 100 mJ and a comparison made between spectra at 1, 1.5 and 2 mm. In each case the laser was focused 1 mm below the target surface in order to eliminate local instabilities in the target surface having adverse effects on the spectra i.e. if any microscopic roughness on the target surface was irradiated on the surface of the target, it might have altered the expansion dynamics of the plasmas plume. A larger spot size produced by defocusing the laser pulse into the target averages out these effects.



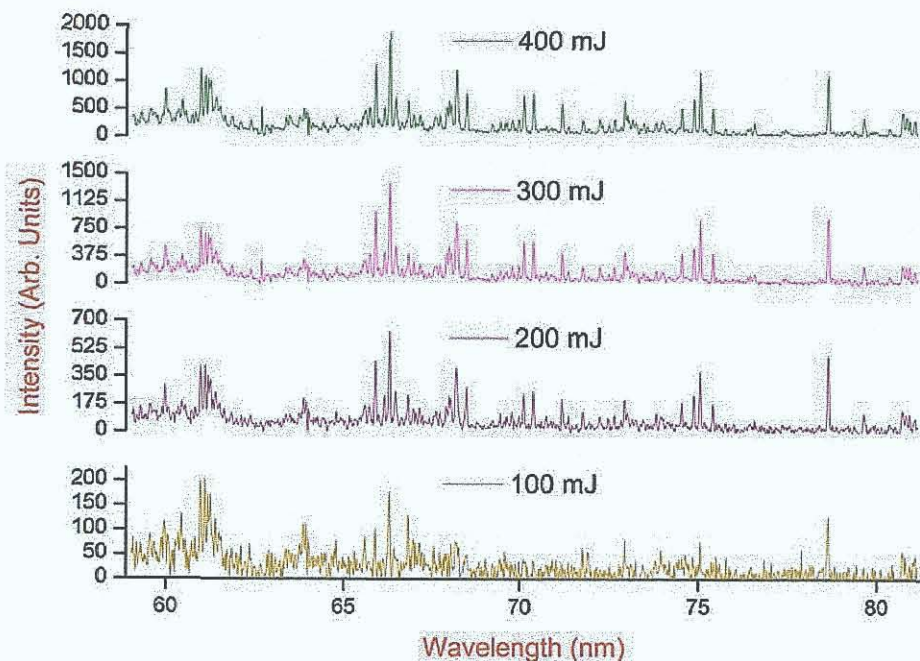


Figure 10: Energy Variation Effect at 1.5 mm - 100 mm Spherical Lens

As Figure 10 shows, there is a large variation in the intensity of spectral emission as the laser output changes. Although general trends in the laser-produced plasma can be gauged from this plot, the essential information lies with the SSSR information calculated from each individual spectrum. Figure 11 shows the SSSR data at the 3 most relevant spatial positions i.e. those that produced the highest signal values.

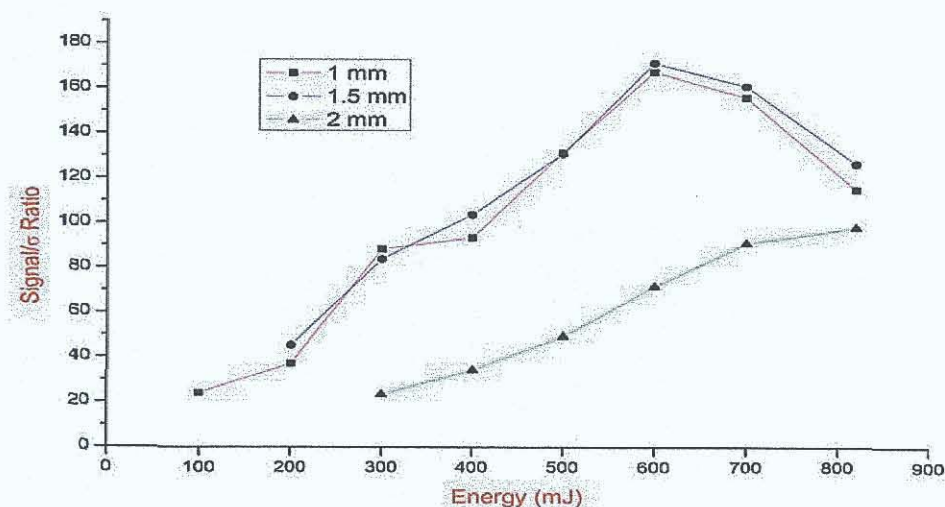


Figure 11: Signal to Standard Deviation Ratios for Varying Pulse Energies at 1, 1.5 and 2 mm - 100 mm Spherical Lens

Figure 11 shows that although SSDR data at 1 and 1.5 mm are similar, the data at 2mm is substantially lower. It must also be noted that curve fits from data taken at 1.5 mm were more accurate than those performed at 1mm due to decreased spectral interference from the underlying continuum radiation. Although the signal intensity decreased somewhat between 1 and 1.5 mm, the concomitant decrease in the background standard deviation decreased at a slightly greater rate and resulted in higher SSDR values for spectra at this distance.

Emission from plasmas produced with the cylindrical lens also produced SSDR levels which were optimised at 1.5 mm from the target surface. Figure 12 below shows spectra from a 150 mm cylindrical lens focussed 1 mm below the target surface captured at 1.5 mm from the target surface.

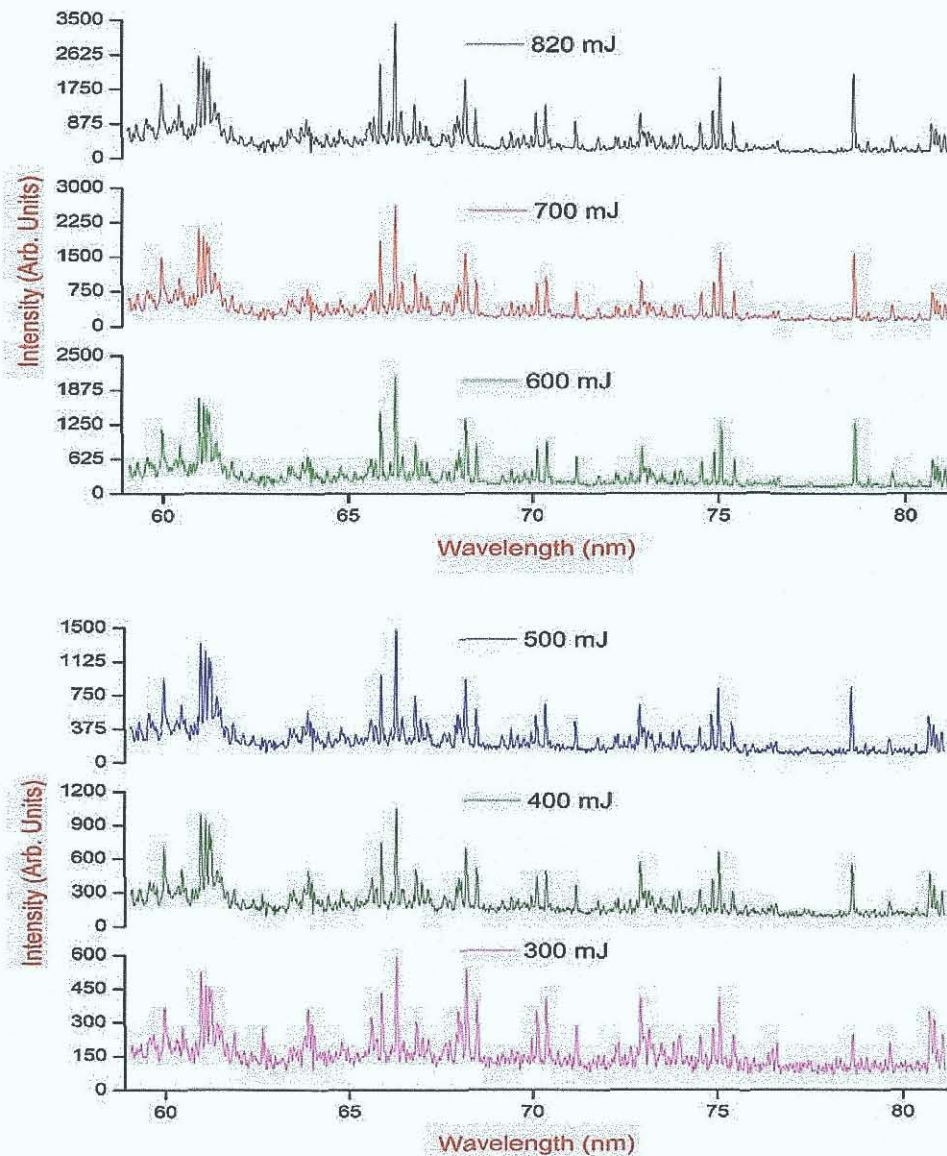


Figure 12: Energy Variation Effect at 1.5 mm - 150 mm Cylindrical Lens

The differences between this spectrum and those seen in Figure 10 are evident. Intensities of all lines are lower than those using the spherical lens, while the background intensity also seems to be muted. Also, there was little or no resolvable emission at energies below 300 mJ, compared with observable lines found at pulse energies as low as 100 mJ with the spherical lens.

Again, the next step in optimisation of the initial conditions was to calculate and plot the signal to standard deviation ratios in the laser-produced plasma. Figure 13 shows the SSDR data at the 3 most relevant spatial positions using the 150 mm cylindrical lens. In all cases, the laser pulse was focussed 1 mm below the target surface

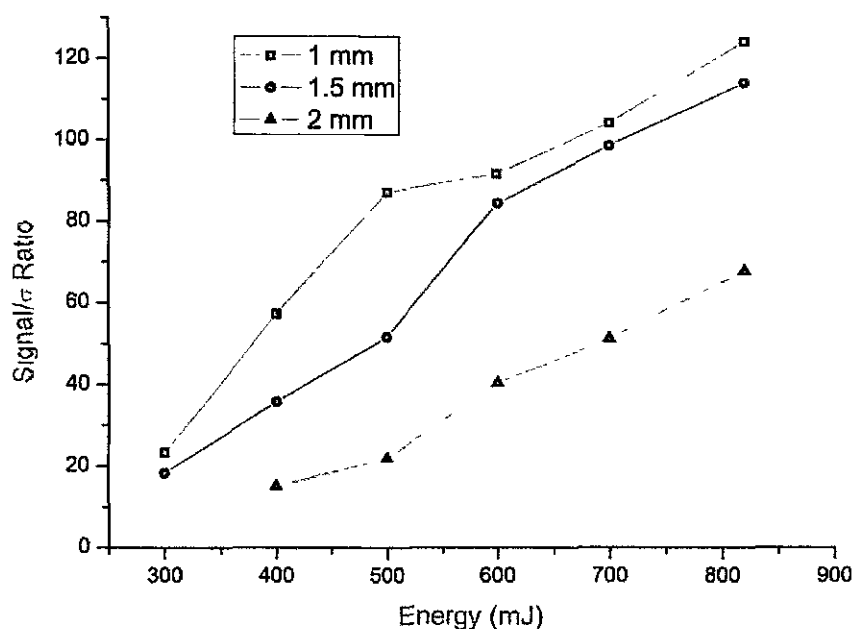


Figure 13 Signal to Standard Deviation Ratios for Varying Pulse Energies at 1, 1.5 and 2 mm
- 150 mm Cylindrical Lens

The SSSR values for the cylindrical lens are noticeably different than those obtained using the spherical lens. Instead of reaching a peak at 600 mJ, the values increase almost linearly up to 820 mJ (the maximum energy output of the laser). The values themselves were also low in comparison to those seen using the spherical lens, with the maximum value observed at 1 mm from the target surface using an 820 mJ laser pulse. It must be noted again that the fit quality of curves to the spectral data was lower when spectra were recorded closer to the target surface

These results clearly show that optimisation with the spherical lens was more successful and produced higher SSDR values than the results of optimised laser plasmas using the cylindrical lens - as such, the spherical lens is the better choice for the calibration experiments. Nevertheless, the next step in optimisation, varying the focusing conditions of the lens, was completed using both types of lenses in order both to show a clear difference between the characteristic plasmas produced by each and for the sake of a more complete vacuum study with each.

4.6 FOCUS VARIATION

An important consideration in producing the laser-produced plasmas was the focal condition the pulse was subjected to. The laser spot is quite easy to defocus and can be done in 2 different ways - forward and backward i.e. into and in front of the target. An example of each defocusing scheme is shown in Figure 14.

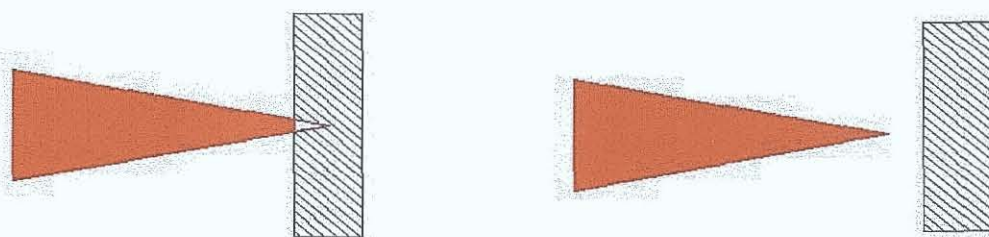


Figure 14: Positive (left) and Negative (right) Defocusing Schemes

As each lens is defocused (in steps of 1 mm each), the spot size changes thus affecting the power density on the target and electron temperature in the plasma. The size increase in the plasma as a result of the increased spot size was also a factor in changing the spectra observed in the plasma. Figure 15 below shows the effect of focus changes in the case of SSDR levels using the cylindrical lens. The data is calculated from spectra produced by accumulating 20 820 mJ laser pulses - the optimum energy from the previous step.

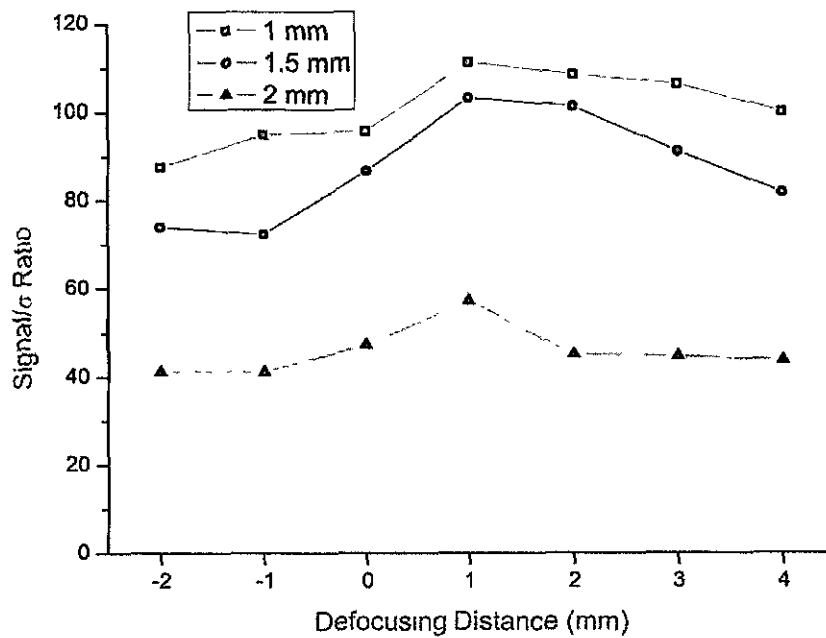


Figure 15 Signal to Background Ratios Under Varying Focal Conditions at 1, 1.5 and 2 mm - 150 mm Cylindrical Lens

The signal to standard deviation ratios are relatively flat and featureless when using the cylindrical lens - outside the presented focal range, the S^{4+} line intensity dropped significantly. The optimum defocusing regime is seen at 1 mm when the lens is defocused by 1 mm *into* the target surface. These results show no major improvements in the signal to background ratio from the previous study on pulse energy variation.

Varying plasma formation conditions using different focusing conditions using the spherical lens was the next step. Since the pulse energy was observed to be optimal at 600 mJ, all data was recorded using accumulations of 20 600 mJ laser shots. Figure 16 shows the result of this experiment.

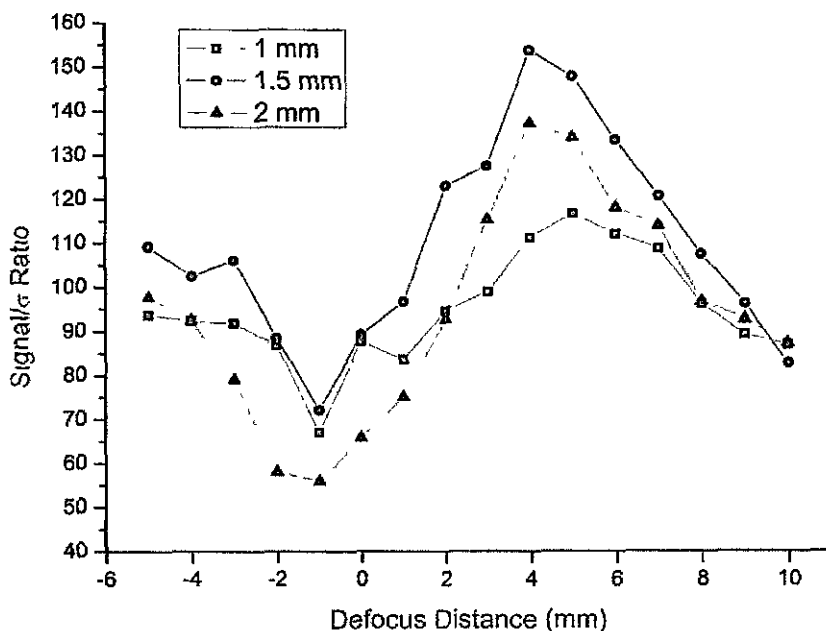


Figure 16 Signal to Background Ratios Under Varying Focal Conditions at 1, 1.5 and 2 mm - 100 mm Spherical Lens

Defocusing the spherical lens had a far more dramatic effect on the signal to background ratio than the cylindrical lens. Negative defocusing (focusing the laser pulse in front of the target surface) produced higher ratios than before but the most noticeable effect was seen by defocusing the pulse 4 mm below the target surface, with a steep rise up to the highest SDR yet. This is possibly due to the best balance struck between the high temperatures required to excite the sulphur atom into the 4th ionisation state and the increased number of sulphur ions in the plasma due to the larger target area illuminated by the laser pulse.

It is also interesting to note the sharp drop in the ratio when the laser is focused to just in front of the target surface. When considering this result, one must take into account the plasma absorption of the incident laser pulse. Since plasma expansion commences relatively early in the laser pulse (in the first few cycles of the pulse itself), it is reasonable to assume that throughout a large fraction of the laser pulse lifetime a dense plasma will lie in between the target and the incoming pulse. This plasma will affect both the laser pulse focusing and the fraction of laser light which reaches the target surface, due to the hottest and densest part of the plasma lying close to the target surface. The effect is less pronounced when the laser pulse is focused further out from the surface due to lower densities at these distances

4.7 SULPHUR CALIBRATION CURVES

With optimum conditions regarding pulse energy and focus found for both cylindrical and spherical lenses, the final step in this vacuum study was to record spectra under these optimised conditions from a carousel of targets with varying concentrations of sulphur (see chapter 3, section 3). In this case, the concentration range varied from targets containing 0.38% of sulphur down to targets containing as little as 0.0119% (119 ppm). For comparison, both lenses were used in this study despite the results obtained using the cylindrical lens being inferior to the spherical lens. This difference between the lenses is almost certainly due to the lower temperatures achievable by the cylindrical lens with the result that fewer of the higher ionisation stages in the relatively light sulphur atom were created. It must be noted that this result is similar to work performed in vacuum by Khater et al in 2000 where a slightly longer focal length lens was used but markedly different to that performed by the same author in ambient gas (Khater, 2002) where the author concludes that a cylindrical lens produced the optimum conditions for carbon calibration. The most successful carbon line used in those studies was from a doubly-ionised carbon atom - different to the quadruply-ionised sulphur atom in the present work.

The first calibration curve presented is that obtained using optimised conditions with the 150 mm cylindrical lens and is shown in Figure 17. The optimised conditions for the cylindrical lens were seen to be 20.820 mJ laser shots recorded 1 mm from the target surface with the cylindrical lens defocused by 1 mm into the target itself.

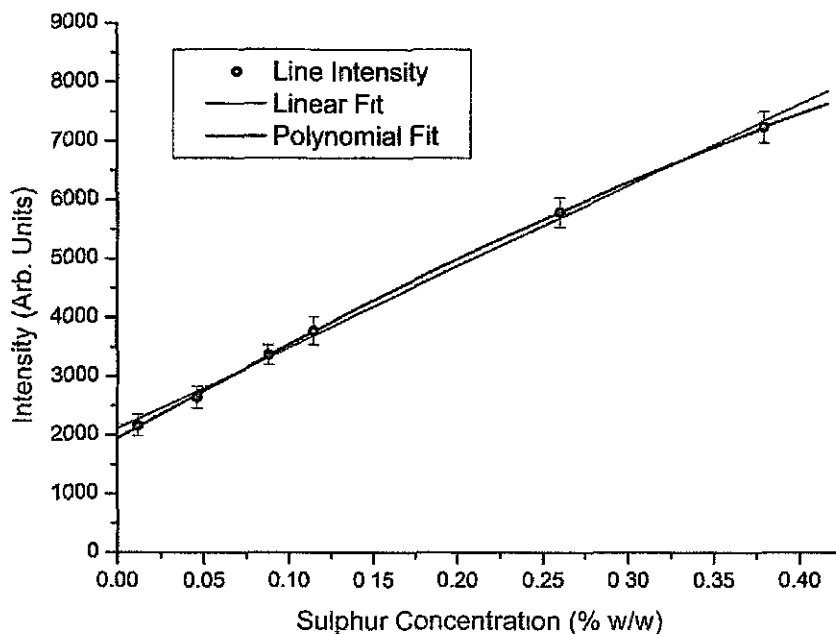


Figure 17 Calibration Curve - Cylindrical Lens
(820 mJ, 1 mm from the Target Surface, 1 mm Defocused)

Several features of the calibration curve must be noted. The intercept on the y-axis is quite high for a supposedly blank signal. This is quite possibly due to a change in the *linear dynamic range* of the calibration curve (Cremers & Radziemski, 2006). This essentially means that the emission characteristics of the analyte species change non-linearly in some concentration regimes. This effect was particularly evident in a calibration study made by St-Onge, Sabsabi & Cielo (1997) in concentration ranges of less than 1%. A previous study made by Khater et al. (2000) used the C^{2+} line at 97.7 nm to make this type of calibration with no serious non-linear effects and with the intercept of the line approaching zero. The difference between this study and that is the higher value of the absorption oscillator strength of the sulphur line in comparison, leading to increased absorption in the laser plasma with increasing number density. The R^2 coefficient (the coefficient of deviation) of the line fit was 0.994 which means that the fit was quite good - the data set was highly linear. Both second and third order polynomial fits were also used on the concentration data with the second order fit modelling the data as accurately as the linear fit. The second order line fit is shown on the calibration curve as well.

To calculate the Limit Of Detection (LOD) and Limit Of Quantification (LOQ) values, the standardised IUPAC (1978) definition states that in order to use the 3σ

criterion (Chapter 2, section 6) the background standard deviation must be calculated from the data recorded in the sample with the lowest concentration of analyte - in this case, the sample with the lowest concentration of sulphur contained 119 ppm. The slope of the line was calculated to be just under 13800 using the line fit equation - when coupled with a lower standard deviation in the 119 ppm sample of 18.62, this gives a LOD of about 42 ppm and a LOQ of 139 ppm - higher than the sample with the lowest concentration in the sample set. By definition, the data obtained for the target containing 119 ppm of sulphur must therefore be called into question as, by definition, the concentration is below that which can be accurately estimated

Table 2 Calculated vs. Actual Concentrations - Cylindrical Lens

Target	Actual Concentration	Calculated Concentration (From Calibration Curve)
BS 65C	0.115 ± 0.005 %	0.124 ± 0.008 %
BS 50E	0.0119 ± 0.0006 %	0.0113 ± 0.001 %
IARM 206A	0.26 ± 0.013 %	0.275 ± 0.012 %
BS 54D	0.046 ± 0.0012 %	0.040 ± 0.003 %
IMZ 123	0.38 ± 0.01 %	0.383 ± 0.014 %
BS 52D	0.088 ± 0.0015 %	0.094 ± 0.005 %

The average error in the data for the cylindrical lens was calculated to be about 7% leading to some calculated values of sulphur concentrations being outside the error range of the calibration curve

The second calibration curve presented (Figure 18) is that obtained using the spherical lens with 20 600 mJ pulses recorded 1.5 mm from the target surface and with the lens defocused by 4 mm into the target surface.

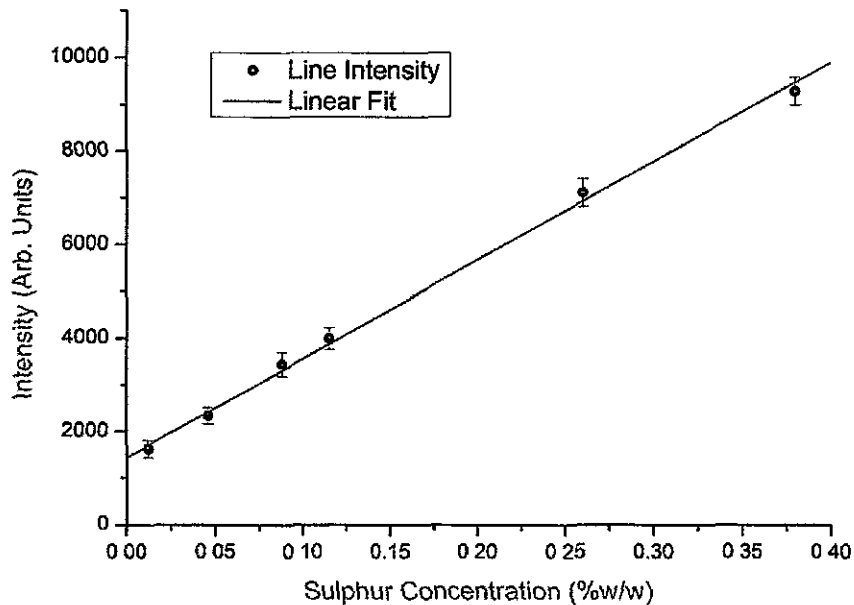


Figure 18 Calibration Curve - Spherical Lens
(600 mJ, 1.5 mm from the Target Surface, 4 mm Defocused)

The above plot has an R^2 coefficient (coefficient of deviation) of 0.998 meaning that a highly linear relationship exists between the data presented and the line fit, better than a linear fit overlaid on the data using the cylindrical lens. Both second and third order line fits were again used on the data, but neither proved to be as successful as the linear fit. One feature of the graph to note is that the line fit has been extended so that it reaches the y-axis of the graph - this means that an apparently zero concentration will result in a relatively high emission reading. This clearly is not the case - the behaviour of a lower range of sulphur concentrations will be examined in more detail in the following chapter. This apparent discrepancy can be attributed to non-linearity in the emission characteristics previously mentioned.

The standard deviation of the background signal was calculated to be just under 20 for this sample and with the slope of the line fit calculated to be just over 21100 (calculated by the line fit equation), this resulted in a LOD for the spherical lens of 28 ppm. The LOQ for the same set of samples was observed to be about 94 ppm. The following table (Table 3) shows the actual values vs the line fit values from the calibration curve for each of the targets used in the study.

Table 3: Calculated vs. Actual Concentrations - Spherical Lens

Target	Actual Concentration	Calculated Concentration (From Calibration Curve)
BS 65C	0.115 ± 0.005 %	0.121 ± 0.007 %
BS 50E	0.0119 ± 0.0006 %	0.0112 ± 0.001 %
C-1215	0.26 ± 0.013 %	0.264 ± 0.011 %
BS 54D	0.046 ± 0.0012 %	0.042 ± 0.003 %
IMZ 123	0.38 ± 0.01 %	0.371 ± 0.012 %
BS 52D	0.088 ± 0.0015 %	0.095 ± 0.007 %

The table shows an average 5% error in the precision of the data between calculated and actual sulphur concentrations in the target. These results show that optimised conditions using the spherical lens are both more sensitive and more accurate than similar studies using a cylindrical lens, a conclusion that had been discovered from the optimisation study performed previously.

4.8 SUMMARY

Optimised conditions for both line and point plasmas have been observed under vacuum conditions with a view to conducting target analysis using calibration curves. Limits of detection and quantification have both been calculated in these conditions, with the optimised conditions for point plasmas proving to be superior to line plasmas for low-level detection of sulphur in a steel matrix. The best result obtained using VUV space-resolved LIPS was calculated to be 28 ppm using optimised plasma ignition conditions with a spherical lens.

REFERENCES

- Colombant D & Tonon GF: "X-Ray Emission in Laser-Produced Plasmas", *Journal of Applied Physics*, **44**, pp 3524 - 3537 (1973).
- Cowan RD: *The Theory of Atomic Structure and Spectra*, University of California Press, 1981.
- Curd W et al: "The Solar Disk Spectrum between 660 and 1175 Angstroms (first order) Obtained by SUMER on SOHO", *Astronomy & Astrophysics*, **126**, pp 281 (1997).
- CXRO Matter Interaction Calculator
http://www-cxro.lbl.gov/optical_constants/gastrn2.html
- Cremers DA & Radziemski LJ: *Handbook of Laser-Induced Breakdown Spectroscopy*, Wiley, 2006
- Dunne P, O' Sullivan G & O' Reilly D: "Prepulse-Enhanced Narrow Bandwidth Soft X-Ray Emission from a Low Debris, Subnanosecond, Laser Plasma Source", *Applied Physics Letters*, **76**, pp. 34 - 36 (2000).
- Eliezer S: *The Interaction of High-Power Lasers with Plasmas*, Institute of Physics Publishing, 2002.
- Hirsch JS et al.: "Vacuum-Ultraviolet Resonant Photoabsorption Imaging of Laser Produced Plasmas", *Journal of Applied Physics*, **88**, pp. 4953 - 4960 (2000).
- IUPAC, Analytical Chemistry Division: "Nomenclature, Symbols, Units and their Usage in Spectrochemical Analysis - II. Data Interpretation", *Spectrochimica Acta Part B*, **33**, pp 241 - 245 (1978).
- Hemmerlin M et al: "Application of Vacuum Ultraviolet Laser-Induced Breakdown Spectrometry for Steel Analysis – Comparison with Spark-Optical Emission Spectrometry Figures of Merit", *Spectrochimica Acta Part B*, **56**, pp 661 - 669 (2001).
- Kelly RL: Kelly Atomic Line Database, <http://cfa-www.harvard.edu/amdata/ampdata/kelly/kelly.html>.
- Kurucz RL et al : Kurucz Atomic Line Database,
<http://cfa-www.harvard.edu/amdata/ampdata/kurucz23/sekur.html>, 1995 Atomic Line Data (R.L. Kurucz and B. Bell) Kurucz CD-ROM No. 23. Cambridge, Mass.: Smithsonian Astrophysical Observatory.
- Khater MA et al: "Time-Integrated Laser-Induced Plasma Spectroscopy in the Vacuum Ultraviolet for the Quantitative Elemental Characterization of Steel Alloys", *Journal of Physics D: Applied Physics*, **33**, pp. 2252 - 2262 (2000).
- Khater MA et al: "Optimization of the Emission Characteristics of Laser-Produced Steel Plasmas in the Vacuum Ultraviolet: Significant Improvements in Carbon Detection Limits", *Applied Spectroscopy*, **56**, pp. 970 - 983 (2002).

- Laming JM et al: "Electron Density Diagnostics for the Solar Upper Atmosphere from Spectra Obtained by SUMER/SOHO", *Astrophysical Journal*, **485**, pp. 911 (1997).
- Ralchenko Y et al.: "NIST Atomic Spectra Database v. 3.1.1 (Online)", <http://physics.nist.gov/asd3>, (2007).
- Radziemski LJ & Cremers DA. *Laser Induced Plasmas and Applications*, Dekker, 1989.
- St-Onge L, Sabsabi M & Cielo P: "Quantitative Analysis of Additives in Solid Zinc Alloys by Laser-Induced Plasma Spectroscopy", *Journal of Analytical Atomic Spectrometry*, **12**, pp 997 - 1004 (1997).
- Sturm V, Peter L & Noll R: "Steel Analysis with Laser-Induced Breakdown Spectrometry in the Vacuum Ultraviolet", *Applied Spectroscopy*, **54**, pp. 1275 - 1278 (2000)
- Winefordner JD et al.: "Comparing Several Atomic Spectrometric Methods to the Superstars: Special Emphasis on Laser Induced Breakdown Spectrometry, LIBS, A Future Superstar", *Journal of Analytical Atomic Spectrometry*, **19**, pp. 1061 (2004).

CHAPTER V: LIPS FOR DETECTION OF SULPHUR IN STEEL: AMBIENT ATMOSPHERES

In this chapter, details of experiments involving laser plasma expansion into ambient gases are given and a theoretical basis for the observed changes is outlined in the beginning. A full series of optimisation experiments were carried out with three different gases at different pressures in order to find the optimum signal to standard deviation ratio - the optimised parameters for conducting LIPS experiments. These experiments resulted in calibration curves obtained using a low concentration target set (27 ppm - 460 ppm) and a new low detection limit of 1.7 ppm achieved.

5.1 INTRODUCTION

The results of experiments in chapter 4 led on to the possibility of conducting LIPS experiments using an ambient gas as a buffer for the expanding plasma in order to improve the sulphur detection limit. LIPS in ambient atmospheres of various different gases has been performed extensively over the past number of years in order to make LIPS a more applicable spectroscopic technique in terms of industrial analysis in on-line and real-world applications (for examples, see Noll 2001, Radziemski 2005 and Latkoczy & Ghislain 2006). Not only is it a more natural circumstance in analytical terms when a laser-produced plasma expands into an ambient gas, but there are significant changes to both the appearance and characteristics of the laser plasma itself in comparison to expansion into vacuum. Although these differences were observed relatively early in the laser plasma timeline (Piepmeier & Osten, 1971), it wasn't until Geohegan's paper in 1992 that absolute differences were shown. This was made possible by the advent of fast gated ICCD cameras, which can capture 2D images with a very high shutter speed. Initial studies like this one were directed towards the effects of pressure changes in ambient atmospheres to aid superconductor growth via PLD, but the general dynamics of plasma plume expansion into gas is an interesting topic in itself. Further research into this area has been conducted extensively by Harilal amongst others in several publications (see Harilal 1998 & Harilal 2003) on the effect of the ambient gas on electron temperature & density and also the effect of changing gas pressures on spectral emission from the laser plasma itself. It has been observed in several publications (e.g. Khater 2002, Corsi 2003 and Radziemski 2005) that emission from the laser plasma is enhanced for many atomic species due to increased collisional excitation in the target/atmosphere plasma. Observations of ionic and neutral lines in the plasma plume from both the target and atmospheric species are sometimes used to measure electron densities and temperatures in the plasma plume (for example, see Amoruso et al., 1999).

The main difference between laser plasma expansion in vacuum and gas is that instead of free expansion of the plume, a shock wave can form in front of the expanding plasma as the ambient gas is compressed by the fast-moving particles at the front of the plume. According to Root (1990), there are three general regimes under which expansion into gases takes place, each of which refers to a different irradiance on the target surface: Laser-Supported Combustion (LSC) waves for low fluences, Laser-Supported Detonation (LSD) waves for intermediate fluences and Laser-Supported Radiation (LSR) waves for high fluences. All these waves describe

different mechanisms via which the laser pulse is absorbed by both the plasma and the ambient gas. When the laser pulse has ended, the expanding plasma then creates a shockwave in the gas which further heats it enough to cause ionisation. There are common attributes to each one of the profiles which can be described as follows.

5.2 THEORY

According to Root's (1990) treatment, when the laser plasma is formed (see Chapter II), the outer edge of the plasma is found to consist of fast-moving ions and electrons which start to collide with the ambient gas. Several zones then form along the laser pulse axis. They consist of the shock wave produced by the collision of the particles with the ambient gas, an absorption zone created by energy transfer initially from the expanding plasma and then from the laser pulse itself and lastly the main bulk of the plasma. The shock wave and absorption zone in front of the main plasma bulk travel along the laser pulse axis while the laser pulse remains "on" - both the shock wave and absorption zone can be considered to be a 1 dimensional travelling wave, while particles at the edge of the bulk plasma expand radially from the ignition point on the target surface. Figure 1 below shows a basic diagram of the plasma expansion into an ambient gas.

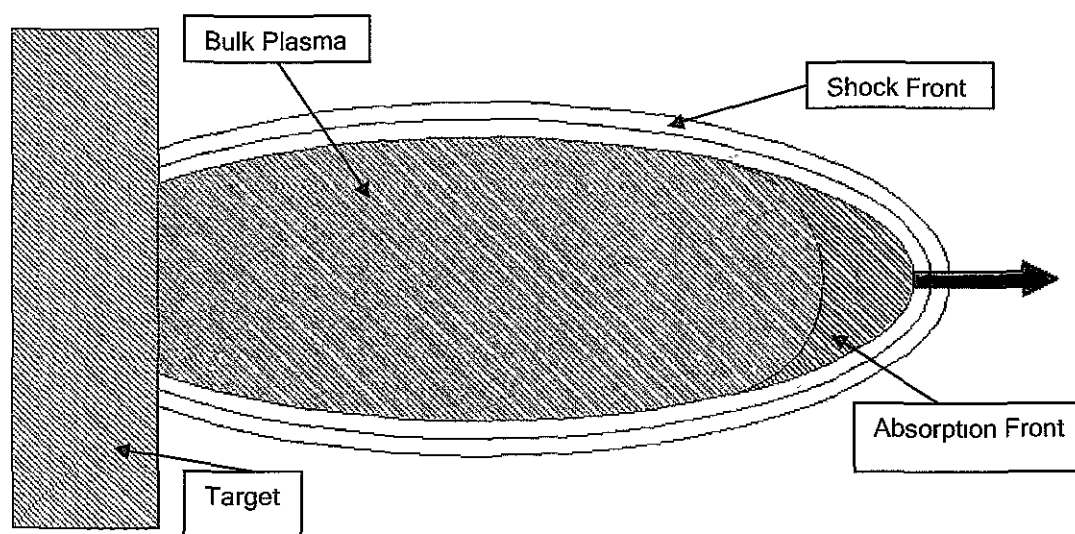


Figure 1 Plasma Expansion into an Ambient Gas

The following descriptions of each of the shock wave schemes are pressure dependent - although the main characteristics as described are more pronounced in relatively high pressures e.g. > 1 mBar, the expansion schemes are relevant to plasmas formed in gases with pressures as low as 10^{-2} mBar.

At low power densities of the order of 10 MW/cm^2 , the LSC wave absorption model is dominant. In this model, the shock wave precedes the absorption front and the bulk plasma. As the shock wave travels through the gas, the gas is "snowploughed" by the following plasma front with the result that the gas is left at a higher pressure than before after passage of the shock wave. This relatively high pressure gas remains optically thin with regards to the laser pulse but the neutral species in this region strongly absorb the high energy VUV and EUV photons produced by the plasma, resulting in photoionisation of the neutral species. The laser absorption coefficient rises proportionally to the square of the pressure in this area, which also increases the absorption rate of VUV and EUV radiation from the plasma. As more and more high energy photons are absorbed by the neutral species, the density increases until the critical density is reached and the plasma in this region is completely coupled to the laser wavelength. The snowplough effect continues in front of the LSC wave as it grows, leading to a continuous source of high pressure gas for the growth of the absorption region. Both plasma radiation and the pressure change caused by the shock wave expansion are necessary to propagate the absorption front along the direction of the laser pulse. By this mechanism, a new absorption front has been created in front of the expanding plasma which continues until the cessation of the laser pulse.

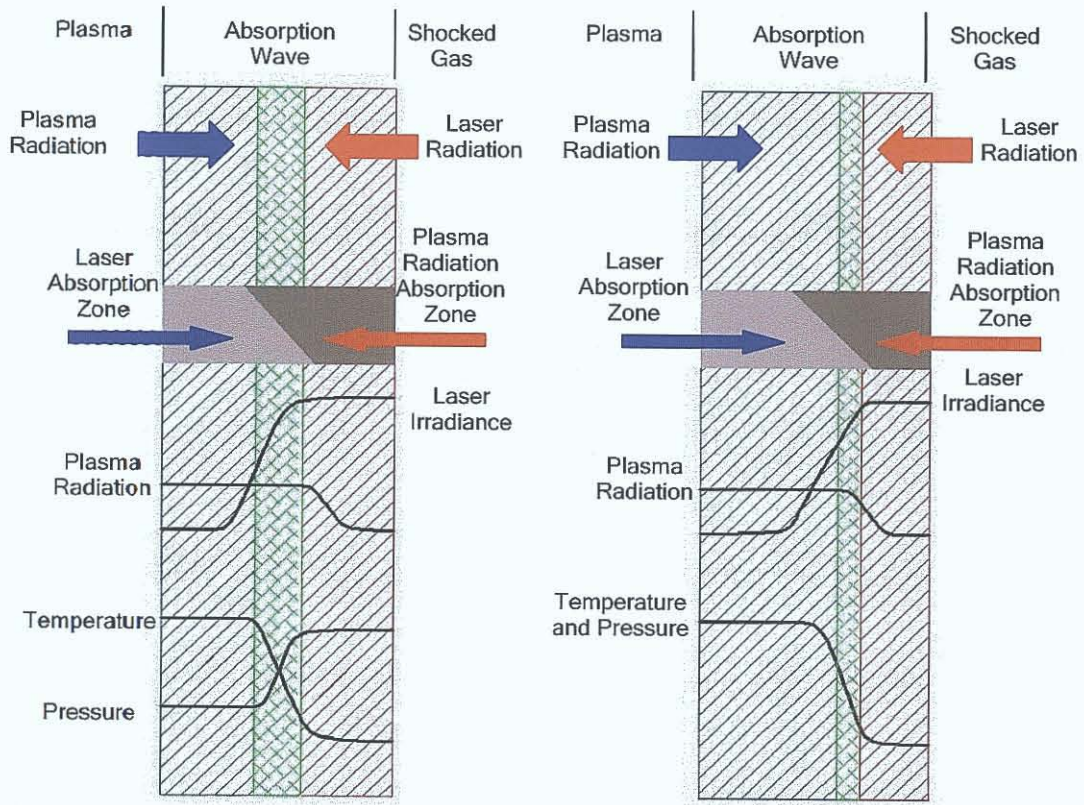
When power densities are of the order of $10 \text{ MW/cm}^2 - 1 \text{ GW/cm}^2$, the shock wave is energetic enough to heat the ambient gas as it passes through it to such a degree that energy transport from the plasma is not required for increased laser pulse absorption. This profile is called a detonation wave as it is analogous to a chemical detonation in a similar way to a chemically-generated shock wave heating the atmosphere as it propagates through it. In this LSD wave scheme, the absorption zone is coupled directly to the trailing edge of the shock wave in this case, as the shock region absorbs the laser pulse directly between the shock front and a point known as the *Chapman-Jouguet* point. The CJ condition (Yinon, 1993) states that a detonation wave proceeds at a velocity at which ambient gases just reach sonic velocity as the wave passes. The propagation of the absorption front is completely controlled by the absorption of the laser beam between the shock front and the CJ point. The laser pulse absorption continues in the high pressure region again until the

critical density is reached again and the plasma becomes optically thick at the laser wavelength.

At the highest power densities of more than 1 GW/cm^2 , a different mechanism is dominant. At very high power densities, the radiation flux from the plasma is so large that before a shock wave is incident on the gas in front of the expanding plasma, photoionisation of the gas in front of the expanding plume results in the absorption coefficient of the plasma increasing rapidly to the point where it becomes optically thick without the need for any energy transport from a shock wave. This plasma is characteristically very hot, and is a strong source of short wavelength radiation. The LSR model results in supersonic expansion of the absorption wave as the main constriction is the emission of radiation from excited species and absorption by species in the atmosphere in front of the hot area, not the speed of sound dominated shock wave. In terms of the energies and power densities used, the LSR scheme seems most relevant to the high power densities ($> 10^{10} \text{ W/cm}^2$) used in the experiments described hereafter, although without accurate VUV diagnostics in both the spatial and temporal dimensions this assertion remains unverifiable.

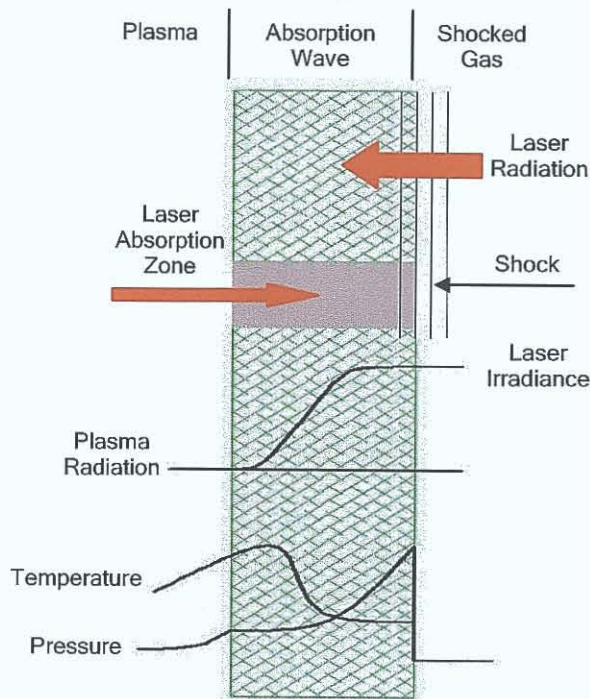
Figure 2 on the next page (after Root 1989) shows a qualitative description of each of the three main types of shock waves produced in an ambient gas by a laser-produced plasma plume

A summary of these three types of expansion would be that the LSC scheme produces a hot, slow moving wave which is an efficient method of converting incident laser radiation into broadband radiation. The LSD scheme results in high-density absorption zones which propagate into the ambient atmosphere at the shock wave velocity rather than being reliant on the speed of advance of the plasma front. The LSR scheme provides the fastest moving shock wave of the three. It is characterised by the creation of a very hot gas plasma in advance of the target plume that emits short wavelength radiation. Again, all of these expansion and shock wave formation schemes are pressure dependent, but can be assumed relevant down to pressures as low as 10^{-2} mBar (Root, 1989, Geohegan, 1992).



A) LSC Wave

B) LSR Wave



C) LSD Wave

Figure 2: Qualitative Comparison of 1-D Laser Absorption Waves - A) LSC Wave, B) LSR Wave, C) LSD Wave (After Root 1989)

In all cases, the gas in front of the expanding laser plasma plume is divided into a region before passage of the shock wave where the ambient atmosphere is unperturbed and a region after passage which is left in a higher energy state than before with higher temperatures and pressures. After cessation of the laser pulse, a shock wave passes through the ambient gas resulting in further heating of the atmosphere in front of the expanding plasma plume. This creates a secondary plasma through heating by the shock wave and impact ionisation from both high energy electrons and ions from the primary plasma (Kagawa, 1994). This plasma has a number of features that make it ideal for spectral analysis. Since the energy transport mechanism is now dominantly collisional through impact excitation and ionisation rather than radiative through inverse Bremsstrahlung, continuum radiation from this secondary plasma is greatly reduced. This means that since line intensities remain reasonably high compared to vacuum expansion, the signal to standard deviation ratios obtainable in an ambient gas should be higher.

The structure inside the plume as it expands has been shown to be complex and variant in several different ambient pressure regimes (Harilal, 2003) with a crossover from interpenetration at pressures below 10^{-1} mBar to a gas/plasma interface forming at pressures above 1 mBar. Both Geohegan and Harilal have both stated that there is a noticeable split in emission regions at this crossover pressure. Two emission components form: a stationary emission component near the target surface and a fast moving breakaway component which expands into the gas and has a clearly defined emission front. Splitting has been observed in the breakaway component of the plasma plume by a number of authors (Park, 1998 and Wood, 1998) - this phenomenon is where the breakaway component seemingly splits in two after interaction with the gas due to collisions with the gas. This is only observed around a pressure range centred on 0.2 mBar where the plasma/gas interpenetration is at its highest.

5.3 EXPERIMENT AND INITIAL SPECTRA

The experiment was configured in the same way as the initial vacuum studies with the main difference being that after the target chamber had been pumped down to its ultimate pressure (in the order of 10^{-6} mBar), a gas was allowed into the chamber by means of a needle valve - a valve with a very fine control of gas flow into

the target chamber. Figure 3 on the following page again shows the experimental configuration.

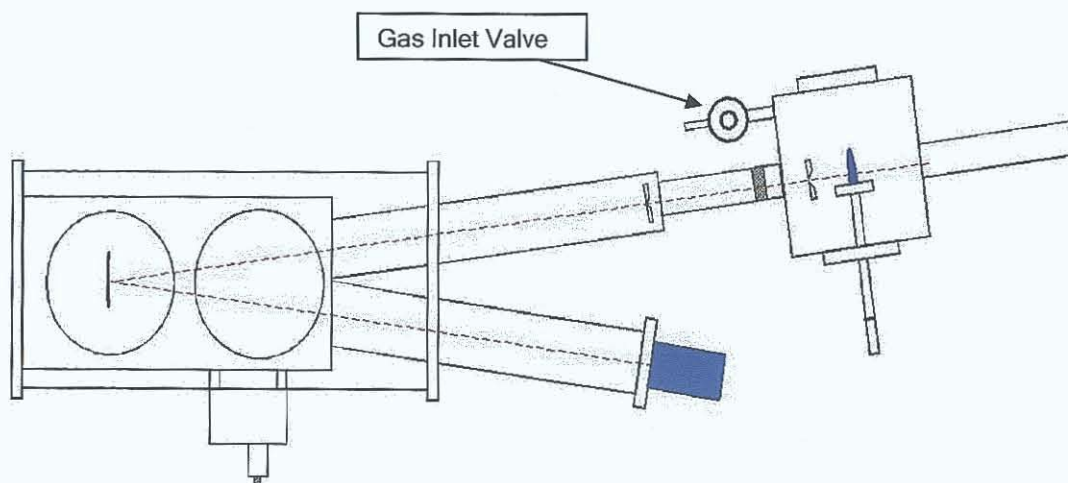
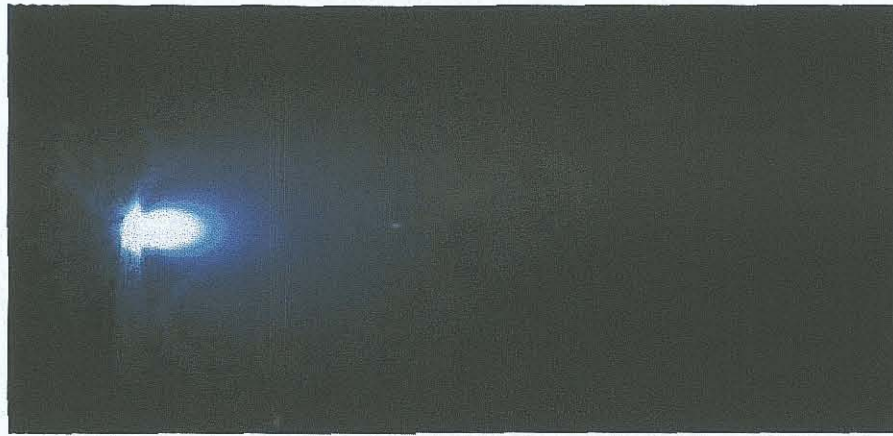


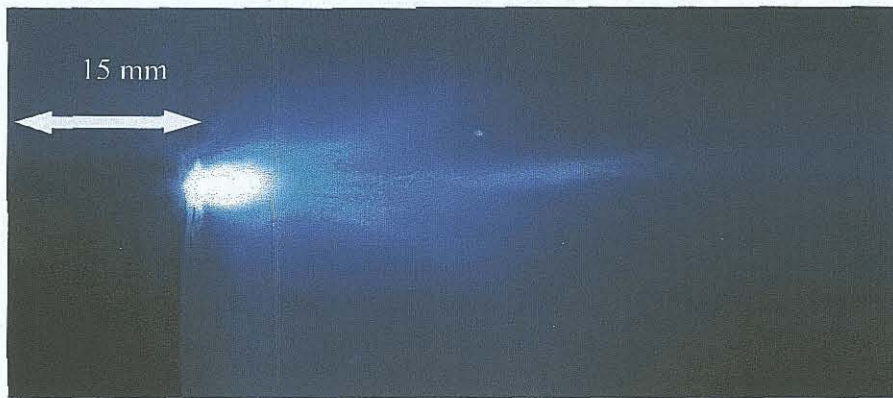
Figure 3: Experimental Configuration

Initial pumping to vacuum of the target chamber ensured that contributions to spectra from gases other than those intended in the target chamber were minimal - most experiments were performed in pressures of 10^{-1} mBar or more, so the percentage contribution of the chamber gas was less than .01%. Pressure was easily controlled in this chamber by fine tuning the needle valve at the chamber and monitoring the pressures of the various different gases in the chamber with an adjustable Pirani gauge. Since the Pirani gauge measures pressure by heat loss through the thermal conduction properties of different gases, different conduction constants in the gauge were required for pressure measurement in different gases. Pre-loaded constants were available for nitrogen, argon and helium with air being approximated to nitrogen.

All spectra in this chapter were generated with a 100 mm spherical lens due to its superior performance in comparison with the cylindrical lens used in chapter 4. The first noticeable change in the plasma was the visual increase in the intensity of radiation from the plasma. Figure 4 below shows the visual signatures of laser plasmas created in vacuum and 0.1 mBar of Nitrogen respectively.



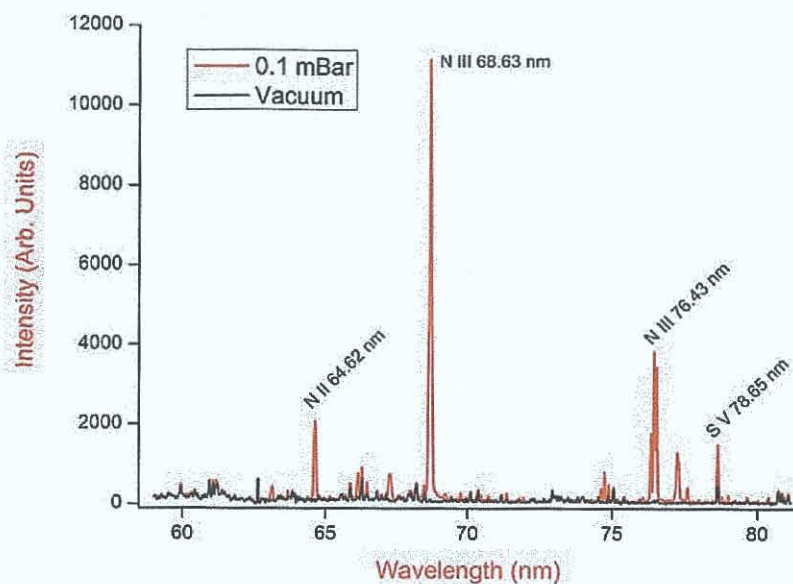
A) Vacuum



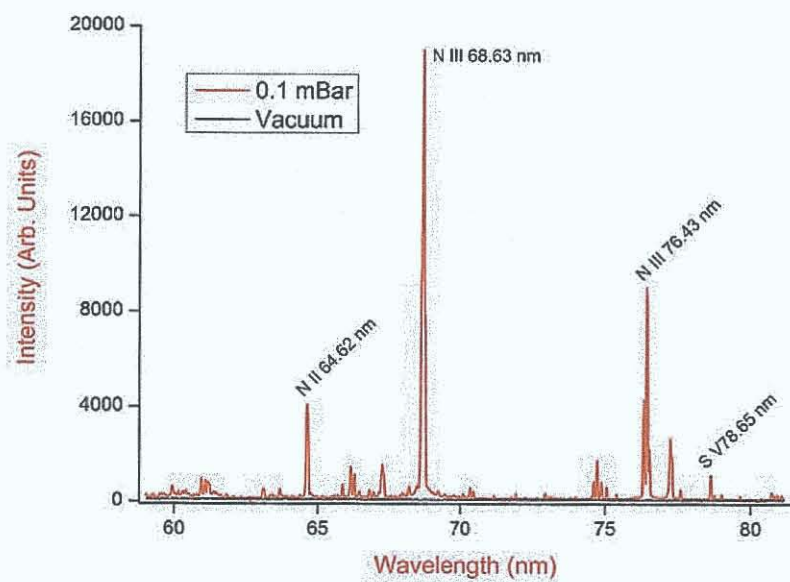
B) Low Pressure (0.1 mBar) Nitrogen

Figure 4: Laser Plasma Expansion into A) Vacuum and B) Low Pressure Nitrogen

Both plasmas were created using an 820 mJ laser pulse focused 3 mm below the target surface, with the images captured by a digital SLR camera using identical, manually set exposure and aperture settings. The target was the same binary target used in the studies in vacuum i.e. the target contained 0.68% of sulphur, with the rest iron. It can be readily seen that the plasma plume extends further into space in gas than in vacuum and that there is a larger amount of "detail" further into the gas - these emission features were observed during all experiments. Test spectra were taken at both 2 and 5 mm from the target surface in vacuum and a 0.1 mBar nitrogen atmosphere to see if there were any obvious changes in the spectral characteristics of the laser-produced plasma. These spectra are shown in Figure 5.



A) 2 mm

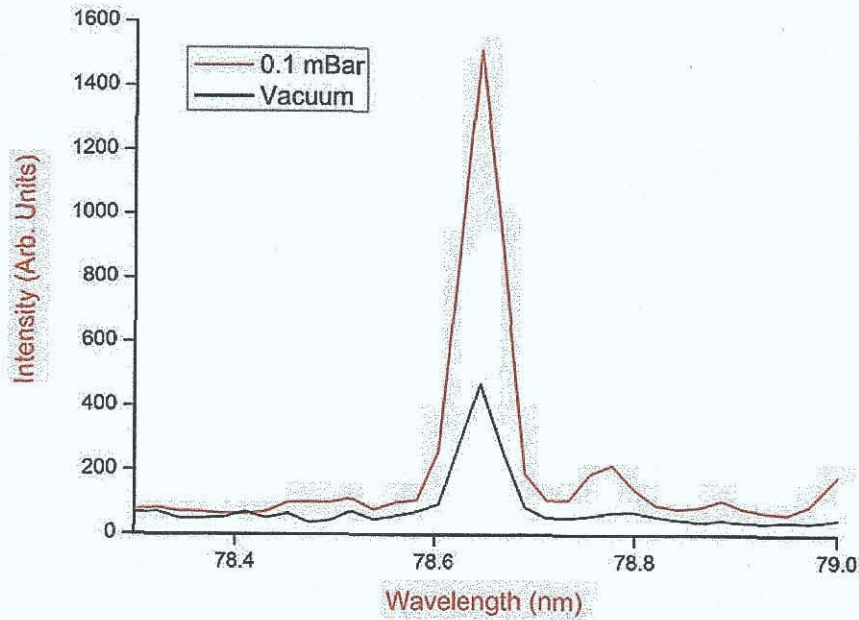


B) 5 mm

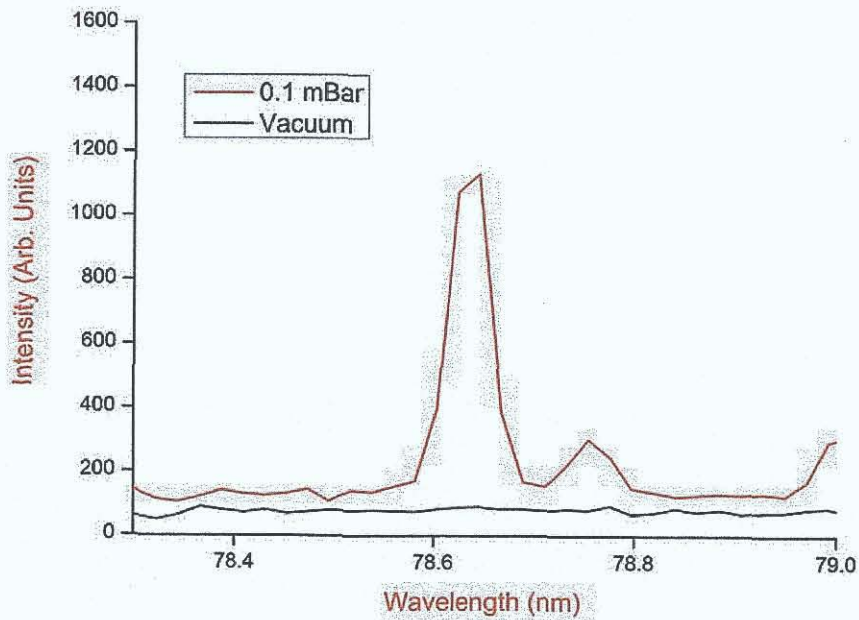
Figure 5: Test Spectra at A) 2 mm and B) 5 mm

As is immediately obvious, there are large differences between vacuum and gas spectra. The most obvious feature of this new spectrum is the N^{2+} line at 68.6 nm, with several other nitrogen lines at 64.5 and 76.5 nm evident. The main interest in the spectra is the S^{4+} line at 78.65 nm used in the previous vacuum study as a

calibration line. Figure 6 shows the change in this line's intensity from data taken in the spectra featured in Figure 5.



A) 2 mm



B) 5 mm

Figure 6: Varying S^{4+} Intensity at A) 2 mm and B) 5 mm

The S^{4+} line increases in intensity by almost a factor of 4 at 2 mm under 0.1 mBar of nitrogen and remains visible further out into the plume compared to the vacuum intensity. The background of the spectra was also reduced to less than half its value under vacuum conditions, with the fading of a significant number of iron lines. This is effectively due to the distance from the hot core of the plasma where continuum emission provides a largely decreased contribution to the radiation emission. With these factors in mind, sulphur lines in the region were again compared to find the best candidate for optimisation studies. The spectra themselves were recorded in 0.1 mBar of nitrogen at 2 mm from the target surface by accumulating 20 820 mJ laser shots which were defocused by 3 mm into the target. The results are shown in Table 1 below.

Table 1: Line Comparison (Ambient Gas Spectra)

Line (nm)	Peak Height (Arb. Units)	Peak Area (Arb. Units)	R ² Value
S^{3+} 66.14	1250.94	58.86	0.972
S^{3+} 74.84	895.15	39.99	0.997
S^{3+} 75.03	377.98	13.56	0.997
S^{4+} 78.65	1758.42	73.03	0.997
S^{5+} 93.34	1196.16	49.06	0.989
S^{2+} 100.62	751.28	31.8	0.988

As with the spectra taken in vacuum, the S^{4+} line is still markedly better than the other lines tested. It also provides a highly satisfactory R² value, meaning that the Gaussian fit of the line profile was accurate to a high degree. The region from 40 - 160 nm was examined for sulphur lines but produced no additional lines of satisfactory intensity on which to base optimisation studies. On this basis, experiments were aimed at improving the S^{4+} line's signal to standard deviation ratio (see chapter 4) by means of varying gas type & pressure, laser energy and focal distance. The first parameters investigated were gas type and pressure

5.4 BEHAVIOUR IN AMBIENT GASES

Laser plasma emission was first studied using the changeable parameters of type of gas, gas pressure and spatial distance from the target surface in order to assess the change in line intensity and signal to standard deviation ratio. Three gases were used in the study: argon, nitrogen and air. The absorption characteristics of each gas at different pressures are shown in Figure 7. The transmission coefficients of each of the gases was calculated using the CXRO Matter Interaction Calculator (ref. CXRO) using a 12 cm path length (the distance from the plasma to the GCA), a temperature of 297 K (lab temperature) and a wavelength of 78.65 nm with the pressure variable for each gas.

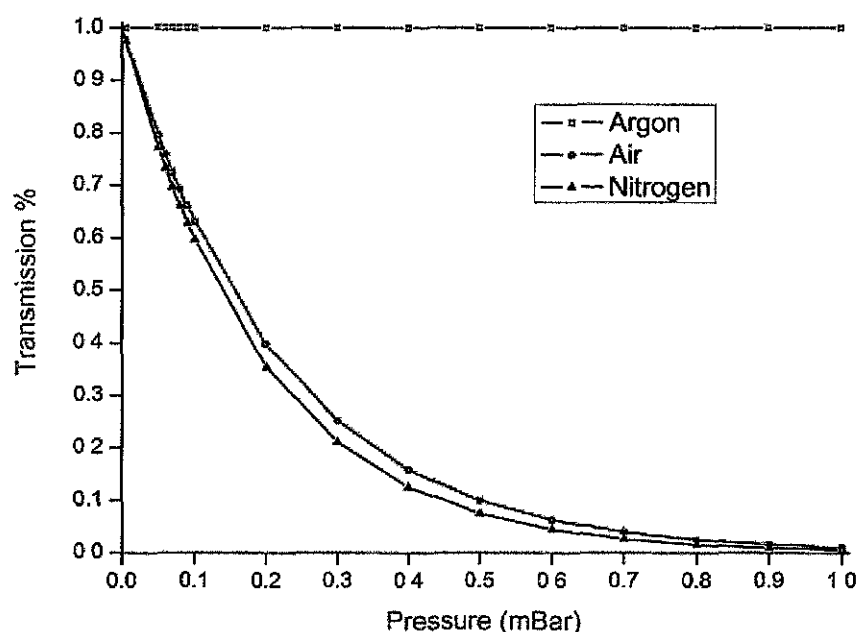


Figure 7: Gas Transmission Curves at 78.65 nm for Argon (red), Air (green) and Nitrogen (blue) - 12 cm Path Length

From Figure 7, one would assume that the line intensity would be greatest from the laser plasmas created in an argon atmosphere due to the fact that it is perfectly transmitting at 78.65 nm - this, however, was not the case. In the following 3 figures (Figures 8 - 10) the sulphur line emission in the 3 different tested gases is shown. The spectra are an average of 3 separate accumulations of 20 820 mJ laser shots each taken 4.5 mm from the target surface with the laser beam defocused by 3 mm - this is a selection from a substantial number of spectra taken in the course of

these experiments. It is interesting to note in these transmission curves that the emission intensity of the 78.65 nm line in vacuum for all gases is practically zero at this distance, while as the gas pressure increases it increases to a peak and drops off afterwards as the pressure approaches 1 mBar in nitrogen and air - the peak is seen at a lower pressure in argon.

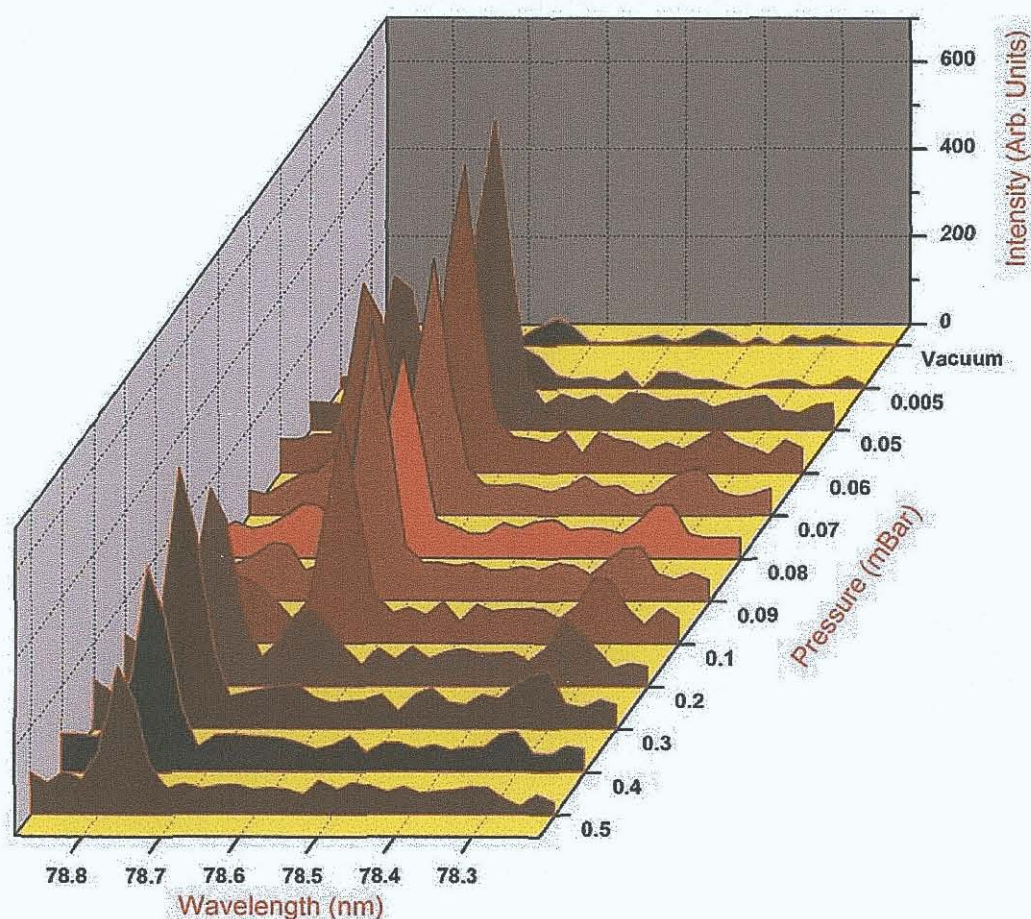


Figure 8: Argon Spectra - 4.5 mm from Target Surface, 20 x 820 mJ Laser Pulses Defocused 3 mm into the Target

Laser plasmas expanding into argon result in different behaviour of the S V line than both air and nitrogen. In Figure 8, the peak emission of the S⁴⁺ line was observed in argon was at a pressure of 0.06 mBar, with a relatively sharp drop in emission as the pressure exceeded 0.1 mBar. In pressures below 0.05 mBar, there was little or no sulphur emission observed due to the distance from the target surface - a result that coincides with those results presented in chapter 4 where emission from the S⁴⁺ line appeared to cease after about 3.5 mm from the target surface.

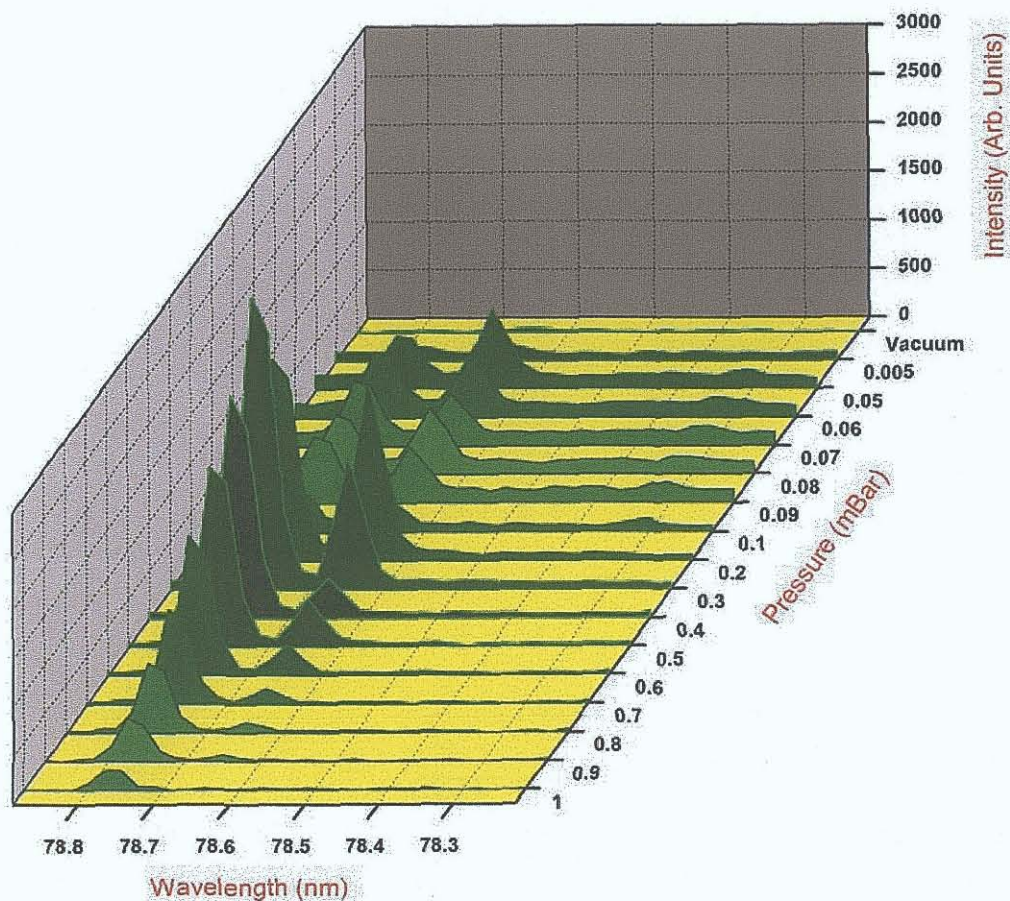


Figure 9: Air Spectra - 4.5 mm from the Target Surface, 20 x 820 mJ Laser Pulses Defocused 3 mm into the Target

In Figure 9, we can see that the air spectrum is quite different to that seen when argon is used as the ambient gas under the same laser energy and focus conditions. Again, there is little or no emission observed in ambient pressures below 0.05 mBar, while the line emission gets bigger above this. There is a dramatic jump in the emission at a pressure above 0.1 mBar, with the peak line emission recorded at 0.2 mBar. At pressures above this value, the emission steadily decreases until it is irresolvable at a pressure of about 0.7 mBar i.e. an accurate Gaussian fit of the line ($R^2 > 0.9$) could not be made.

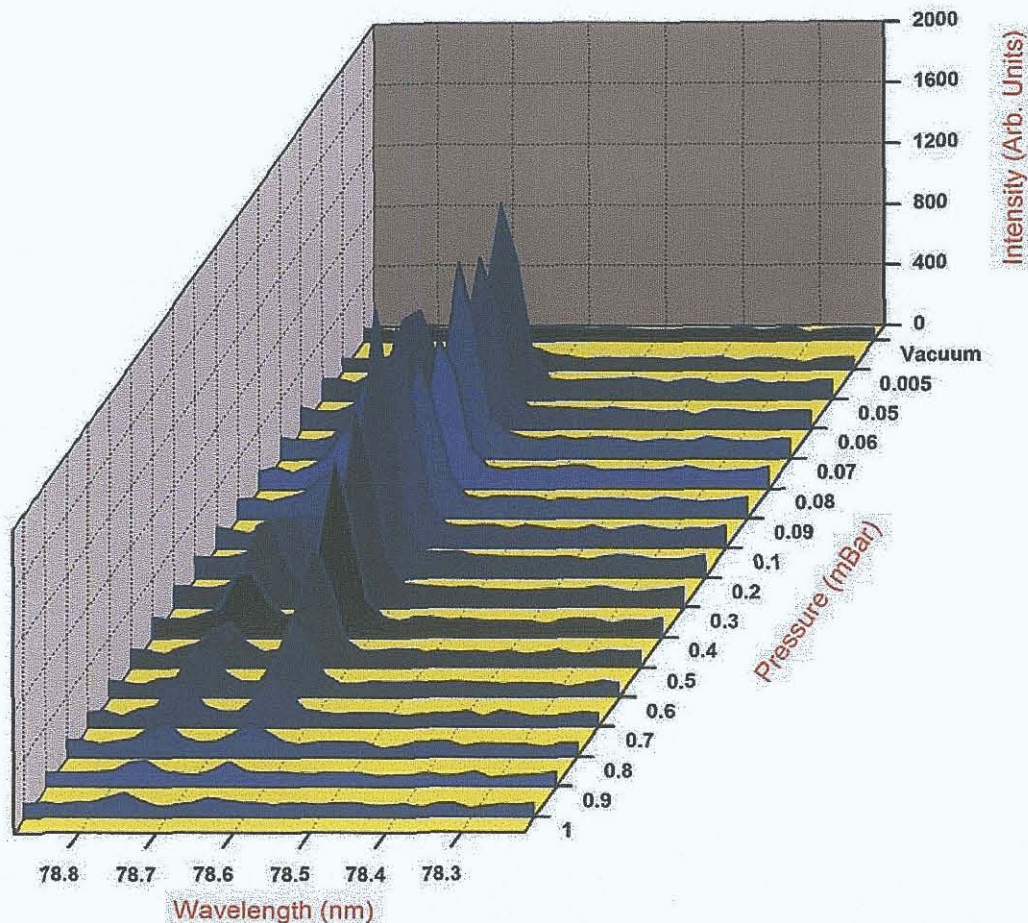


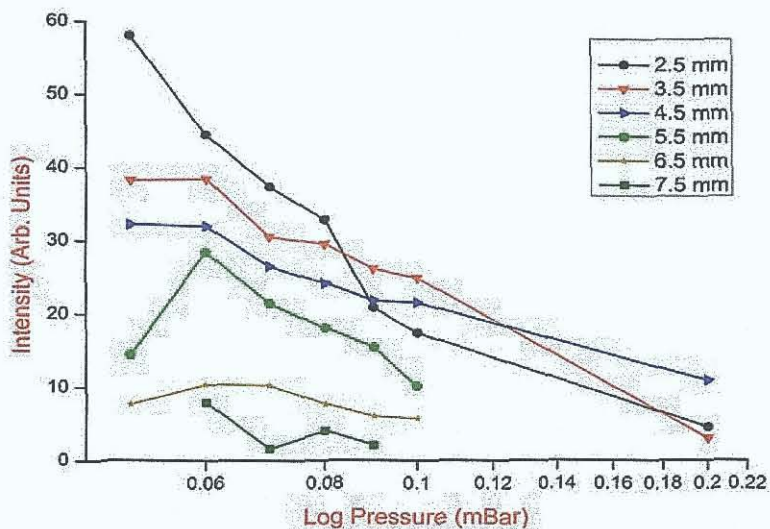
Figure 10: Nitrogen Spectra - 4.5 mm from Target Surface, 20 x 820 mJ Laser Pulses
Defocused 3 mm into the Target

Figure 10 shows the spectra observed in a nitrogen atmosphere. The behaviour of the S^{4+} line in nitrogen is similar to that seen in air, with the exception that the peak emission is about 25% greater than that seen in air. The peak emission was observed at a pressure of 0.2 mBar with the line remaining resolvable up to a pressure of 0.9 mBar - a greater pressure than that observed in air.

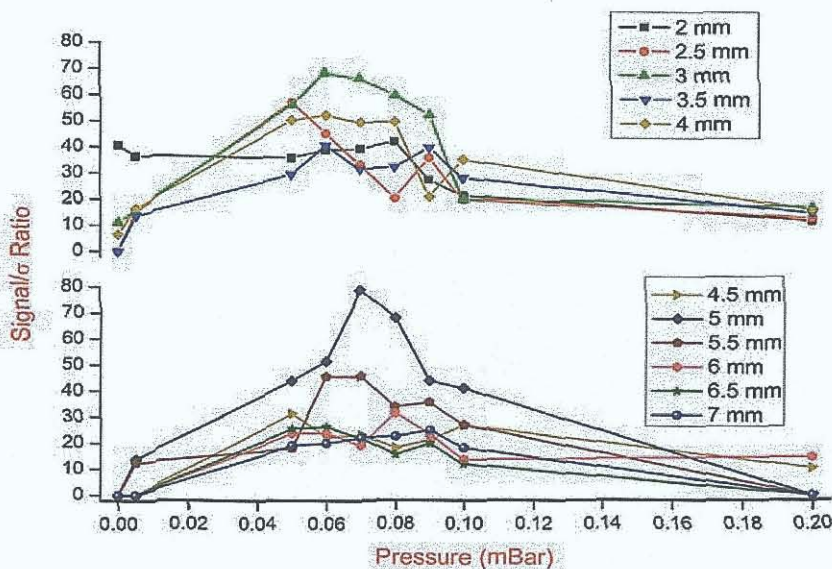
Both air and nitrogen produced peak emission values at 0.2 mBar - a pressure at which the percentage of transmitted radiation from the S^{4+} line was supposed to be just less than 40% for both. There was also a supplementary difference between air and nitrogen - the emission intensity from the line in air was about 20% less than at the same pressure in nitrogen, ostensibly due to oxygen absorption bands in the VUV.

For an analysis of line intensity behaviour, the most relevant approach was to graph the ratio of intensity to the standard deviation of a blank part of the spectrum

chosen to represent the background intensity in each spectrum. The "blank" standard deviation was found using the standard deviation from 2 line-free areas in each spectrum i.e. data points from 2 separate areas in the spectrum were used to calculate the standard deviation in the background. This value was then averaged over 3 separate spectra under the same conditions. These plots are combined with a sample of raw line intensities in order to show the stark differences in the relationship between the raw line intensity changes and the intensity to standard deviation ratio.



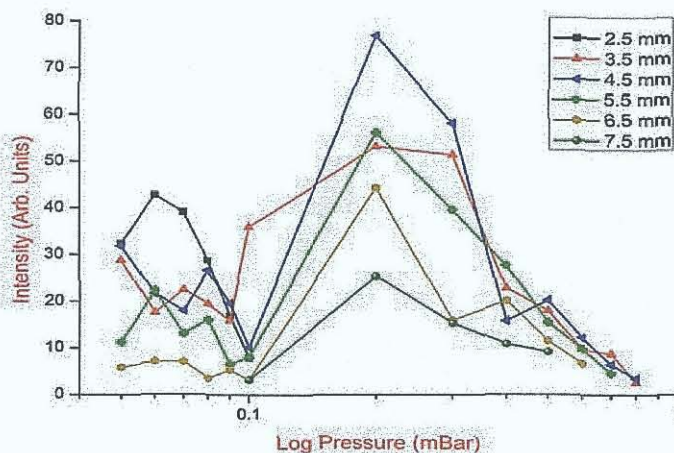
A) Argon - Raw Line Intensities with Varying Spatial Distance and Pressure



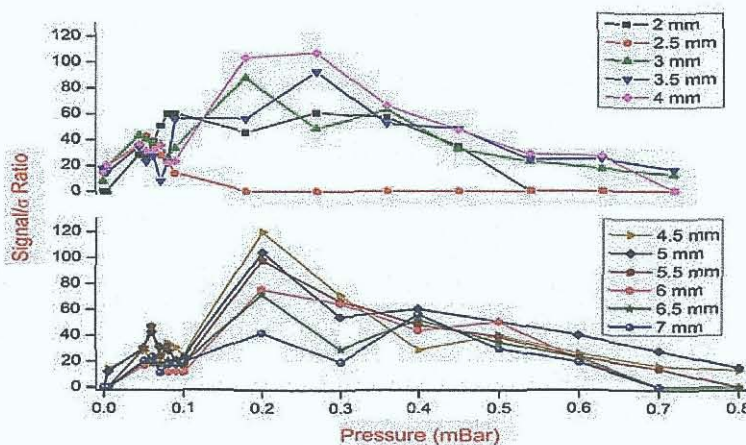
B) Argon - Signal/σ Ratios with Varying Spatial Distance

Figure 11: A) Raw Line Intensities and B) Signal/σ Ratios for S V (78.65 nm) in Varying Argon Pressures and at Varying Target Distances

In Figure 11A & B on the previous page both the raw line intensity and the line intensity vs. standard deviation ratio are plotted. The raw line intensity ratio seems to show that the best intensities were observed near the target surface with high line intensities observed close to the target surface. This high intensity decreased as the distance from the target surface increased - also, the intensity decreased as the argon pressure in the target chamber increased. When the ratio of the standard deviation in the background is calculated and the ratio between the line intensity and the standard deviation is used, the greatest values are seen at 5 mm from the target surface in 0.07 mBar of argon. There is a general increase in emission at all distances in Figure 11B between pressures of 0.05 mBar and 0.09 mBar, with a drop off above this pressure - indeed, the 78.65 nm line was no longer resolvable above 0.2 mBar.



A) Air - Raw Line Intensities with Varying Spatial Distance and Pressure



B) Air - Signal/σ Ratios with Varying Spatial Distance

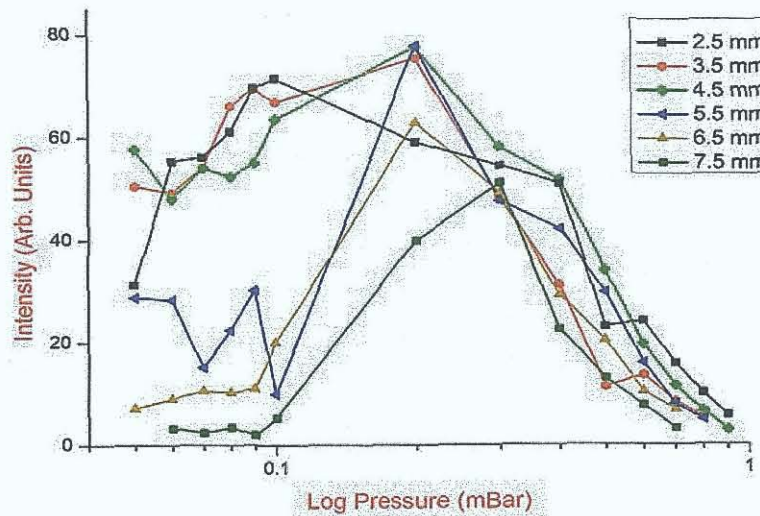
Figure 12: A) Raw Line Intensities and B) Signal/σ Ratios for S V (78.65 nm) in Varying Air Pressures and at Varying Target Distances

Figure 12 on the previous page shows identical plots for data recorded in an air atmosphere under the same conditions - 3 sets of 20 820 mJ shots were recorded at varying pressures and varying distances from the target surface. These results were averaged and plotted both on their own and as a ratio of the intensity to the standard deviation in the background signal.

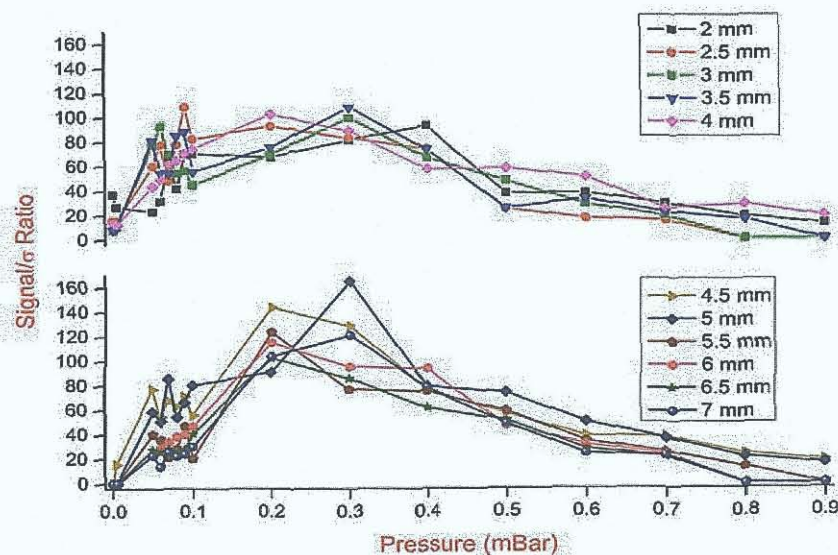
When the unmodified line intensities are viewed, it can be seen that they behave in a manner quite different to those recorded in an argon atmosphere. Although there seems to be a peak in line intensities near the target surface at pressures under 0.1 mBar, at 0.1 mBar the intensities at all distances seem to drop. At pressures just above this, line intensities peak dramatically at 0.2 mBar at distances over 3 mm, all the way out to 7 mm. The line can be seen at most distances up to a pressure of 0.7 mBar with reasonable intensity.

The signal to standard deviation ratios again change the nature of the plot - using this ratio, the fairly large line intensities near the target surface are discarded due to the ratio being low. A definite peak in the SDR can be seen at 0.2 mBar with the highest value recorded at 4.5 mm from the target surface. Ratios were high at distances close to the optimum distance i.e. from 4 mm to 5.5 mm with a similar trend in the decreasing intensity up to a pressure of about 0.7 mBar.

The final stage in optimising the atmospheric conditions was to perform the same experiments in a nitrogen atmosphere. Nitrogen was chosen in order to see if there were any differences between it and air and also because of its role in steel manufacturing (see chapter 1). The laser pulse parameters were again 20 820 mJ shots, 3 sets of which were recorded in order to average line intensities from the spectra.



A) Nitrogen - Raw Line Intensities with Varying Spatial Distance and Pressure

B) Air - Signal/ σ Ratios with Varying Spatial DistanceFigure 13: A) Raw Line Intensities and B) Signal/ σ Ratios for S V (78.65 nm) in Varying Nitrogen Pressures and Varying Target Distances

The behaviour of the S^{4+} line in a nitrogen atmosphere is quite similar to that seen in air. At pressures under 0.1 mBar, the raw line intensities are quite high at distances up to 4.5 mm. at greater distances from the target surface, the line intensities drop significantly. However, at all distances from the target surface the line intensities seem to peak at 0.2 mBar with a steady drop thereafter. The S^{4+} line was

visible in pressures up to about 0.8 mBar at nearly all distances from the target surface up until a maximum distance of 7.5 mm from the surface.

When the standard deviation was calculated and the line intensity to standard deviation ratio plotted, the graph shows a clear trend from the spectra. In the raw data, the line intensities were quite high at distances close to the target surface. When the signal was high near the target surface at pressures under 0.1 mBar, the standard deviation in the background was also large - this reduced the SDR to low values. At pressures of 0.1 mBar and above, the large peak seen in air is even more pronounced. The maximum value was recorded 5 mm from the target surface in 0.3 mBar of nitrogen although most of the maximum intensities were seen at 0.2 mBar for other distances from the target surface. Again, there is a steady decline in values up to a pressure of 0.8 or 0.9 mBar where the line becomes indistinguishable from the background.

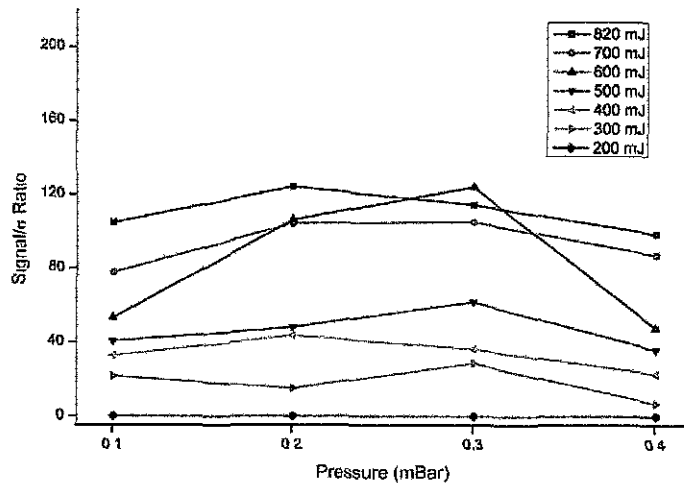
From data collected on the S^{4+} line behaviour in the ambient gases, it was observed that nitrogen produced the highest signal to standard deviation ratios. At 5 mm from the target surface at a pressure of 0.3 mBar, the highest signal to standard deviation ratio was observed before any optimisation of the laser pulse was made. The next step in optimisation of the spectral line was optimisation of the laser pulse in terms of energy and focus.

5.5 LASER PULSE OPTIMISATION

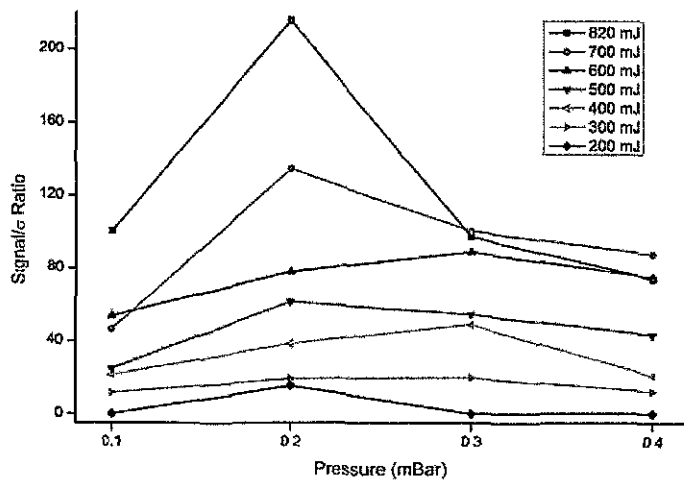
With the atmospheric conditions in the laser plasma generally optimised for maximum signal to standard deviation values in the laser plasma, the next stage in optimisation of the SDR was to vary the laser pulse both in terms of energy and in terms of power density on the target surface. This involved both modifying the initial laser pulse energy of the laser and changing the focal characteristics of the pulse on the target by movement of the 100 mm spherical lens, as was performed in the initial optimisation study conducted under vacuum. Since an increase was seen in a reasonably narrow range of conditions, the logical course was to perform the energy study for a wider range of spatial and atmospheric parameters relative to the somewhat optimised atmospheric conditions. All experiments were conducted in a nitrogen atmosphere since it produced the best spectra.

5.5.1 ENERGY OPTIMISATION

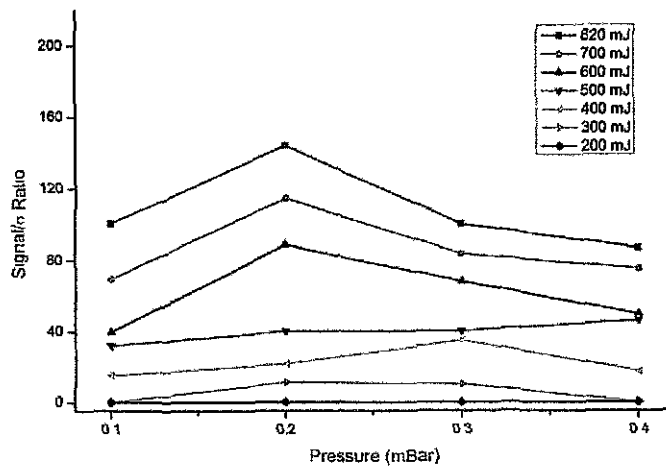
Spectra were taken from 4 to 5.5 mm from the target surface and in nitrogen pressures of 0.1 to 0.4 mBar, with the energy of the laser pulse being changed (via changing the voltage across the laser flashlamps) from 200 to 820 mJ. Spectra were averaged from 3 sets of 20 laser shots which were defocused by 3 mm into the target i.e. the focal point was 3 mm below the target surface. The target was cleaned with greatly defocused cleaning shots before spectra were recorded. The plots shown in Figure 14 represent the SSDR data taken at each spatial position.



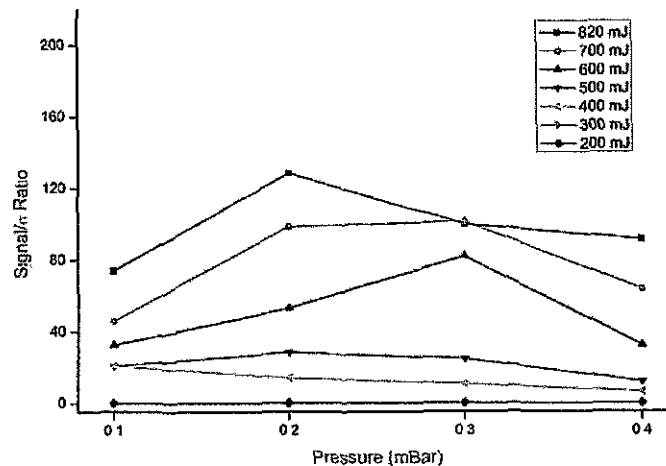
A) 4 mm



B) 4.5 mm



C) 5 mm



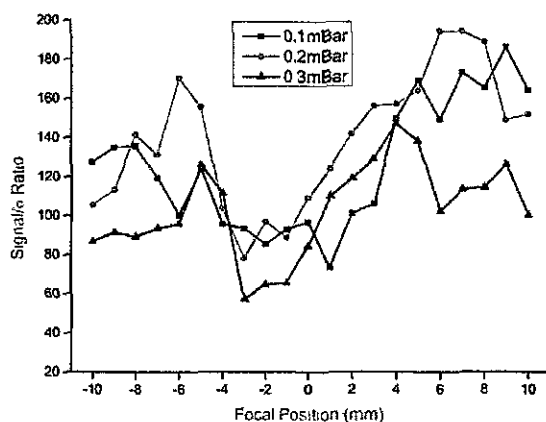
D) 5.5 mm

Figure 14: Signal/ σ with Varying Pulse Energy in Atmospherically Optimised Conditions (0.1 - 0.4 mBar) at A) 4 mm, B) 4.5 mm, C) 5 mm and D) 5.5 mm

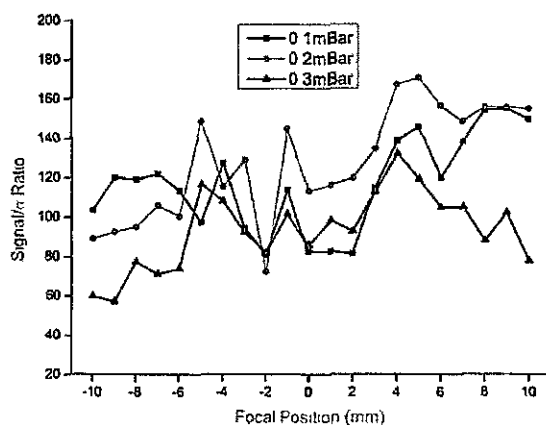
The spectra shown above are graphed using the same y axis (Signal/ σ Ratio) scale for easier comparison. The spectra show that the highest SDR figures are obtained using the most energetic pulses i.e. the maximum laser energy output, 820 mJ. The highest signal to standard deviation ratio was observed 4.5 mm from the target surface using an 820 mJ pulse in 0.2 mBar of nitrogen. This value was peaked far above the surrounding spatial distances, indicating that a "sweet spot" in terms of energy, distance and pressure had been found. With curves being reasonably flat up to 4.5 mm, the trend at and after this distance was similar but less pronounced than this optimum combination of parameters, eventually falling to quite uniform behaviour at 6 mm from the target surface.

5.5.2 LASER PULSE DEFOCUSING

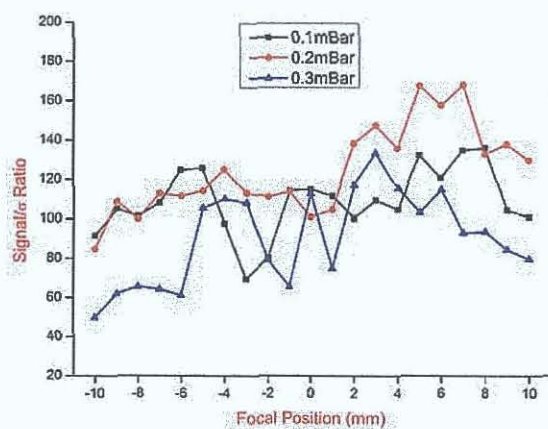
Defocusing effects were studied as a further step in the energy optimisation - again, the trade off between the target mass ablated by the laser pulse and the corresponding size of the plasma was a desirable variable to investigate. Initial spectra indicated that a very wide defocusing range was appropriate to find the best lens focus on target, as the degree to which line intensity and standard deviation values fluctuated were surprising, at least to the author - the defocusing range was surprisingly large. Spectra were therefore recorded in a range of nitrogen pressures from 0.1 to 0.3 mBar by accumulating 20 820 mJ laser pulses at distances between 4 and 5.5 mm from the target surface. The focal range of the 100 mm spherical lens was varied between -10 and +10 mm relative to the target i.e. 10 mm in front of and 10 mm behind the target surface. The results of this series of experiments can be seen in Figure 15 below.



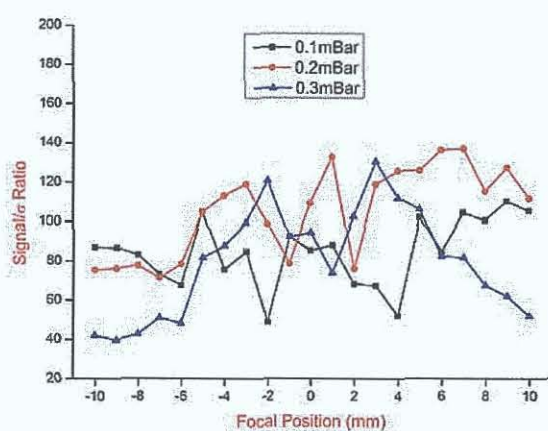
A) 4 mm



B) 4.5 mm



C) 5 mm



D) 5.5 mm

Figure 15: Signal/ σ with Varying Focus at Almost Optimised Distances - 820 mJ Pulse Energy, Nitrogen Atmosphere

Once again, the ratios calculated are the average values found from 3 separate spectra in each set of conditions. The effects of changing focus and concomitantly changing power density on the target surface are far greater than that seen in vacuum. Previously, the best results had been seen around 4.5 - 5 mm from the target surface but with the changes in power density this moves closer to the target surface, with a new maximum seen around 4 - 4.5 mm. Defocusing the spherical lens by +7 mm i.e. focusing the lens 7 mm below the target surface produces the best results yet when observed 4 mm from the surface in a 0.2 mBar nitrogen atmosphere. The maximum ratio seems to be consistent over all the axial distances with maxima seen at about +7 mm in 0.2 mBar of nitrogen.

There is a significant dip in the SDDR at small negative defocusing distances in the data shown close to the target surface. This is quite an interesting effect as since the atmosphere confines the plasma closer to the target surface than would normally happen in a freely expanding plasma created in vacuum, the laser pulse is focused into the hot, dense centre of the laser plasma as it expands. This appears to have a very negative effect on the signal to standard deviation ratio - the line intensity in these cases drop sharply as opposed to an increase in the standard deviation in the background

5.5.3 VARIATION IN THE NUMBER OF ACCUMULATED SHOTS

The last variable under consideration in this study was the number of shots accumulated in each spectrum. Up to this point, each spectrum has consisted of radiation accumulated from 20 laser produced plasmas on the target. As a final experimental variable, this was changed in order to observe both intensities from the S^{4+} line and the resulting changing signal to background ratio. The main concern with a large number of shots on target is the effect of plasma confinement in the cratered target (Zeng 2003, Yeates 2004). The resulting plasma expansion from the target surface can be affected due to modified electron densities and temperatures in the crater due to the effects of the target wall around the plasma as it is formed and starts to expand. It follows from these studies that a smaller number of shots would be preferable to avoid these effects but a larger number of shots could be desirable to increase accumulated line emission intensities from the laser plasma. These effects were considered with the knowledge that the main parameter would therefore be the variation in the background standard deviation and how it changed as the number of accumulated shots increased. Figure 16 below shows that (as may have been assumed before the experiment was conducted) the number of accumulated laser shots in the spectrum results in an increase in the raw line intensity. The data was again averaged from 3 spectra taken with the previously close-to-optimised parameters (820 mJ pulse, +7 mm focus, nitrogen atmosphere).

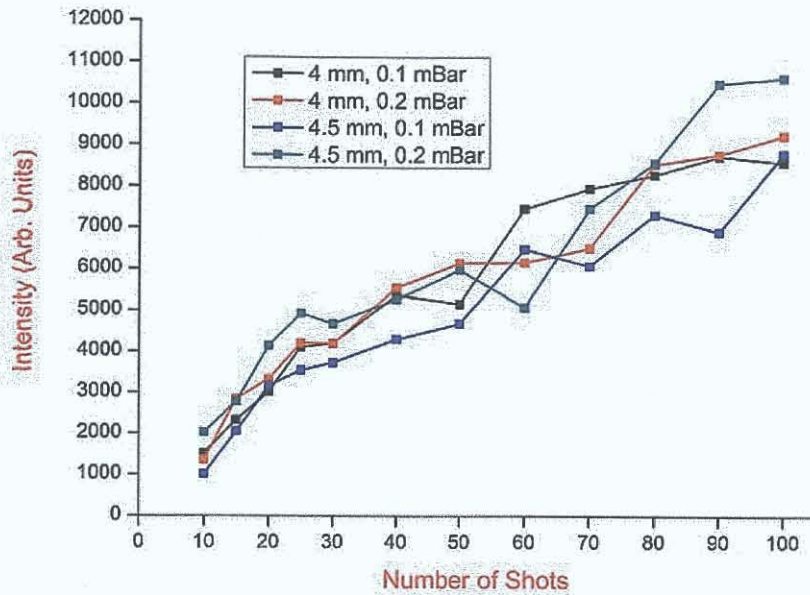


Figure 16: Intensity Increase with Varying Number of Laser Shots

The rate of increase in the intensity drops as the number of shots is increased. This increasing behaviour changes once the line intensity has been divided by the background intensity to produce the SDDR however. The next graph, Figure 17, shows how the nature of the data changed once more as the background standard deviation levels were considered.

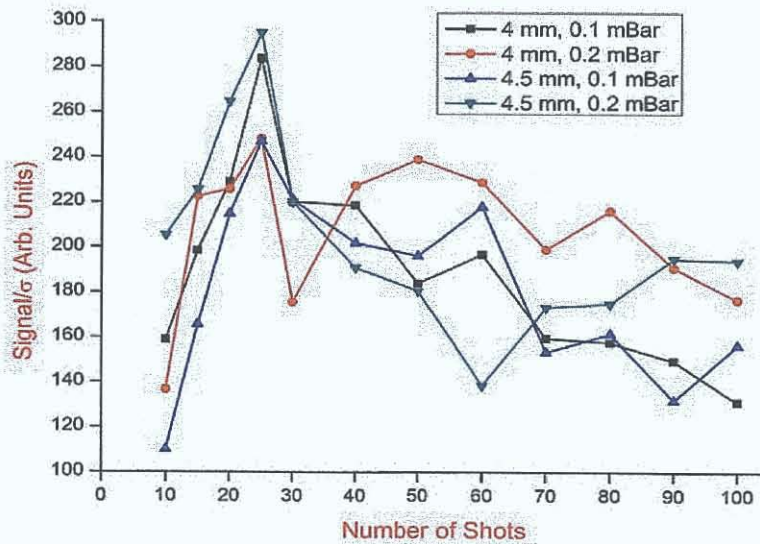


Figure 17: Variation in Signal to Standard Deviation Ratios with Increasing Numbers of Laser Shots

The data here is clearly peaked at 25 laser shots. The optimised conditions that this peak was seen in were 0.2 mBar of Nitrogen with spectra captured 4.5 mm from the target surface

5.6 CALIBRATION CURVES

The main goal of the preceding experiments was to find optimised conditions to perform a LIPS experiment for determining low levels of sulphur in iron/steel matrices. Spatial distance, energy and focal parameters were combined with gaseous atmospheres in order to see if a positive change in the emission intensity and signal to background ratio could be seen for the most suitable sulphur emission line. These conditions were seen to be optimised at the values shown in Table 2.

Table 2: Optimised Conditions for LIPS in Ambient Atmospheres

Parameter	Optimised Value
Line	S ⁴⁺ 78.65 nm
Gas	Nitrogen
Gas Pressure	0.2 mBar
Pulse Energy	820 mJ
Focus	+7 mm
Number of Shots	25
Axial Distance from the Surface	4.5 mm

The binary target on which the optimisation study was conducted was changed for a target carousel (see chapter 3) consisting of six calibrated steel standards containing very low concentrations of sulphur - a much lower range than the higher concentration targets used in the initial LIPS study in vacuum. The concentration range for this more sensitive study varied from 460 ppm down to the lowest available concentration, 27 ppm as opposed to the 0.38% - 0.0119% range used in the vacuum study. Each data point on each of the calibration curves is the result of 10 sets of 25 shots on target under optimised conditions, with each of the 10 sets of shots recorded from different areas on the target. Each target underwent the standard number of defocused cleaning shots prior to any spectra being recorded to

ensure that ejecta from previous shots on target would not interfere with the data being taken. Calibration curves were constructed using both the internally referenced scheme and sulphur intensities extracted directly from the target spectra.

5.6.1 INTERNALLY REFERENCED SULPHUR CALIBRATION

Since the sulphur line has such a high excitation energy, it was not possible to find a suitable iron line with a similar one in the spectral range observable by the camera. However, a line with a similar *relative* transition energy was found quite close - the Fe^{2+} line at 85.97 nm. This line has a lower energy level of 0 eV and an upper energy level of 14.42 eV, both relative to the ground state of Fe^{2+} . This is reasonably close to the upper energy of the S^{4+} line at 15.76 eV (relative to the S^{4+} ground state), making it a good candidate for referencing to the sulphur line. It was a feature of the spectra that a decrease in iron emission occurred both further out from the target surface and also with the addition of an ambient gas. This hampered the search for suitable iron lines to reference the sulphur line to.

The first calibration curve obtained from the six targets is found below in Figure 18, and is the calibration curve found using the internal referencing scheme where the intensity of a line under analysis is divided by an emission line of the main constituent of the sample - in this case, iron (see chapter 2, section 5)

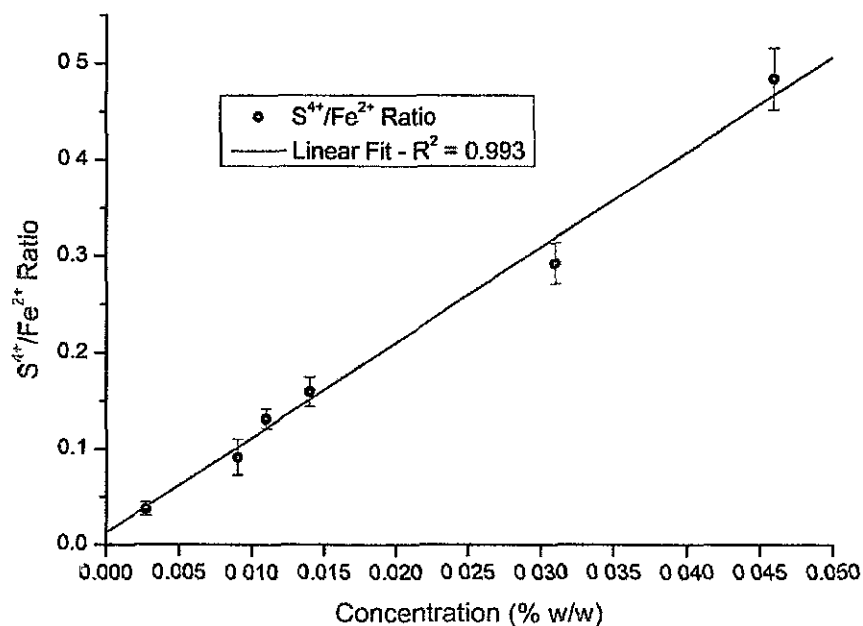


Figure 18 Internally Referenced Calibration Curve - Experimentally Optimised Conditions
(Nitrogen Atmosphere, 25 Shots, 820 mJ Pulse, +7 mm defocused)

The method by which a limit of detection is extracted from an internally-referenced calibration curve is quite similar to that of an unreferenced curve (St. Onge, 1997). Since the standard deviation in the background signal of the target with the lowest concentration of sulphur has been calculated at 9.8, this can be converted to the 3σ signal at which the detection limit is measured. Using the slope of the calibration curve, this value is then converted to the lowest detectable concentration, the detection limit. The usual formula (equation 5.1) is used to calculate the limit of detection

$$L.O.D. = \frac{3\sigma_B}{S} \quad [5.1]$$

where σ_B is the standard deviation in the background levels of the target with the lowest concentration of analyte and S is the slope of the calibration curve, as determined by the line fitting program. In the case of the referenced calibration curve, the limit of detection is 1.8 ± 0.2 ppm with the limit of quantification concomitantly 6 ± 0.5 ppm. These figures are quite accurate - the R^2 value of the linear fit (0.993) is also quite good, indicating a very linear plot

5.6.2 STANDARD CALIBRATION CURVE

Another calibration curve was constructed, this time using the raw sulphur line intensities from the spectra. Figure 19 on the next page shows the calibration curve produced by using the raw line intensities.

The calibration curve has quite a high slope for the concentrations involved and yet retains a high degree of accuracy, with an R^2 value of 0.994 indicating good linearity of the data. The slope of the line in the calibration curve is just above 170,000 as calculated by the line fit equation from the Origin© fitting software. The standard deviation in the background of the target with the lowest concentration of sulphur in it is about 9.8 - this is the standard deviation that must be used to calculate the Limit of Detection according to the IUPAC guide (IUPAC, 1978). These figures result in a limit of detection of 1.7 ± 0.1 ppm and a limit of quantification of 5.7 ± 0.3 ppm. These figures of merit are a little better than those found using the internal referencing curve, with the linear fit also a little more accurate - an R^2 value of 0.994 was calculated from the linear fit.

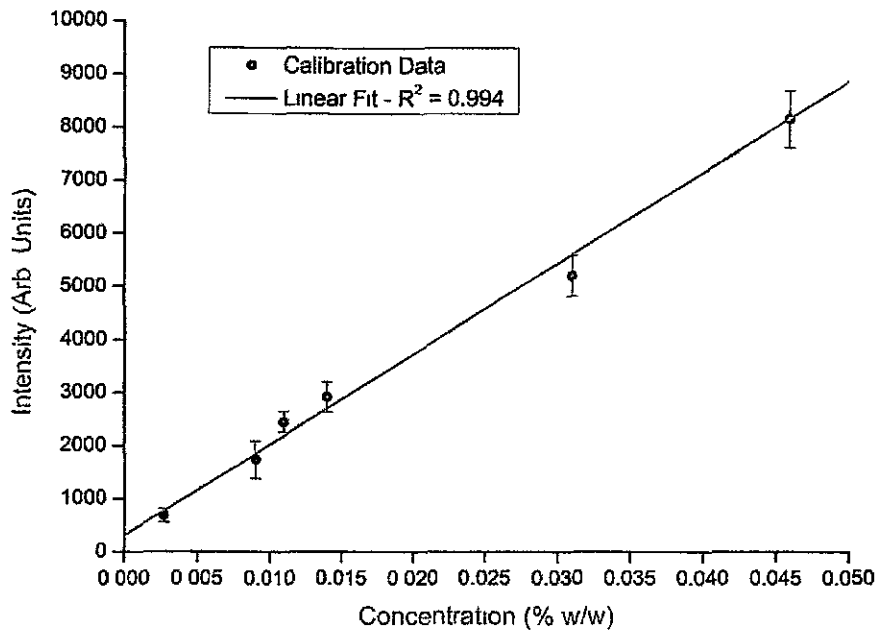


Figure 19: Calibration Curve - Experimentally Optimised Conditions
(Nitrogen Atmosphere, 25 Shots, 820 mJ Pulse, +7 mm defocused)

The lowest limit of detection published in the literature to date has been that published by Hemmerlin (2001) - 4.5 ppm using a neutral sulphur line in the near VUV at 180.73 nm. The same paper by Hemmerlin also states a limit of detection using spark optical emission spectroscopy of 3 ppm, which the current work also surpasses.

Using the standard calibration curve data, the accuracy of the elemental concentrations of the targets was compared to their pre-calibrated values quoted from the supplier. Table 3 on the following page shows how the data compared to them.

The concentrations gleaned from the calibration curve compare quite well to those quoted as the actual sulphur concentrations. There is an average 5% error in the calculated concentrations - this is calculated from the error in the slope of the line fit.

Table 3: Calculated vs. Actual Concentrations

Target	Actual Concentration (%)	Calculated Concentration (From Calibration Curve) (%)
361-XCCT	.011 ± .00023	.0115 ± .0008
361-XCCS	.014 ± .0003	.0149 ± .0007
CRMFE 1	.0027 ± .00006	.0026 ± .0001
361-54D	.046 ± .0012	.046 ± .001
351-215/3	.031 ± .0007	.03 ± .002
361-XAAS	.009 ± .0002	.0087 ± .0004

5.7 OBSERVATIONS & CONCLUSIONS

5.7.1 OBSERVATIONS

As has been stated in the theory section of this chapter, the reason that emission from laser plasmas created in ambient atmospheres seems to be more intense is that excitation of atomic species through collisional processes is more prevalent in some pressure regimes than others. It was seen that the emission from the S^{4+} ion reaches a maximum at 0.2 mBar - this is about the same pressure that both Harilal (2003) and Geohegan (1992) have stated that the laser plasma expansion changes from a freely-expanding vacuum model where particles from the plasma can easily penetrate the area into which they are expanding to a confined model where the plasma generates a barrier between the edge of the plume and the atmosphere in front of it. This behaviour was highlighted in another paper by Harilal (2002) in which he noted a peculiar plume splitting and sharpening phenomenon at 150 mTorr (2 mBar) - Figure 20 below is the image data from this paper.

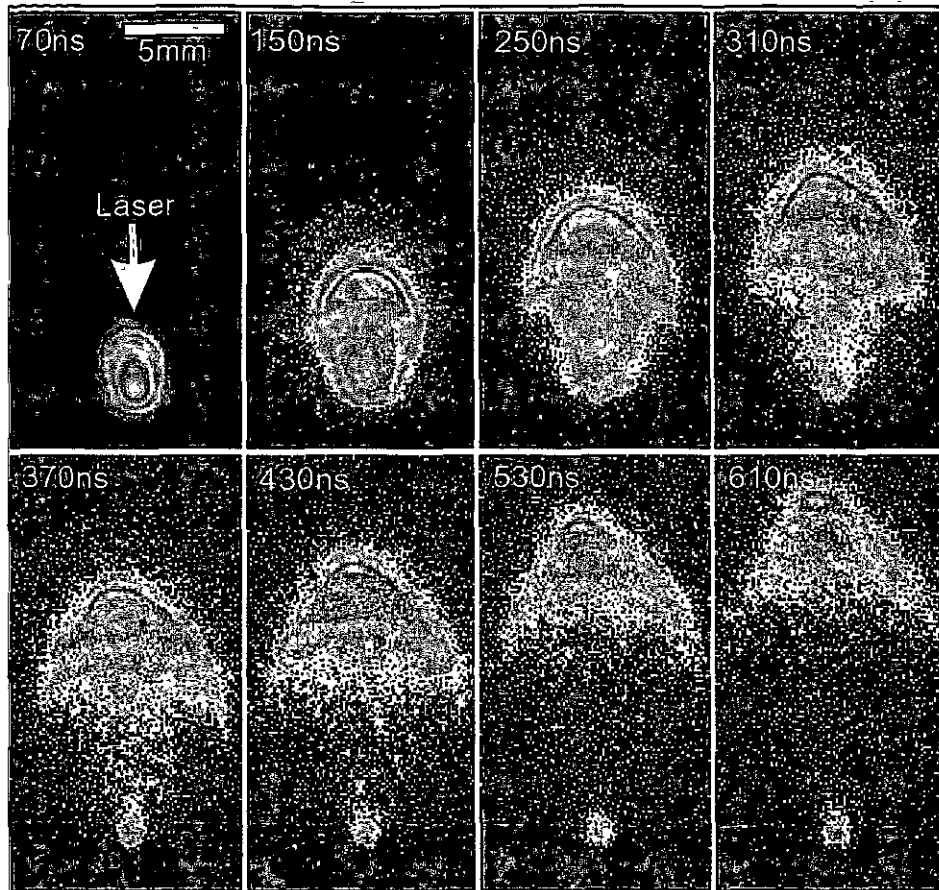


Figure 20: ICCD Photos of Visible Emission from Al Plasmas in 150 mTorr Air (Copyright AIP, Journal of Applied Physics 2003)

The collision strengths for several S^{4+} lines have been calculated theoretically by Hudson & Bell (2006). The particular transition responsible for the 78.65 nm line, the Mg-like $1s^2 2s^2 2p^6 3s^2 1S_0 - 1s^2 2s^2 2p^6 3s 3p^1 P_1^0$, has been shown both through experiment and calculation to have a relatively high effective collision strength (an order of magnitude or more) in comparison to the others for which the collision strength has been calculated. This goes some way to explaining how such a relatively highly ionised atomic species is capable of emitting at a higher level in a gaseous atmosphere where instinct might suggest that recombination would lead to low densities of this ion at distance from the target surface. It is notable from the data collected that this would also only hold for air and nitrogen - the peak emission in the argon atmosphere occurs at a pressure of about 7×10^{-2} mBar. In a previous paper from our laboratory, Khater et al (2002) showed that carbon detection limits were best optimised in an air atmosphere at about 0.2 mBar - again, the pressure at which the plume splitting and sharpening has been observed. This would seem to confirm again that the collisional excitation and recombination enhances the emission from

certain atomic species in the VUV as well as for the more commonly studied visible and UV transitions.

In the emission studies conducted to date, near-UV and visible emission lines have been used to monitor emission levels from the plasma. One paper by Naeem (2003) indicates that there is a difference in emission levels between different charge states of atomic species with regard to the atmospheric pressure of the gas they expand into, showing that higher charge states tend to emit more at lower pressures than the neutral species in the plasma. This fact would appear to hold true for VUV emission as well as visible and UV. This paper also suggests that the enhancement of some spectral lines of zinc is due to resonant charge transfer - this is a process where the transition energy of one level matches or nearly matches a sum of transition energies from another species. In the case of Naeem's paper, the energy difference between Ne and Ne^+ (21.56 eV) is very close to the sum of the excitation energies of $\text{Zn} + \text{Zn}^+$ (21.41 eV). When the ionisation energies of both sulphur and nitrogen were looked up (Chemical Rubber Company, 2006), it was seen that there was no correlation in the energies between any two or more atomic energy levels, as seen on the next page in Table 4.

However, the ionisation energy of the N_2 molecule is very close to the S^{4+} transition energy. Since N_2 is a covalently-bonded molecule, the ionisation energy can be expected to be larger than the nitrogen atom, since the bonding electrons are in a more stable energy state. The ionisation energy of molecular nitrogen is 15.58 eV, while the transition energy for the S^{4+} line at 78.65 nm is 15.76 eV. This may be a contributing factor to the increased emission in the laser plasma.

Another mechanism by which resonant ionisation of an electron occurs is radiative excitation. In order to achieve direct ionisation, a photon must be of or close to a transition energy of an absorbing atomic species. When the Kurucz database was searched, it was found that two singly ionised nitrogen emission lines at 48.58 nm (25.52 eV) and 48.74 nm (25.44 eV) have transition energies very close to the S^{3+} ionisation energy of 25.37 eV. It is quite possible that radiative ionisation of the S^{3+} species in the plasma plume is seeding the plasma with S^{4+} ions which then undergo collisional excitation and radiative de-excitation with the resultant emission of radiation at 78.65 nm. At the present time, a time-resolved diagnostic system does not exist in the laboratory in DCU, so this hypothesis unfortunately remains unverifiable.

Table 4: Ionisation Energies for Sulphur and Nitrogen Species

Species	Ionisation Energy ΔE (eV)
S	10.36001
S \rightarrow S ⁺	12.97787
S ⁺ \rightarrow S ²⁺	11.45212
S ²⁺ \rightarrow S ³⁺	12.432
S ³⁺ \rightarrow S ⁴⁺	25.3725
S ⁴⁺ \rightarrow S ⁵⁺	15.4585
N	14.5341
N \rightarrow N ⁺	15.0672
N ⁺ \rightarrow N ²⁺	17.84794
N ²⁺ \rightarrow N ³⁺	30.02426
N ³⁺ \rightarrow N ⁴⁺	20.4167

5.7.2 CONCLUSION

All of the detection limits listed have been obtained using lines in the near VUV at either 180.7 or 182 nm with the exception of the study by Radziemski which used a line at 545.4 nm. A recent paper by Asimellis (2006) a line in the near IR has been used for a qualitative study with a possible extension into a quantitative system but nothing further is available in the literature yet. All of the studied lines have also been from neutral species, which makes the deep VUV study conducted by this author a little more novel in its approach.

In terms of the detection limits for sulphur in steel, those seen in the present work are nearly three times better than those already quoted in the available literature, the previous most sensitive being that published by Hemmerlin (2001) where a LIPS scheme in the near VUV at about 180 nm was used to achieve a detection limit of 4.5 ppm. A comparison between this study and contemporary research into sulphur detection using LIPS is shown below in Table 5. The present study contains the lowest recorded limit of detection for sulphur to date.

Table 5: Sulphur Detection Limits

Author	Matrix	Detection Limit (ppm)
Gonzalez (1995)	Steel	70
Dudragne (1998)	Air	1500
Sturm (2000)	Steel	8
Noll (2001)	Steel	11
Hemmerlin (2001)	Steel	4.5
Sturm (2004)	Steel	7
Radivojevic (2004)	Steel	73
Radziemski (2005)	Soil	0.11%
<i>O'Leary (current)</i>	<i>Steel</i>	<i>1.7 ± 0.1</i>

REFERENCES

- Amoruso S et al.: "Characterisation of Laser-Ablation Plasmas", *Journal of Physics B: Atomic, Molecular and Optical Physics*, **32**, pp. R131 - R172 (1999).
- Asimellis G, Giannoudakos A and Kompitsas M: "New Near-Infrared LIBS Detection Technique for Sulfur", *Analytical and Bioanalytical Chemistry*, **385**, pp. 333 - 337 (2006)
- Corsi M et al.: "Temporal and Spatial Evolution of a Laser-Produced Plasma from a Steel Target", *Applied Spectroscopy*, **57**, pp. 715 - 721 (2003).
- Chemical Rubber Company *CRC Handbook of Chemistry and Physics 87th Edition*, CRC Press, 2006.
- CXRO Matter Interaction Calculator:
http://www-cxro.lbl.gov/optical_constants/gastrn2.html
- Dudragne L, Adam P and Amouroux J: "Time-Resolved Laser-Induced Breakdown Spectroscopy: Application for Qualitative and Quantitative Detection of Fluorine, Chlorine, Sulphur and Carbon in Air", *Applied Spectroscopy*, **10**, pp. 1321 - 1327 (1998).
- Geohegan DB: "Fast Intensified-CCD Photography of YBa₂Cu₃O_{7-x} Laser Ablation in Vacuum and Ambient Oxygen", *Applied Physics Letters*, **60**, pp. 2732 - 2734 (1992).
- Gonzalez A, Ortiz M and Campos J: "Determination of Sulphur Content in Steel by Laser-Produced Plasma Atomic Emission Spectroscopy", *Applied Spectroscopy*, **49**, pp. 1632 - 1635 (1995).
- Harilal SS et al.: "Influence of Ambient Gas on the Temperature and Density of Laser Produced Carbon Plasma", *Applied Physics Letters*, **72**, pp. 167 - 169 (1998).
- Harilal SS et al.: "Plume Splitting and Sharpening in a Laser-Produced Aluminium Plasma", *Journal of Physics D: Applied Physics*, **35**, pp. 2935 - 2938 (2002).
- Harilal SS et al.: "Internal Structure and Expansion Dynamics of Laser Ablation Plumes into Ambient Gases", *Journal of Applied Physics*, **93**, pp. 2380 - 2388 (2003).
- Herrmerlin M et al.: "Application of Vacuum Ultraviolet Laser-Induced Breakdown Spectrometry for Steel Analysis – Comparison with Spark-Optical Emission Spectrometry Figures of Merit", *Spectrochimica Acta Part B*, **56**, pp. 661 - 669 (2001)
- Hudson CE and Bell KL: "Fine Structure Effective Collision Strengths for the Electron Impact Excitation of S v", *Astronomy & Astrophysics*, **452**, pp. 1113 - 1120 (2006)
- IUPAC, Analytical Chemistry Division: "Nomenclature, Symbols, Units and their Usage in Spectrochemical Analysis - II Data Interpretation", *Spectrochimica Acta Part B*, **33**, pp. 241 - 245 (1978).

- Kagawa K et al. "XeCL Excimer Laser-Induced Shock Wave Plasma and its Application to Emission Spectrochemical Analysis", *Applied Spectroscopy*, **48**, pp. 198 - 205 (1994)
- Kelly, R. "Gas Dynamics of the Pulsed Emission of a Perfect Gas with Applications to Laser Sputtering and to Nozzle Expansion", *Physical Review A*, **46**, pp. 860 - 874 (1992).
- Kelly: Kelly Atomic Line Database, <http://cfa-www.harvard.edu/amdata/ampdata/kelly/kelly.html>.
- Khater MA, Costello JT and Kennedy ET: "Optimisation of the Emission Characteristics of Laser-Produced Steel Plasmas in the Vacuum Ultraviolet: Significant Improvements in Carbon Detection Limits", *Applied Spectroscopy*, **56**, pp. 970 - 983 (2002).
- Latkoczy C & Ghislain T: "Simultaneous LIBS and LA-ICP-MS Analysis of Industrial Samples", *Journal of Analytical Atomic Spectroscopy*, **21**, pp 1152 - 1160 (2006).
- Naeem TM, Matsuta H and Wagatsuma K. "Effect of Plasma Gas for Spectrometric Analysis of Tin and Zinc using Low-Pressure Laser-Induced Plasma", *Spectrochimica Acta Part B*, **58**, pp. 891 - 899 (2003).
- Noll R et al.: "Laser-Induced Breakdown Spectrometry - Applications for Production Control and Quality Assurance in the Steel Industry", *Spectrochimica Acta Part B*, **56**, pp 637 - 649 (2001)
- Park SM and Moon JY: "Laser Ablation of Graphite in an Oxygen Jet", *Journal of Chemical Physics*, **109**, pp. 8124 - 8129 (1998).
- Piepmieier EH & Osten DE. "Atmospheric Influences on Q-Switched Laser Sampling and Resulting Plumes", *Applied Spectroscopy*, **25**, pp 642 - 652 (1971).
- Radivojevic et al. "Microanalysis by Laser-Induced Plasma Spectroscopy in the Vacuum Ultraviolet", *Analytical Chemistry*, **76**, 1648 - 1658 (2004).
- Radziemski LJ et al. "Use of the Vacuum Ultraviolet Spectral Region for Laser-Induced Breakdown Spectroscopy-Based Martian Geology and Exploration", *Spectrochimica Acta Part B*, **60**, pp 237 - 248 (2005).
- Root RG: Chapter 2 - "Modelling of Post-Breakdown Phenomena", *Laser-Induced Plasmas and Applications*, Dekker, 1990.
- St. Onge L, Sabsabi M and Cielo P: "Quantitative Analysis of Additives in Solid Zinc Alloys by Laser-Induced Plasma Spectrometry", *Journal of Analytical Atomic Spectroscopy*, **12**, pp. 997 - 1004 (1997).
- Sturm V, Peter L and Noll R: "Steel Analysis with Laser-Induced Breakdown Spectrometry in the Vacuum Ultraviolet", *Applied Spectroscopy*, **54**, pp. 1275 - 1278 (2000).

- Wood RF et al: "Dynamics of Plume Propagation, Splitting and Nanoparticle Formation during Pulsed-Laser Ablation", *Applied Surface Science*, **129**, pp. 151 - 158 (1998).
- Yeates P: "A Spectroscopic and Diagnostic Study of Laser Plasma Generation and Evolution using Multi-Variable Target Conditioning", PhD thesis, Dublin City University, 2004
- Yinon J: *Modern Methods and Applications in Analysis of Explosives*, Wiley, 1993.
- Zeng X et al. "Plasma Diagnostics during Laser Ablation in a Cavity", *Spectrochimica Acta Part B*, **58**, pp 867 - 877 (2003).

CHAPTER VI: GENERAL CONCLUSIONS & FUTURE

WORK

The final chapter of this thesis is a general summary of the experiments performed and the conclusions which can be drawn from them. Some text is devoted at the end to possible *avenues of research in the future to further the goals of VUV LIPS development as both a fundamental study of laser-matter interaction and as an industrially important diagnostic assay tool.*

6.1 SUMMARY & CONCLUSIONS OF THE PRESENT WORK

6.1.1 SUMMARY

The goal of the present body of work has been the low-level quantitative determination of sulphur in steels. Sulphur has a large and mostly undesirable effect on the material characteristics of steel with most steelmaking processes designed to remove it completely from the end product. To this end, a number of optical emission spectroscopy (OES) experiments were carried out designed to optimise the emission from sulphur ions using the Laser-Induced Plasma Spectroscopy (LIPS) technique in particular. This technique involves the use of a high power laser to generate a typically hot, dense and short-lived plasma on the surface of solid targets. Radiation from the plasma is then used for both quantitative and qualitative evaluation of both major and minor elements in the material. To date, this technique has been almost exclusively used in the visible and UV regions of the electromagnetic spectrum owing to the ease of use of this region. This leaves a shortcoming when analysis of light elements is required as these elements' strongest emission lines lie in the vacuum ultraviolet (VUV). The most successful studies on light elements have used spectral lines in the near VUV at about 180 nm, with a notable exception being the analysis of carbon conducted by Khater et al. in 2002. That study proved the feasibility of deep VUV spectroscopy by attaining a limit of detection for carbon of 1.2 ppm, the lowest limit of detection yet achieved.

A variation on the most commonly used LIPS methodology is used for the current VUV studies. It involves the use of a time-integrated detection system instead of a time-resolved one to capture radiation emitted from the plasma. In a conventional LIPS system, light from the entire plasma plume is transported by optical components into a spectrometer where the specific wavelength range is selected and captured by a time-resolved detector. This allows the user to block out broadband "continuum" radiation from the early stages of the plasma by switching the camera on a sufficient time after the continuum-dominated stage has subsided and the emission is line-dominated. A novel and unconventional approach used in the current body of work uses the spatial characteristics of a laser plasma i.e. that the area closest to the target surface consists of continuum dominated emission and that areas further from the surface consist mainly of line-dominated emission.

In order to use the space-resolved LIPS technique, a modern, high-power Q-switched Nd:YAG laser system operating at the fundamental frequency of 1064 nm was used to generate laser plasmas in a custom-made vacuum chamber. The targets

were held in such a way that its position could be manipulated externally without the need to vent the chamber for each set of spatial parameters. The focusing lens for the laser system was also mounted on a rail so the focal characteristics could be changed according to the targets' position relative to the optical axis of the target chamber. Radiation from the plasma was spatially isolated by use of a pre-slit inside the target chamber. This radiation then entered a 1 metre VUV spectrometer equipped with a 1200 grooves/mm Al+MgF₂ diffraction grating which has a reciprocal linear dispersion of 0.83 nm/mm in the first order at its blazed wavelength of 80 nm. An Andor Technology back-illuminated VUV-sensitive CCD camera was used to capture the spectra produced. The camera was used in "full vertical binning" mode which means that photon counts in the vertical plane were summed. All equipment was kept at a constant pressure of 2×10^{-6} mBar due to the high absorption of VUV radiation by the atmosphere at atmospheric pressure. Later experiments using buffer gases used a glass capillary array (GCA) to isolate the target chamber from the spectrometer and CCD camera, with gases being pumped in at a controlled rate.

Optimisation studies were conducted using a binary target consisting of 0.68% sulphur, with the remainder iron. As the optimisation studies were concluded and the optimum plasma production conditions discovered, the binary target was switched for a target carousel consisting of six targets, each with a different concentration of sulphur in it. In the first set of optimisation experiment conducted in vacuum, a sulphur concentration of 0.119% - 0.38% was used to obtain data for a calibration curve. In the second set of experiments, a range of 27 ppm (parts per million) - 460 ppm was used.

6.1.2 CONCLUSIONS

The following conclusions may be drawn from the present body of work.

Vacuum Studies. An initial survey of the VUV spectrum from 40 - 140 nm was made in order to ascertain which sulphur emission lines were suitable for the present work. In this survey, four spectral lines at different stages of ionisation were observed to be free from spectral interference from underlying iron emission lines and to have a reasonable intensity. These lines were: S IV at 66.142 nm, S IV at 75.03 nm, S V at 78.65 nm and S VI at 93.3 nm. Of these, the S V line at 78.65 nm had the highest integrated emission intensity of the four, and was chosen as the main line with which to conduct the optimisation study. The first series of experiments involved the comparison between line and point plasmas using a cylindrical and a spherical lens. This showed that the drop off in intensity with increasing spatial distance was more

rapid using the cylindrical lens, but that the underlying continuum was more muted. As the laser pulse energy was varied, it was observed that the signal to standard deviation ratio using the spherical lens was far superior at an optimised energy of 600 mJ, while the cylindrical lens was optimised at 820 mJ - the maximum output energy the laser is capable of. Following the energy results, variation of the lens focal conditions were examined. This involved moving the lens into and out of focus on the target surface with the result that the power density on the surface changed. At the optimised energies, the cylindrical lens was seen to be optimised with the lens focus 1 mm below the target surface. The results from the spherical lens were more interesting however - a large dip in intensity was seen when the lens was focused 1 mm in front of the target with the best results clearly seen when the lens was focused 4 mm under the target surface.

With these parameters optimised for the calibration, experiments were performed on a selection of targets containing a wide range of pre-calibrated sulphur concentrations. These experiments resulted in calibration curves using both the cylindrical and spherical lenses. The calibration curve using the cylindrical lens resulted in an intercept on the y-axis of the graph that was quite high, indicating the possibility of a transition into a non-linear emission state with lower concentrations of sulphur. A limit of detection of 42 ppm was extracted from the calibration curve graph with a concomitant limit of quantification of 139 ppm. The spherical lens produced better results, although the y-intercept produced by the calibration curve remained high. A limit of detection of 28 ppm was obtained, with the concomitant limit of quantification of 94 ppm.

Studies in Gaseous Atmospheres. With the results from the previous study on targets in vacuum in mind, experiments using buffer gases were conducted using only spherical lenses. Preliminary observations indicated that the distance at which sulphur emission could be detected was double that of the vacuum studies. With such a large variation in spectra, another survey of suitable analytical lines was conducted. Despite the change in spectral emission, the resonant S^{4+} line at 78.65 nm remained the brightest line compared to 5 others in identical plasma ignition conditions.

The first parameter investigated in this series of experiments was the gas type and pressure. Argon, air and nitrogen were used as buffer gases with data taken in each of the gases at different pressures and distances. The large amount of data taken meant that the behaviour of the emission line in each gas at varying distances and pressures could be compared, with the best range of pressures and distances

chosen for further analysis. Spectra taken in each of the gases showed contrasts, with the result that the highest signal to standard deviation ratio was observed in plasmas created in a 0.3 mBar nitrogen atmosphere at distances of about 5 mm from the target surface.

This led to another series of experiments geared towards optimising the laser pulse energy in the nitrogen atmosphere. Peaks were seen in the data taken in a 0.2 mBar atmosphere, with the best data recorded at 4.5 mm from the target surface. The data was taken over a range of different pressures and distances to account for any localised fluctuations in the signal to standard deviation ratios. Defocusing of the lens accounted for the second part of the laser energy parameter, with trends seen to be best at the closer distances to the target surface i.e. 4 and 4.5 mm. The best results were seen with the lens defocused 7 mm under the surface of the target, a comparatively large distance compared to the vacuum study. The best data were again observed in 0.2 mBar of nitrogen.

Under these almost optimised conditions, some data was taken to compare the differences the number of accumulated spectra made. This was done as cratering of the target surface can have an effect on the shape of the emerging laser plasma owing to partial confinement effects. It was seen that, despite the steadily increasing emission from the laser plasma, the signal to standard deviation ratio was maximised at 25 laser shots.

With the basic analysis of optimum conditions now completed, calibration curves of the data were plotted using a set of targets with low concentrations of sulphur present in them. Two approaches to the calibration curves were used - the internally referenced method and the unreferenced method previously used in the vacuum studies. The internally referenced calibration curve resulted in a limit of detection of 1.8 ppm, while the unreferenced curve resulted in 1.7 ppm. Both of these limits are far better than those produced in vacuum and almost 3 times better than the best available LIPS limit of detection published in the literature to date.

6.2 FUTURE WORK

The VUV TISR-LIPS spectroscopic technique has been proved to work extremely well in this body of work and on previous occasions (Khater et al., 2000 & 2002). The challenges facing the development of the technique are now twofold - the continuing application to the detection of low levels of different elements & matrices and possible integration of the VUV technique into an industrial manufacturing line

6.2.1 AUTOMATION

In the author's opinion, the first task that should be completed for the furtherance of the VUV LIPS technique is the automation of the analysis process. In its current form, when spectra are recorded using the CCD camera software they must be reformatted, imported into the fitting programme and the desired line manually selected before a curve fit is applied to it. The process by which sections of the spectrum then have to be selected for the standard deviation to be calculated is equally long-winded, with the appropriate areas of the spectrum manually selected. Automation of the line fitting should be achievable using a computer programme such as Matlab © which has the most commonly used functions such as the Gaussian and Lorentzian profiles available as standard features, with the more complex profiles such as the Voigt profile readily accessible to the software with the assistance of the Matlab online community. Calculation of the background standard deviation has been commented on in the literature (Dawson, Snook & Price, 1993) with some novel solutions published (Schulze et al., 2006). With the automation of both of these tasks, spectra could be analysed quickly and efficiently with minimum time spent on the more tiresome aspects of the analysis process. This would enable more targets to be analysed quicker, with the result that more elements could be studied with more permutations in the type of spectrum taken and a possible industrial prototype developed.

6.2.2 DUAL PULSE TECHNIQUE

A great deal of research has been performed over the past number of years in the use of more than one laser pulse for generation of laser plasmas for the LIPS technique. There have been numerous reports of signal enhancement using multiple pulses in several configurations - a comprehensive review of these can be found in Babushok et al. (2006). Enhanced signals, a larger ablated target mass and longer-lived plasmas have been observed in the course of these studies using different beam geometries, different wavelengths, different laser pulse lengths and different inter-pulse delays. Some research has also been carried out on resonance-enhanced laser ablation, where the wavelength of one of the incident laser pulses matches that of an observed transition (i.e. the resonant laser pulse pumps the transition into its excited state). Resonant enhancement is an impractical goal for VUV LIPS because of the radiation wavelengths involved; however, the enhancement of signals due to increased mass ablation and also processes in the plasma plume (reheating) are quite feasible for further study. These enhancements have not been limited to UV and visible transitions in the plasma either - enhancements of VUV and soft x-ray

emission has also been observed using laser pulses incident on a "pre-plasma" generated by a primary laser pulse (Murphy et al., 2003)

The application to the existing system of a second laser would require the synchronisation of a second laser to the existing timing system in such a manner as to enable the inter-pulse delay to be modified easily and reliably. This could be done via the purchase of another delay generator relatively easily, providing there is availability of a second laser system. The picosecond laser system already in use in the laser plasma labs in DCU would be an excellent method of comparing the emission from both types of laser plasma - expansion dynamics of nanosecond and sub nanosecond plasmas tend to be dissimilar in nature and may have an effect on the type of emission observed from an experiment (See, for example Stavropoulos et al., 2004 and Barthélemy et al., 2005).

A second consideration is the method by which the second laser beam is introduced into the plasma. There are two configurations used in dual pulsing experiments - collinear and the orthogonal. The collinear configuration would be relatively straightforward to implement, however the orthogonal configuration may be a greater challenge as it would require modification of the existing chamber as there is only one free port into which laser pulses may enter. The collinear experiment would allow greater manipulation of the inter-pulse delay, but the orthogonal experiment has the advantage of shining the laser pulse onto a select area of the plasma parallel to the target surface. This would be particularly interesting given the spatially resolved nature of the current experiment.

6.2.3 PLASMA DIAGNOSTICS

Plasma diagnostics would be a good complement to the dual pulse technique as plots of electron densities and temperatures would give a greater insight into the mechanisms behind the enhanced emission observed in the VUV (Murphy et al., 2003). There has been a huge amount of research into plasma diagnostics over the years, with several commonly used techniques used for the determination of temperatures and pressures in the laser plasma (see for example Griem, 1964 and Lochte-Holtgreven, 1995). This has already been attempted by Khater (2002) with limited success due to the lack of availability of a VUV sensitive gated CCD camera. When an intensifier is used in conjunction with a CCD camera, it acts as a high-speed shutter by remaining open for times as low as a couple of nanoseconds. The problem with the fabrication of a VUV sensitive intensifier is that a suitable material has yet to be found out of which the intensifier can be fabricated.

In the course of this research, the author has attempted plasma diagnostics twice with limited success in one case and no success in another. In the first instance, a 0.5 m imaging spectrometer was used with a visible ICCD detector to try to study electron densities in the laser plasma. A huge number of iron lines were observed in the 300 - 700 nm range (the effective range of the spectrometer's diffraction grating) to such an extent that the resolution of the spectrometer was insufficient to fully distinguish individual iron or sulphur lines. The second attempt was made using an experimental camera provided by Andor Technology, supposedly sensitive in the VUV region. On use, it was found that the camera was not in fact sensitive to radiation dispersed by the VUV diffraction grating from 40 to 160 nm.

Plasma diagnostics using a VUV sensitive ICCD detector would represent a great addition to the current research. The earliest parts of the plasma's lifetime could be investigated also allowing for diagnostics on the higher ion stages to be performed with a modern, two dimensional detector. The differences between spatial and temporal resolution in the VUV LIPS experiment could also be compared directly.

6.2.4 INDUSTRIAL COLLABORATION

With the widespread use of LIPS as an industrial analysis technique, the logical step for the VUV LIPS system is integration into an industrial environment. There are a number of firms around the country involved in the manufacturing of steel products in which quality control plays an important part. The use of VUV LIPS in these plants would provide valuable data on industrially relevant steel samples to both the manufacturer for greater control of sulphur and carbon and to the experimentalist in order to gain a greater understanding of the manufacturing process in terms of elemental inclusions in the end product. The role played by LIPS in the LIBSGRAIN project (Bulajic et al., 2002) has led to greater development of the technique in general and has led to the improvement in quality of a manufactured product - both parties have benefited from the use of this analysis system. The specific details and requirements of a manufacturer are somewhat different to those of a laboratory and require modification of both equipment and its method of use; however the advantages in terms of the progress made on the technique development and the advantage to the wider industrial community make the challenges facing the VUV LIPS analytical technique well worthwhile.

REFERENCES

- Babushok VI et al.: "Double Pulse Laser Ablation and Plasma: Laser Induced Breakdown Spectroscopy Signal Enhancement", *Spectrochimica Acta Part B*, **61**, pp. 999 - 1014 (2006).
- Barthélemy O et al.: "Influence of the Laser Parameters on the Space and Time Characteristics of an Aluminium Laser-Induced Plasma", *Spectrochimica Acta Part B*, **60**, pp. 905 - 914 (2005).
- Bulajic D et al.: "Diagnostics of High-Temperature Steel Pipes in Industrial Environment by Laser-Induced Breakdown Spectroscopy Technique: the LIBSGRAIN Project", *Spectrochimica Acta Part B*, **57**, pp. 1181 - 1192 (2002).
- Dawson JB, Snook RD & Price WJ "Background and Background Correction in Analytical Atomic Spectroscopy - Part 1: Emission Spectroscopy, A Tutorial Review", *Journal of Analytical Atomic Spectrometry*, **8**, pp. 517 - 536 (1993)
- Griem, HR: *Plasma Spectroscopy*, McGraw-Hill, 1964.
- Khater M A et al.: "Time-Integrated Laser-Induced Plasma Spectroscopy in the Vacuum Ultraviolet for the Quantitative Elemental Characterization of Steel Alloys", *Journal of Physics D: Applied Physics*, **33**, pp. 2252 - 2262 (2000).
- Khater MA et al.: "Optimisation of the Emission Characteristics of Laser-Produced Steel Plasmas in the Vacuum Ultraviolet: Significant Improvements in Carbon Detection Limits", *Applied Spectroscopy*, **56**, pp. 970 - 983 (2002).
- Lochte-Holtgreven W: *Plasma Diagnostics*, AIP Press, 1995.
- Murphy A et al.: "VUV and Soft X-Ray Emission from Pre-Plasmas Irradiated with Picosecond and Femtosecond Pulses", *Proceedings of SPIE*, **4876**, pp. 1196 - 1203 (2003).
- Schulze HG et al.: "Automated Estimation of White Gaussian Noise Level in a Spectrum With or Without Spike Noise Using a Spectral Shifting Technique", *Applied Spectroscopy*, **60**, pp. 820 - 825 (2006)
- Stavropoulos P et al.: "Calibration Measurements in Laser-Induced Breakdown Spectroscopy Using Nanosecond and Picosecond Lasers", *Spectrochimica Acta Part B*, **59**, pp. 1885 - 1892 (2004)

APPENDIX A: EQUILIBRIUM IN PLASMAS

A laser produced plasma is considered to be in complete thermal equilibrium (CTE) if the following conditions are satisfied (Carroll & Kennedy, 1981):

- All neutral species, ions, electrons and particles can be described by the Maxwell velocity distribution
- The population distributions over the states of any atom or ion in the plasma are given by the Boltzmann distribution
- The number of ions in a charge state Z can be related to the number of ions in a charge state $Z-1$ using the Saha equation (see Chen, 1984 for example)
- The intensity distribution of the radiation in the plasma-occupied space can be calculated accurately using the Planck formula

A laser produced plasma in a steady state occurs when the rate of ionisation in the laser plasma is equal to the rate of recombination. The plasma temperature is also constant in the above state. The last criterion also implies that the laser plasma is optically thick at all frequencies in order for the Planck distribution to accurately model the radiation from the plasma. In most laser produced plasmas these four criteria are not approached and require the use of other methods to approximate the equilibrium state of a laser produced plasma. The three most commonly-used models used in laser plasma physics are *Local Thermal Equilibrium (LTE)*, *Coronal Equilibrium (CE)* and *Collisional Radiative Equilibrium (CRE)*. The main factor affecting the correct application of each of these models is the electron density in the laser plasma. Detailed descriptions of each of the following equilibrium states can be found in McWhirter (1965).

LOCAL THERMAL EQUILIBRIUM (LTE)

Local thermal equilibrium occurs in a laser produced plasma of sufficiently high electron density when collisional processes are more dominant in the plasma than radiative processes - Hughes (1975) states that the probability of collisional de-excitation must exceed that of radiative de-excitation by a factor of 10 for LTE to apply. The collisional excitation processes are also in balance with the collisional de-excitation processes. Plasmas in LTE can be described at discrete local points by all the criteria for a plasma in CTE with the exception of the Planck formula - radiative effects are assumed to play a negligible role in the equilibrium state of the plasma in this model. The temperature T_i which describes the velocity distribution of the ions

and neutrals and the electron temperature T_e are not assumed to be the same in this model. This is based on the fact that electron-atom and electron-ion interactions are of far greater significance than atom-ion interactions, which do not greatly affect the equilibrium condition.

The lower electron density boundary below which the laser plasma cannot be described as being in LTE has been derived by McWhirter (1965) and is given by:

$$n_e \geq 1.6 \times 10^{12} T_e^{1/2} \chi^3 \text{ cm}^{-3} \quad [\text{A.1}]$$

In equation [A.1], T_e is the electron temperature in Kelvin and χ is the excitation potential in eV of the atomic/ionic transition under consideration.

CORONAL EQUILIBRIUM

As the electron density of the plasma decreases over time to the point where it is comparable to the Sun's corona ($n_e \approx 10^8 \text{ cm}^{-3}$) the probability of radiative de-excitation becomes comparable to de-excitation by collisional processes, even exceeding it at low densities. In this model, the main excitation process is due to electron impact ionisation due the optically thin nature of the bulk plasma. The main de-excitation processes are also radiative - in these low density plasmas the low collision frequency means that radiative de-excitation is the dominant process type and is primarily achieved through spontaneous radiative decay and radiative recombination. The fact that the atomic processes have varying degrees of importance and that each of these processes are not directly in balance with its inverse results in the establishment of a different type of equilibrium, as outlined by Colombant & Tonon (1973).

COLLISIONAL RADIATIVE EQUILIBRIUM

The development of the CRE model of equilibrium in laser plasmas was to compensate for the intermediate electron density ranges i.e from about $n_e = 10^{19} - 10^{21} \text{ cm}^{-3}$ where neither the LTE nor CE models can be effectively applied. These electron densities correspond to the critical densities of plasmas created with CO₂ and Nd:YAG lasers respectively. The model itself is based on the CE model, with modifications made in order to include collisional de-excitation and three body recombination processes in the upper energy levels of transitions occurring in this density range, as in the LTE model. Radiative recombination and spontaneous radiative decay remain an important inclusion for the lower energy levels, as in the

coronal model. The two primary criteria for the valid application of the CRE model have been stated by Colombant & Tonon (1973) and are:

1. The velocity distribution of the electrons in the laser plasma must be Maxwellian. This occurs when the electron-electron relaxation time is smaller than the heating time, a common feature of laser produced plasmas.
2. The population density of species in the charge state $Z + 1$ must not change to any significant degree when the steady-state population distribution is being established amongst the species in the plasma of charge Z .

The steady-state ion distribution has been defined for the CRE model by Colombant & Tonon (1973) as:

$$\frac{n_{Z+1}}{n_Z} = \frac{S(Z, T_e)}{[\alpha_r(Z+1, T_e) + n_e \alpha_{3b}(Z+1, T_e)]} \quad [\text{A.2}]$$

In [A.2], the terms apply as follows:

- $S(Z, T_e)$ is the collisional ionisation coefficient
- $\alpha_r(Z+1, T_e)$ is the radiative recombination coefficient
- $\alpha_{3b}(Z+1, T_e)$ is the three body recombination coefficient

Equation [A.2] has been derived with the assumption that in plasmas with an electron temperature of greater than 30 eV, the three body radiative recombination term $n_e \alpha_{3b}$ is far lower than that of the radiative recombination term α_r . As such, the ion distribution equation [A.2] can be approximated to be density-independent, with the following relationship holding:

$$Z \approx \frac{2}{3} [AT_e]^{1/3} \quad [\text{A.3}]$$

where A is the atomic number of the relevant element. This relation is applied more successfully to elements with high atomic number rather than the lighter elements.

REFERENCES

- Carroll PK & Kennedy ET: "Laser-Produced Plasmas", *Contemporary Physics*, **22**, pp. 61 - 96 (1981)
- Chen FF: *Plasma Physics and Controlled Fusion Volume 1: Plasma Physics*, Plenum Press, 1984
- Colombant D & Tonon GF: "X-Ray Emission in Laser-Produced Plasmas", *Journal of Applied Physics*, **44**, pp 3524 - 3537 (1973)
- McWhirter RWP: *Plasma Diagnostics*, Academic Press, New York, 1965
- Hughes TP. *Plasmas and Laser Light*, Hilger, 1975.

APPENDIX B: TARGETS

All target materials in this appendix can be found in the Glen Spectra Reference Materials catalogue, the company from which they were purchased.

The table is split into three main sections. The first is the binary target used for the optimisation studies, the second is the set of targets used for the calibration in chapter 4 and the third is the set of targets used in the calibration found in chapter 5.

Target Set	Sample	Concentration (%)	
		Sulphur	Iron
Binary	341-14920	0.68	99.62
Chapter 4 Target Set	361-65C	0.115	97.89
	361- 50E	0.0119	99.83
	182-206A	0.26	98.45
	361-54D	0.046	97.27
	201-123	0.38	97.08
	361-52D	0.088	97.75
Chapter 5 Target Set	361-XCCT	0.011	96.99
	361-XCCS	0.014	99.46
	081-CRMFE1	0.0027	99.88
	361-54D	0.046	97.27
	351-215/3	0.031	98
	361-XAAS	0.009	99.78

APPENDIX C: SPECTRAL LINE PROFILES

The majority of this appendix can be found in Lochte-Holtgreven (1995).

Spectral lines emitted from laser produced plasmas are, in general, observed to have a finite range directly proportional to the width of the entrance slit of the spectrometer. The intensity profile is centred on a frequency ν_0 and can be represented by the equation:

$$I = \int_{\nu_0 - \infty}^{\nu_0 + \infty} I(\nu) d\nu \quad [\text{C.1}]$$

Spectral line profiles are characteristic of conditions prevailing in the plasma and also the influence the dispersion instrumentation has. The types of line profile they result in are Gaussian and Lorentzian, with a convolution of the two resulting in the Voigt profile. The convoluted Voigt is the most common type of line profile due to several broadening mechanisms present in a typical experiment.

Doppler broadening is where thermal motion of an emitting species in a laser produced plasma shifts the central frequency of the spectral line so that the resulting profile is broadened. Doppler broadening results in a line profile of the Gaussian type which is of the form:

$$f(x) = C \exp\left(-\frac{x^2}{B_1^2}\right) \quad [\text{C.2}]$$

in which case B_1 and C are constants.

Stark or collisional broadening in a laser produced plasma occurs when the energy level structure of an atomic species is perturbed when it collides with charged particles in the plasma. The line profile most commonly associated with Stark broadening is the Lorentzian profile, of the form:

$$f(x) = \frac{C}{1 + \frac{x^2}{B_2^2}} \quad [\text{C.1}]$$

Again, B_2 and C are constants. Natural broadening is another type of broadening with a Lorentzian profile. It is caused by the fact that exact determination of the energy state of an electron is impossible due to the Heisenberg uncertainty principle. Natural broadening accounts for the minimum possible line width (the full width at half-maximum, FWHM, of the spectral line) observable from an emission source.

Consider a spectral line with two components where the first component of the line can be represented by the function $I(x) = f(x)$ and the second component

can be represented by the function $I(x) = \phi(x)$ where x is relative to the central wavelength of the spectral line (λ_0) i.e. $\lambda_0 - \lambda = x$. When both functions act on a point on the profile $x = \lambda'$, the corresponding intensity at this point is given by the equation:

$$I(\lambda') = \int_{-\infty}^{\infty} f(x)\phi(\lambda' - x)dx = F(\lambda') \quad [\text{C.4}]$$

If both components of the line profile are Gaussian, the total line profile can be considered as a Gaussian with the constant B_1 calculated to be $B_1^1 = B_1'^2 + B_1''^2$. If both components are Lorentzian, then the total line profile can also be considered to be Lorentzian with the appropriate constant B_2 calculated by $B_2 = B_2' + B_2''$. If both types of components are acting on the line intensity simultaneously, then the resulting profile is known as a Voigt profile - a convolution of both types of line profile. The Voigt profile takes the generalised form:

$$F(x) = \frac{\left[C \exp\left(-\frac{x^2}{B_1^2}\right) \right]}{\left[1 + \left(\frac{x^2}{B_2^2}\right) \right]} \quad [\text{C.5}]$$

Voigt profiles appear generally Gaussian near the centre and Lorentzian near the wings of the line. A comparison between the three types of line profile can be seen in Figure 1 below.

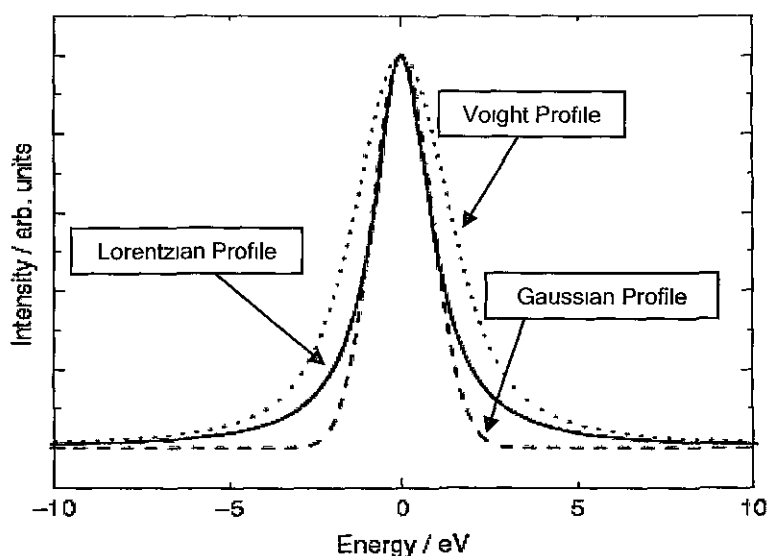


Figure 1: Comparison of Gaussian, Lorentzian and Voigt Line Profiles (Taken from Hesse, Streubel & Szargan, 2007)

As seen in Figure 1 on the previous page, the three types of line profile have been fitted to an imaginary spectral line with a set peak value i.e. the intensity at the central frequency of the line, ν_0 , is the same for all three profiles. The shape of the line profiles after this is different - if each of the profiles shown above were integrated, each would result in a different area under the curve. It is therefore vital that the proper line profile is used in the analysis of spectral lines, as this can affect the results of line integrations to a large degree.

REFERENCES

- Hesse R, Streubel P & Szargan R: "Product or Sum. Comparative Tests of Voigt, and Product or Sum of Gaussian and Lorentzian Functions in the Fitting of Synthetic Voigt-Based X-Ray Photoelectron Spectra", *Surface and Interface Analysis*, **39**, pp 381 - 391 (2007)
- Lochte-Holtgreven W *Plasma Diagnostics*, AIP Press, 1995

LIST OF FIGURES

Chapter 2

Figure 1:	Laser Plasma Formation (After Eliezer, 2002)	19
Figure 2:	Free-Free Radiative Processes	22
Figure 3:	Free-Bound Processes	24
Figure 4:	Bound-Bound Processes	25
Figure 5:	Transition Constants	28
Figure 6:	Gaussian Distribution	30

Chapter 3

Figure 1:	Experimental System Overview	36
Figure 2	Surelite III-10 Laser and Pulse Temporal Profile	37
Figure 3	Laser Pulse Energy Variation	38
Figure 4:	Laser Operation - Pockels Cell "Off"	39
Figure 5:	Laser Operation - Pockels Cell "On"	40
Figure 6	Target Chamber	42
Figure 7	Target Manipulator	43
Figure 8	Target Carousel	44
Figure 9:	Microscope Image of a Typical GCA, © Burle Industries Inc.	45
Figure 10	ARC VM-521 Spectrometer	46
Figure 11	Rowland Circle	47
Figure 12:	ARC VM-521 VUV Spectrometer Schematic	48
Figure 13:	Image Formation Schematic (After Samson)	49
Figure 14:	Spectrometer in Normal Incidence and Near Normal Incidence Configurations	52
Figure 15:	P-Type Silicon MOS Gate (After Holst, 1996)	56
Figure 16:	Unbinned CCD Camera Image	57
Figure 17	Full Frame CCD Chip	58
Figure 18:	Experimental Timing Scheme	61

Chapter 4

Figure 1:	Calculated Gas Transmission Curves for VUV Radiation at Different Pressures (1 m path length)	65
Figure 2:	Typical Laser Produced Plasma (After Eliezer, 2002)	67
Figure 3:	Intensity Variation with Spatial Distance - 100 mm Spherical Lens	68

Figure 4:	VUV Emission Survey A) 40 - 60 nm, B) 60 - 80 nm, C) 80 - 100 nm, D) 100 - 120 nm, E) 120 - 140 nm	72
Figure 5:	A) S IV - 66.142 nm; B) S IV - 75.03 nm, C) S V - 78.65 nm; D) S VI - 93.3 nm	73
Figure 6:	Grotrian Diagram of Relevant Transitions	74
Figure 7:	Calculated Power Densities with Varying Focus for Spherical and Cylindrical Lenses	76
Figure 8	Columbant & Tonon Model Electron Temperatures - Cylindrical and Spherical Lenses	77
Figure 9:	Spatial Spectral Variation using a Cylindrical Lens	78
Figure 10:	Energy Variation Effect at 1.5 mm - 100 mm Spherical Lens	80
Figure 11:	Signal to Standard Deviation Ratios for Varying Pulse Energies at 1, 1.5 and 2 mm - 100 mm Spherical Lens	80
Figure 12:	Energy Variation Effect at 1.5 mm - 150 mm Cylindrical Lens	81
Figure 13:	Signal to Standard Deviation Ratios for Varying Pulse Energies at 1, 1.5 and 2 mm - 150 mm Cylindrical Lens	82
Figure 14:	Positive (left) and Negative (right) Defocusing Schemes	83
Figure 15:	Signal to Background Ratios Under Varying Focal Conditions at 1, 1.5 and 2 mm - 150 mm Cylindrical Lens	84
Figure 16:	Signal to Background Ratios Under Varying Focal Conditions at 1, 1.5 and 2 mm - 100 mm Spherical Lens	85
Figure 17	Calibration Curve - Cylindrical Lens (820 mJ, 1 mm from the Target Surface, 1 mm Defocused)	87
Figure 18:	Calibration Curve - Spherical Lens (600 mJ, 1.5 mm from the Target Surface, 4 mm Defocused)	89
Chapter 5		
Figure 1:	Plasma Expansion Into an Ambient Gas	95
Figure 2	Figure 2: Qualitative Comparison of 1-D Laser Absorption Waves - A) LSC Wave, B) LSR Wave, C) LSD Wave (After Root 1989)	98
Figure 3:	Experimental Configuration	100
Figure 4	Laser Plasma Expansion into A) Vacuum and B) Low Pressure Nitrogen	101
Figure 5.	Test Spectra at A) 2 mm and B) 5 mm	102
Figure 6:	Varying S ⁴⁺ Intensity at A) 2 mm and B) 5 mm	103
Figure 7:	Gas Transmission Curves at 78.65 nm for Argon (red),	

	Air (green) and Nitrogen (blue) - 12 cm Path Length	105
Figure 8:	Argon Spectra - 4.5 mm from Target Surface, 20 x 820 mJ Laser Pulses Defocused 3 mm into the Target	106
Figure 9:	Air Spectra - 4.5 mm from the Target Surface, 20 x 820 mJ Laser Pulses Defocused 3 mm into the Target	107
Figure 10:	Nitrogen Spectra - 4.5 mm from Target Surface, 20 x 820 mJ Laser Pulses Defocused 3 mm into the Target	108
Figure 11:	A) Raw Line Intensities and B) Signal/ σ Ratios for S V (78.65 nm) in Varying Argon Pressures and at Varying Target Distances	109
Figure 12:	A) Raw Line Intensities and B) Signal/ σ Ratios for S V (78.65 nm) in Varying Air Pressures and at Varying Target Distances	111
Figure 13:	A) Raw Line Intensities and B) Signal/ σ Ratios for S V (78.65 nm) in Varying Nitrogen Pressures and Varying Target Distances	112
Figure 14:	Signal/ σ with Varying Pulse Energy in Atmospherically Optimised Conditions (0.1 - 0.4 mBar) at A) 4 mm, B) 4.5 mm, C) 5 mm and D) 5.5 mm	115
Figure 15:	Signal/ σ with Varying Focus at Almost Optimised Distances - 820 mJ Pulse Energy, Nitrogen Atmosphere	117
Figure 16:	Intensity Increase with Varying Number of Laser Shots	119
Figure 17:	Variation in Signal to Standard Deviation Ratios with Increasing Numbers of Laser Shots	119
Figure 18:	Internally Referenced Calibration Curve - Experimentally Optimised Conditions (Nitrogen Atmosphere, 25 Shots, 820 mJ Pulse, +7 mm defocused)	121
Figure 19:	Calibration Curve - Experimentally Optimised Conditions (Nitrogen Atmosphere, 25 Shots, 820 mJ Pulse, +7 mm defocused)	123
Figure 20:	Figure 20: ICCD Photos of Visible Emission from Al Plasmas in 150 mTorr Air (Copyright AIP, Journal of Applied Physics 2003)	125